UNIVERSITÀ DI PARMA

UNIVERSITÀ DEGLI STUDI DI PARMA

DOTTORATO DI RICERCA IN

"INGEGNERIA INDUSTRIALE"

CICLO XXXI

Al-Si-Mg Alloys produced by Casting and Selective Laser Melting (SLM): The Influence of Microstructure on Mechanical and Fracture Behaviour

Cordinatore:

Chiar.mo Prof. Gianni Royer Carfagni

Tutore:

Chiar.ma Prof.ssa Emanuela Cerri

Dottoranda:

Maria Teresa Di Giovanni

Anni 2015/2018

“Source your sense of self

from your integrity

in every

interaction.”

Chani Nicholas

Preface

This doctoral thesis is the result of three years of study full-time, including courses and research at the University of Parma, Italy, from November 2015 to November 2018. Most of the experimental work has been carried out at the Department of Engineering and Architecture (DIA) in Parma. The first part of the experimental work was conducted at the Norwegian University of Science and Technology in close cooperation with the Solidification/Casting Group during my stay in Trondheim from April to July 2016. The second part of the experiments was conducted at the Laboratory of Fracture Mechanics, Department of Metallurgical and Materials Engineering, COPPE/Federal University of Rio de Janeiro, during my stay in Rio de Janeiro from October 2017 to April 2018.

Professor Emanuela Cerri at the Department of Engineering and Architecture (DIA) was the main supervisor. Professor Marisa Di Sabatino Lundeberg hosted my stay at the Norwegian University of Science and Technology. Professor Enrique Mariano Castrodeza hosted my stay at the Federal University of Rio de Janeiro.

Doctoral scholarship was partially founded by the "Fondazione Cariparma".

Aim of the present PhD work was, from one side, the study of the influence of element additions and/or heat treatment optimization on the mechanical response of Al-Si-Mg aluminum cast alloy; from the other side the fatigue crack growth behavior of AlSi10Mg alloy produced by SLM additive manufacturing technology. The research was subdivided into separate projects and led to five articles, which represent the main part of this doctoral thesis. The manuscripts are:

1. M.T. Di Giovanni, E. Cerri, M. Merlin, D. Casari, G.L. Garagnani, L. Arnberg., "The Influence of Ni and V Trace Elements on High-Temperature Tensile Properties and Aging of A356 Aluminum Foundry Alloy''. *Metallurgical and Materials Transactions A*, vol. 47(5), pp. 2049-2057, 2016.

2. M.T. Di Giovanni, E. Cerri, T. Saito, S. Akhtar, P. Åsholt, Y. Li, M. Di Sabatino. "How Slight Solidification Rate Variations within Cast Plate Affect Mechanical Response: A Study on As-Cast A356 Alloy with Cu Additions". *Advances in Materials Science and Engineering*, vol. 2018(3), pp. 1-11, 2018.

3. M.T. Di Giovanni, E. A. Mørtsell, T. Saito, S. Akhtar, M. Di Sabatino, Y.Li, E. Cerri. "Influence of Cu addition on the heat treatment response of A356 foundry alloy", **submitted** to *Material Science and Engineering A.*

4. M.T. Di Giovanni, J. T.O. de Menezes, E. Cerri, E. M. Castrodeza. "Influence of microstructure and porosity on the fracture toughness of Al-Si-Mg alloy", **submitted** to *Journal of Material Research and Technology*.

5. M.T. Di Giovanni, J. T.O. de Menezes, G. Bolelli, E. Cerri, E. M. Castrodeza. "Fatigue crack growth behavior of a selective laser melted AlSi10Mg", **submitted** to *Engineering Fracture Mechanics*.

The list below reports publications concerning research paper and side activities in the framework of light alloys. These papers were written during the three years' period but are not included in this thesis.

- M.T. Di Giovanni, E. Ghio, T. Rimoldi, E. Cerri. "Stability of intermetallic phase particles in Al-Si-Mg foundry alloy: the role of Cu additions", **submitted** to *Transactions of Nonferrous Metals Society of China.*

- L. Lattanzi, M. T. Di Giovanni, M. Giovagnoli et. al. "Room Temperature Mechanical Properties of A356 Alloy with Ni Additions from 0.5 Wt to 2 Wt %". *Metals*, vol. 8(4), pp. 224-239, 2018.

- E. Cerri, D. Knez, T. Rimoldi, M. T. Di Giovanni. "Microstructure evolution and mechanical properties of hot deformed Mg9Al1Zn samples containing a friction stir processed zone". *Journal of Magnesium and Alloys*, vol. 5, pp. 388-403, 2017.

- M.T. Di Giovanni, E. Cerri, T. Saito, S. Akhtar, P. Åsholt, Y. Li, M. Di Sabatino. "Effect of copper additions and heat treatment optimization of Al-7% Si Aluminum Alloy", *La Metallurgia Italiana*, vol. 11, pp. 43-47, 2016.

- M.T. Di Giovanni, E. Cerri, M. Merlin, D.Casari, G.L.Garagnani. "Correlation between Aging Effects and High Temperature Mechanical Properties of the Unmodified A356 Foundry Aluminium Alloy". *Materials Science Forum*, vol.879, pp. 424-429, 2016.

- E.Cerri, M.T. Di Giovanni, T.Rimoldi, L.Cristofolini. "Fracture Surface Characterisation of Friction Stir Processed Magnesium Alloy after Mechanical Tests". *Materials Science Forum,* vol. 879, pp. 301-306, 2016.

- D. Casari, F. Poli, M.T. Di Giovanni M. Di Sabatino."Effect of Ni additions on A356 alloy's microstructure and high-temperature mechanical properties''. *La Metallurgia Italiana*, vol. 6, pp.37-40, 2016.

- E. Cerri, M. T. Di Giovanni. "Mechanical properties of a Friction stir processed Hpdc magnesium alloy'. *HTDC – Conference proceedings AIM*, 21-24 Jun 2016.

- M. T. Di Giovanni, E. Cerri "Copper Influence on aging behaviour of a commercial A356 foundry alloy. A study towards elongation.". *ISBN 978-88-98237-21-0*, pp. 41-44, 2016.

- M. T. Di Giovanni, E. Cerri "Influence of Nickel and Vanadium Impurities on High Temperature Tensile Properties of A356 Aluminium Foundry Alloy". ISBN 978-88-98237-17-3, pp. 106-110, 2015.

Acknowledgements

I would like to thank: Daniel Pennac, Mazzy Star, Stefano Benni, The Strokes, Andrea Pazienza, Radio Deejay, Chapelier Fou, Nobraino Rob Brezny, Zero Calcalare, Sibilla Aleramo, Cristicchi, Caparezza, Valentina D'Urbano, Marco Polo (Netflix), The Smiths, Chico Buarque, Igor Sibaldi, Le luci della centrale Elettrica, Lauryn Hill, Dott. Mozzi, Pino Daniele, Lonely Planet, Dante Alighieri, Banksy, Lou X, Internazionale (magazine), Mima, Marielle Franco, Dario Brunori, Lucio Battisti, Rousseau, Dalla, Gabriel Garcìa Màrquez, Lou Reed, Wes Anderson, The National, Cirque de Soleil, Truman Capote, The Cure, Shy (Braking Italy), Paolo Virzì, Nicolò Fabi, and many others whose arts, genius and ideas alleviated the path over the last three years.

I owe my deepest gratitude to Prof. Arnberg for believing in me and encouraging me to undertake this challenging experience.

I am grateful to my tutor Prof. Cerri for given me all the freedom to pursue my research.

Many thanks go to Prof. Castrodeza, for sharing his evaluable expertise in the field of 'Fracture Mechanics' and more importantly to really made me feel welcome in his Lab. and in Rio 'a Cidade Maravilhosa'.

To my friends, near and far, for the moments spent and shared, for listening and laughing. Thanks to my long life girlfriends Annalisa, Anita e Giorgia, for always being there. To Alberto e Andrea for mental escapes. To "Valentines" for soul cleaning. To Dina, Laura, Ales, Ari, Vez, Lori for waiting for me with open arms, there is no Parma besides you. To Nadia, Mohammed, Luciana, Patricia, Joao, Marco, Alfredinho for showing and most importantly sharing all the best of the stunning Rio (I'll be back!). To Luca, Adrian, Mirko, Rosa, Sole and Corrado because 'company in distress makes trouble less' or, as we say "mal comune mezzo gaudio"!

Finally, I thank my dearest love for your endless support, encouragement, patience and understanding. Thank you for never leaving my side.

Summary

The use of Al-Si alloys in various applications such as automotive and aerospace has recently increased in the light of their good castability, lightness, low strength-to-weight ratio and corrosion resistance. Among this class, Al-Si-Mg foundry alloys are found to give good results since they show concurrently excellent casting characteristics and mechanical properties. In view of the two room and high temperature applications, enhanced static and dynamic properties are required and, indeed, coarsening resistant strengthening phases are needed. To pursue this goal, two main paths can be followed, namely: (i) chemical modification of Al-Si-Mg alloys; (ii) Heat Treatment Optimization. Both the paths are meant to induce the formation of thermally stable strengthening phases.

Aluminum is produced by the Hall-Héroult electrochemical reduction of aluminum oxide dissolved in a molten salt. The deterioration in the current coke quality for anode production has led to increase the amount of metal impurities such as Ni and V in primary aluminum. In the next years, the levels of Ni and V are expected to rise. At the present, there is no cost effective or efficient method available for removal of these impurities. Therefore, industries are developing a growing interest with respect to the effect of increased Ni and V levels on the properties of aluminum alloy products. In the last decade, aluminum alloys have been re-focused in term of lightweight material for vehicles. Considering the new trends, it is of importance understand which role is played by the Ni- and V- addition on the high temperature mechanical behavior. Currently, the EN 1676-2010 standard specifies the maximum concentration limit only for V of 0.03wt% for EN-AB aluminum foundry alloys (A356 alloy), whereas there are no indications for the maximum tolerable Ni level in this group of alloys. Hence, the first part of this research activity is meant to evaluate the influence of Ni and V trace elements on the high temperature tensile properties of as-cast and T6 heat treated A356 unmodified foundry alloys in both sand and permanent mold casting process.

Alloy composition and cooling rate play a key role on the castability and also on the mechanical properties of Aluminum-Silicon cast alloys. The cooling rate controls the microstructural features of the material including the Secondary Dendrite Arm Spacing (SDAS), which is often used as measure of the grain size of the material, and thus as measure of the mechanical response. The fraction, size, shape and distribution of eutectic

silicon particles and intermetallic phases also give a crucial contribution in connection with microstructure optimization. Industries, especially in the automotive sector, are paying attention in finding suitable chemical compositions for cast aluminum alloys for high temperature applications. The concomitant presence of the two copper and magnesium in Al-Si-Cu-Mg alloys should in fact enable the precipitation of more stable Cu-based intermetallic precipitates at higher temperatures, leading to enhanced thermal stability of the T6 heat treated alloys. In this concern, part of this thesis offers a combined overview of the two aspects of SDAS and Cu additions on the as cast A356 alloy.

Optimization of solution heat treatment represents a necessary pillar to improve the aging response of Al-Mg-Si alloys with Cu additions. It has been reported that during artificial aging, Cu content influence the aging precipitation sequence, number and density of precipitates, and eventually improve the contribution to strength. Even though some reports show no difference in precipitation kinetics in the quaternary as compared to the ternary alloys (Al-Si-Cu-Mg vs. Al-Si-Mg), a wide literature suggests the existence of different precipitates types after artificial aging, and, in particular, a double aging peaks have been sometimes observed in Al-Si-Cu-Mg alloys. The influence of the aging parameters on the tensile response has been extensively on high Cu alloys (up to 5 wt. %), while few works were conducted on Al-Si-Cu-Mg alloys containing up to 1 wt. % Cu. Article 3 in the present collection examines two solutionizing temperatures and two artificial aging temperatures in Al-Si-Mg alloys having 0 wt. %, 0.5 wt. %, and 1 wt. % Cu content. Mechanical properties in connection with precipitation behavior during artificial aging have been also investigated.

The past two decades have been marked by great progress and innovation in the aluminum foundry industry. However, the low ductility and fracture toughness, as compared to the wrought aluminum alloys counterpart, still represent one of the major impediment for increased use of aluminum casting aerospace industry. With improving molten metal quality and foundry technology, cast alloys are expected to be used more commonly in critical applications. So far, the lack of knowledge towards the fracture toughness of these alloys had limited their use to field where fracture toughness related properties were not relevant. Though, fracture toughness evaluation in Al-Si alloys might
represent a strategic point to understand the metallurgical features which control the toughness and hence will might allow proper material specifications to be settled for those

applications where toughness-related failure must be prevented. In this framework, Article 4 proposes a study on the fracture toughness of a A356 Al alloy and its Cu-containing (1wt.%) variant, under four different aging conditions. The toughness was obtained through crack growth resistance curves (J-R curves) which were determined by the unloading compliance method. In order to assess the mutual influence of casting defects and alloys hardness, as resulting after aging treatments, hardness results have been composed together with porosity values, and finally integrated with the J_{IC} values. In addition, microstructural observations were carried out to endorse the fracture mechanism.

Good castability of Al-Si alloys, characterized by high melt fluidity, narrow solidification range associated with eutectic, and low shrinkage with low hot tearing tendency, makes Al-Si alloys readily available for the emerging additive manufacturing (AM) technology. Among the AM technologies, the Selective Laser Melting (SLM), has been experiencing a large growth since the past few years due to his high flexibility, versatility and customizability and it is now suiting most sectors of industrial production. The SLM technology involves layer by layer melting of the metallic powder by means of a high-power laser beam according to the instructions provided by CAD files. The process is characterized by high temperature gradients leading to rapidly solidified, non- equilibrium microstructures, causing a substantial residual stress development. As a consequence, the mechanical properties of SLM parts can differ substantially from one another and from those produced by conventional techniques. In order to meet the full potential that the SLM has to offer, especially for flight-critical components, studies and qualifications are needed. In this light, article 5 examines the high cycle fatigue crack growth behavior in the linear region of da/dN vs. ΔK diagrams (described by the Paris law) of AlSi10Mg alloy for different experimental conditions. The Fatigue Crack Growth (FCG) curves revealed the beneficial influence of the heat treatment on the FCG response, as compared to the as-built case. On the other hand, the latter' fatigue crack growth behavior is found to be strongly dependent on the material orientation. Fractographic analysis and residual stress measurements have been further performed to understand the mechanisms involved.

Sommario

Le leghe di alluminio con Si come maggiore alligante, sono le più utilizzate tra le leghe di fonderia; grazie all'elevata colabilità, leggerezza, resistenza specifica e resistenza a corrosione. Ciò spiega l'uso crescente che ne è stato fatto negli ultimi anni, in particolare nell'ambito aerospace e automotive. Le applicazioni di tali leghe interessano sia la temperatura ambiente che le alte temperature e, a tal riguardo, assicurare elevate proprietà meccaniche (sia statiche che dinamiche) è di fondamentale importanza. L'obiettivo presunto può essere raggiunto percorrendo due strade: (i) modificando la composizione chimica delle leghe Al-Si-Mg, (ii) ottimizzando i trattamenti termici. Il fine ultimo delle due opzioni è quello di promuovere la formazione di precipitati con alta stabilità termica.

Recentemente, nell'alluminio primario, prodotto grazie al processo Hall-Heroult, si è notata una crescente concentrazione di impurezze metalliche e di elementi in tracce. Tale inquinamento, si riflette nel graduale incremento del contenuto di impurezze nei lingotti di alluminio primario. Monitorando l'inquinamento del coke di petrolio, si prevede nell'immediato futuro una crescita delle quantità di Nichel (Ni) e Vanadio (V). Questa tematica accende l'interesse industriale, dato che, ad oggi, non sono disponibili tecniche efficaci ed economiche per la purificazione del metallo dai suddetti elementi. Quindi, tenendo conto del progressivo inquinamento del coke e delle normative attualmente vigenti (EN 1676-2010), che specificano il limite massimo per il solo Vanadio (V < 0.03 wt. %), parte del presente lavoro di tesi è volto alla valutazione dell'influenza dell'aggiunta di Ni e V in tracce, sulle proprietà meccaniche a caldo sulla lega Al-Si-Mg A356. La definizione delle proprietà meccaniche ad alta temperatura è stata condotta esaminando campioni in lega A356 non modificata, colata sia in sabbia che in conchiglia, aggiungendo quantità in tracce di Ni o V.

Le proprietà meccaniche e la colabilità delle leghe da fonderia a base Alluminio-Silicio, sono fortemente dipendenti dalla composizione chimica e dalla velocità di raffreddamento. Quest'ultima infatti, governa la microstruttura del materiale, a partire dal parametro di SDAS (Secondary Dendrite Arm Spacing), che è spesso usato come misura della "dimensione" del grano del materiale, e quindi, della sua risposta meccanica. In relazione alla microstruttura, un parametro che determina significativamente la risposta meccanica è il Si eutettico. In particolare, parametri relativi al Si, come la frazione percentuale, la

distribuzione, la dimensione e la forma possono essere ottimizzati in funzione dei risultati attesi. Riguardo questa classe di leghe, l'attenzione dell'industria, specialmente nel settore automotive, è rivolta a trovare nuove composizioni chimiche utilizzabili anche alle alte temperature. A tal proposito, la concomitante presenza di Rame (Cu) e Magnesio (Mg) nelle leghe Al-Si-Cu-Mg dovrebbe promuovere la precipitazione di intermetallici a base Cu, più stabili alle alte temperature, e conseguentemente contribuire ad una migliore stabilità termica delle leghe trattate termicamente. Il secondo lavoro presente in questa collezione di articoli offre una valutazione combinata della duplice influenza del parametro di SDAS e delle aggiunte di Cu sulla lega A356 non trattata termicamente.

L'ottimizzazione del trattamento di solubilizzazione, rappresenta un passaggio chiave per migliorare la risposta all'invecchiamento delle leghe Al-Si-Mg con l'aggiunta di Cu. Durante l'invecchiamento artificiale, la presenza del Cu ha effetto sulla sequenza di precipitazione, sulla densità e la tipologia di precipitati, e in fine sul rafforzamento. Ad esclusione di qualche lavoro, buona parte della letteratura mostra, confrontando le leghe quaternarie con le ternarie (Al-Si-Cu-Mg vs. Al-Si-Mg), una chiara differenza nella cinetica di precipitazione, e indica la presenza di una diversa tipologia di precipitati. Occasionalmente, sono state osservate nelle leghe Al-Si-Cu-Mg, curve con un duplice picco di durezza. L'influenza dei parametri di trattamento termico sulla risposta meccanica è stata largamente studiata nelle leghe con alti tenore di Cu, mentre è molto limitata la letteratura inerente alle leghe Al-Si-Cu-Mg avente contenuto di Cu inferiore al 1 wt. %. A tal proposito l'articolo 3 di questa tesi presenta uno studio della lega Al-Si-Cu con contenuto variabile di Cu (0 wt. %, 0.5 wt. %, e 1 wt. % Cu) soggetta a due diverse temperature di solubilizzazione e rispettivamente, due differenti temperature di invecchiamento. Inoltre, l'analisi ha interessato anche la riposta meccanica in connessione con i diversi fenomeni di precipitazione.

Negli ultimi decenni, il mondo industriale della fonderia, è stata caratterizzato da un forte progresso tecnologico e innovativo. Tuttavia, la scarsa duttilità e la bassa tenacità a frattura dei getti, rispetto alle leghe da deformazione plastica, rappresenta ancora uno dei maggiori ostacoli per incrementare l'uso dei fusi di alluminio nell'industria aereonautica.
A seguito del recente miglioramento della qualità dei getti di alluminio e delle tecnologie di fonderia, ci si aspetta che l'uso leghe di alluminio da fonderia vada via via ad interessare settori di applicazione più critici. Fin ora, la mancanza di dati, riguardo le proprietà di

tenacità a frattura di queste leghe, ha ristretto la loro applicazione in campi dove tali proprietà non sono di interesse primario. Dunque, lo studio della tenacità a fratuttura nelle leghe Al-Si, sembra essere di fondamentale importanza per comprendere i fenomeni metallurgici che controllano tali proprietà, per poi successivamente rendere questi materiali servivibili ad applicazioni ben più critiche ove la tenacità a frattura è prioritaria. Riguardo a ciò, l'articolo 4 della presente raccolta, presenta uno studio sulla tenacità a frattura di una lega A356 base e di una sua variante contenente l'1 wt. % di Cu, per quattro diverse condizioni di invecchiamento. I valori di tenacità sono stati ottenuti attraverso le curve J-R di propagazione alla frattura, determinate con il metodo 'unloading compliance'. L'analisi ha preso in considerazione due aspetti fondamentali: la presenza di porosità (difetto intrinseco della tecnologia di fonderia) e la durezza (in funzione dei diversi trattamenti di invecchiamento proposti). I valori ottenuti sono stati successivamente combinati e correlati con i valori di tenacità ottenuti, $J_{IC.}$ L'intero studio è stato supportato da analisi microstrutturali (ottiche e SEM), volte inoltre a chiarire il meccanismo di frattura.

In conclusione, vista la crescente attenzione attorno al tema Additive Manufacturing (AM), sia nell'ambito industriale che scientifico, il presente lavoro offre uno spunto inerente alla caratterizzazione meccanica di una lega Al-Si, prodotta con tecnologia additiva. Difatti, l'ottima fluidibilità, la rapida solidificazione associata alla fase eutettica, la bassa criticità in termini di ritiro e'hot tearing' rendono le leghe della classe Al-Si, candidate perfette per l'emergente mercato della fabbricazione additiva. Tra le tecnologie AM, la tecnologia 'Selective Laser Melting' (SLM) è sicuramente la più diffusa e, grazie alla sua alta flessibilità e versatilità la si trova sempre più impiegata in diversi settori industriali. L'innovazione di tale tecnologia è nel processo stesso e consta di una deposizione strato su strato di un letto di polveri, fuse ad opera di un fascio laser ad alta energia, e istantaneamente solidificate. La spinta versatilità e quindi la possibilità di poter personalizzare il prodotto risiede nel fatto che la movimentazione del fascio e di conseguenza la geometria del manufatto finale, è coordinata da un file CAD. Le polveri nel corso del processo, sono soggette a grandi gradienti termici che inducono una rapida

solidificazione oltre che la formazione di microstrutture instabili che causano forti e distinte concentrazioni di tensioni residue. Di conseguenza, le proprietà meccaniche di questi manufatti possono variare molto tra loro, oltre che risultare molto diverse se confrontate

con la loro controparte prodotta con tecnologie convenzionali. Studi e qualifiche sono quindi necessari al fine di comprendere e sfruttare a pieno tutto il potenziale che la tecnologia SLM ha da offrire. A tal proposito, parte del nostro studio è volto alla valutazione della propagazione di cricca a fatica nella regione lineare of da/dN vs. Δ K (descritta dalla legge di Paris) in una lega AlSi10Mg per diverse condizioni sperimentali. In particolare, le curve di propagazione di cricca a fatica hanno evidenziato una risposta positiva all'influenza del trattamento termico rispetto al caso as-built. Inoltre, si evince che la resistenza a propagazione di cricca in quest'ultimo caso, appare essere strettamente correlata alla direzione di accrescimento dei campioni. A conferma dei risultati mostrati dalle curve di resistenza, sono state investigate le superfici di frattura e misurate le tensioni residue, al fine di comprendere il meccanismo di frattura.

Table of Content

Part 1

Part 2

Articles

1. Theoretical Background

1.1 Al-Si Alloys

Al-Si foundry alloys are widely used in the automotive and aerospace industry due to their good castability, lightness, low strength-to-weight ratio and corrosion resistance. Silicon increases the fluidity in aluminum casting alloys, reduces the melting temperature and the thermal expansion coefficient and diminishes the tendency of the alloy toward shrinkage and hot tearing. Among the commercial aluminum alloy castings, Al-Si based foundry alloy constitutes 85-90% of the total aluminum cast part produced [1]. The Al-Si system is a simple eutectic system. The two solid solution phases are FCC Al and Diamond-cubic Si (Figure 1). Al-Si alloys are divided into three groups: 1) Hypoeutectic containing 5-10% silicon 2) Eutectic containing 10-13% silicon 3) Hypereutectic containing 13-25% silicon. The maximum solubility of Si in Al is 1.5 at. % at 577 °C and it falls to 0.05 at. % at 300 °C. The maximum solubility of Al in Si is 0.016 at. % at 1190 °C and becomes minor at lower temperatures [2]. The only invariant reaction for the Al-Si system is a eutectic reaction (Liq. → Al(s) + Si(s)). The eutectic temperature is 577 °C for a Si content of 12.2 at. %. Alloys to the left of the eutectic point are called as hypoeutectic while alloys to the right are termed hypereutectic. Solidification in hypoeutectic alloys starts with the formation of primary α-Al dendrites. Further cooling leads to the growth of this solid solution phase: dendrites develop as a rigid network and finally coarsen. Si is progressively rejected into the residual liquid until the eutectic temperature is reached. When the undercooling is large enough, the final eutectic reaction occurs. Differently, solidification in hypereutectic alloys initially involves the formation of polyhedral primary Si crystals and, when the eutectic temperature is reached, finalizes with the eutectic reaction. In commercial Al-Si alloys (commonly not pure binary systems), Si content varies in the range 5-22 wt. %. The lower Si restriction is meant to guarantee the “fluidity” and “feedability” necessary for the casting technology, owing to Si high latent heat of fusion. Where the upper limited is set assure the minimal amount of plasticity in the alloy. Moreover, the growth of Si particles during solidification partially compensates for the contraction of Al and, as results, counteract the shrinkage and hot tearing phenomena. In addition, Si phases exert a dominant role in controlling Al-Si alloys’ mechanical and

physical properties [3]. Besides Si-phases, several intermetallics may form prior or post the eutectic reaction in commercial Al-Si alloys.

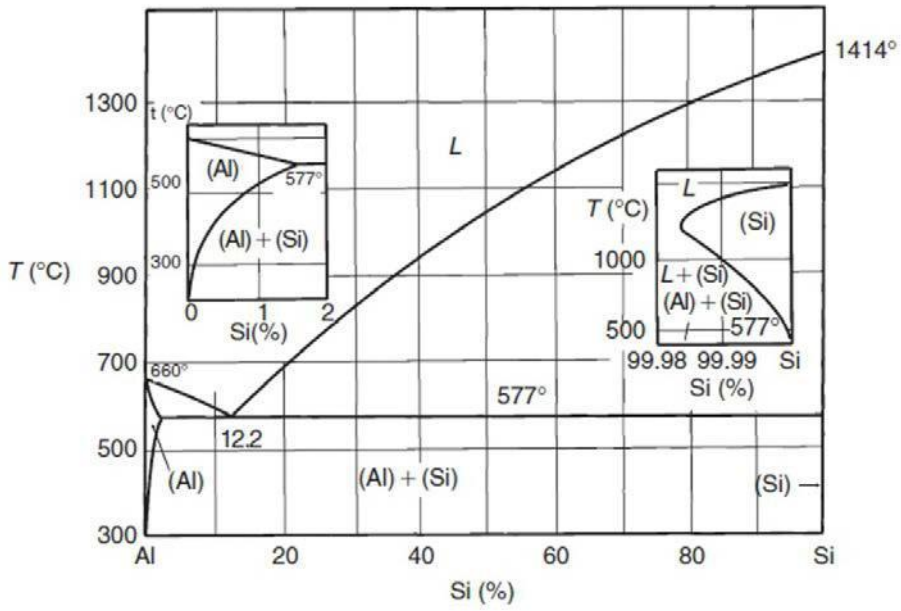

Figure 1- *Phase diagram of the binary Al-Si system. [1]*

1.2 Trace element impurities

Based on the source of raw materials used for production, Al-Si alloys are classified into primary and secondary alloys. Secondary alloys are obtained by recycling and re-melting the correct base alloy charge of scrap metal in combination with melt treatment operations e.g. cleaning and fluxing are widely used to reduce inclusions, hydrogen content or major impurity elements. While primary alloys are made from pot line Al, higher grade Si and other desired alloying elements are added in the form of different binary master alloys to reach customer tailored properties of the final casting. Severe control of detrimental impurities on trace element level is crucial to ensure a consistent performance of the final casting. This is expected to become even more critical as one of the future trends will be to use a higher fraction of secondary metal in the primary alloy production. Hence, aluminum producers worldwide are currently facing major challenges to keep their alloy composition within the tight customer specifications as raw material quality for the primary Al production steadily decreases or is subject to considerable fluctuations depending on the location of raw material deposits. Impurity issues in primary Aluminum smelting have

historically been focused on the control of particles and dissolved hydrogen and alkali earth metals. However, an emerging problem is the increase in certain impurities, such as Ni and V. Both of them come principally from the anodes of the Hall-Héroult electrolytic process, but in the case of the Vanadium, a small contribution is given by the Alumina [4]. Considering the decrease in quality of petroleum coke observed in recent years (Figure 2), trace elements and metal impurities are expected to rise in the future with significant implications for the ability of cast houses to meet customers' chemical specifications. It is reported that the Ni and V content in the coke will enrich concentrations of 420 and 1080 ppm, respectively [5]. Currently, there is no cost effective or efficient method available for the removal of these impurities, and the response to the problem is mainly monitoring the V and Ni levels and checking for any negative influence [4].

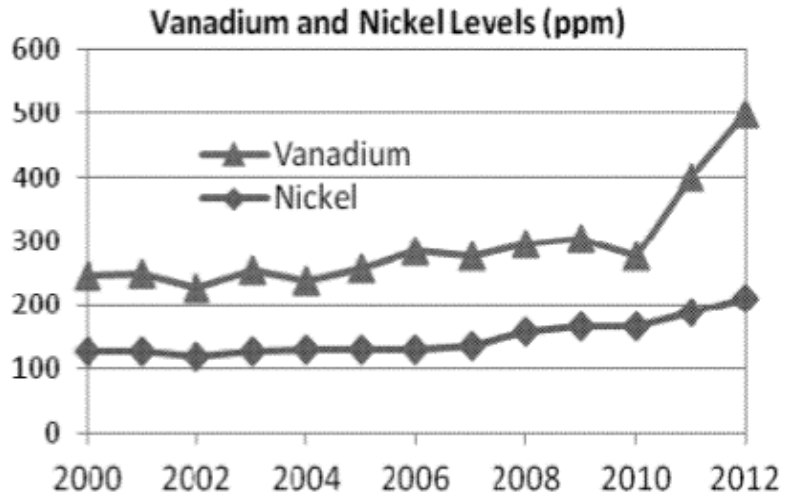

Figure 2 - *V and Ni Level in Petroleum Coke [6].*

1.2.1. The influence of Nickel and Vanadium impurities in Al-Si Alloys

Nickel (Ni) has a low distribution coefficient ($K_d = C_s/C_l$), and it is reported that it remains in the liquid until the later stages of solidification. In commercial Al-Si alloys, where Fe is present as an impurity, Ni is more likely to be associated with iron, i.e. in AlFeSi intermetallics and eventually segregate at the grain boundaries, than be dissolved in the α-Al matrix. There is a lack of information about the Ni additions below 1000 ppm in the Al-Si foundry alloys. Grandfield et al. [7] studied the effect Ni and V combined additions of

300 ppm of each in a AA6063 and A356 alloys. In the as-cast condition, the Ni was mainly found in the intermetallic phase, the π-$Al_8Mg_3FeSi_6$ in an AlSiNi phase with unknown stoichiometry. Mechanical Properties were weakly influenced, nevertheless no significant differences were noticed in the corrosion. Zhu *et al*. [8] evaluated the influences of Ni addition, varying from 80 ppm to 500 ppm in a A356 alloy, results were in concordance with the work conducted by Grandfield et al., though an identified AlSiFeNi phase was detected. Moreover, as documented by Garci [9], brittle Al_3Ni particles were detected in Al-7wt%Si alloy containing 0.5 and 0.1 wt% of Ni. These particles exercised a negative effect on the tensile properties, decreasing strength, elongation and hardness. T.H. Ludwig *et al*. [10] studied the influence of Ni addition in both high purities binary Al-7wt%Si and commercial purity A356 foundry alloys. Ni addition, over 300 ppm, resulted in the formation of the two Al_3Ni and Al_9FeNi intermetallic phases. The first one was fine and distributed in the immediate vicinity of the eutectic Si crystals in both the alloys, while the second one occurred in the commercial alloys, forming distinct script or oval shape particles in the proximity of the π-$Al_8Mg_3FeSi_6$ phase. In another work [11] the high temperature strength of Al-7 wt%Si and Al-12 wt%Si was investigated. The as-cast microstructure consisted of a network of interconnected Si lamellae and 3D shape Ni-rich intermetallics. After the solution heat treatment, the stability of the Si-eutectic network was stabilized by the Ni-rich intermetallics that maintain their contiguity to the spherodized Si particles. As result the high temperature strength at 250 °C and, in particular, the yield strength was evidently enhanced. The optimal concentration was established at 1 wt. %. In the end, D.Casari *et al.* [12] reported that Ni addition of 0.06 wt. % strongly influenced the tensile properties of the sand cast A356 alloy in as-cast condition, leading to a reduction of both the Yield Strength and Ultimate Tensile Strength by 87% and 37%, respectively. Ni-rich intermetallic where observed in the fracture surface, prone to fracture more easily than other secondary phases.

Vanadium (V) is a slow diffusing peritectic element, showing the maximum solubility (~ 0.4 wt. %) at the peritectic temperature of 611°C [13]. In most cases V resides in the Al matrix [14] whereas V containing intermetallic particles are unlikely to form below the concentration of 0.1 wt.%. Is reported by Mondolfo [15] that V, and in particular the peritectic precipitation of Al_3V, had some beneficial effect on the grain refinement, even thought it was less efficient than Ti and/or B. Grandfield et al. [7] evaluated the influence

of 0.03 wt.% V addition in both AA6063 and A356 alloys, showing a very moderate effect on the tensile properties. Further investigations on A356 alloy in the as-cast condition [4] revealed an increase in strength, due to the solid solution strengthening effect produced by the addition of 0.1 wt.% V. As stated by T.H. Ludwig [16], increasing the V content from 0.06 wt.% to 0.8wt.% in a A356 foundry alloy resulted in a shift of nucleation, minimum and growth temperature of the α -Al by up to 4.5K, whereas the undercooling was not affected. No influence on the grain refinement was discovered. Polyhedral Si_2V phases were detected beyond the concentration of 0.06 wt.%, and the β-Al_5FeSi phases began enriching in V with increasing nominal V addition, with changes in morphology from needle to script like.

1.3 The A356 alloy

Alloy A356 is a high-purity version of the well-known casting alloy 356, and belongs to a group of hypoeutectic Al-Si alloys. It is designed as EN AB-42100, according to the EN 1676-2010 specifications. In accordance with the Aluminium Association designation system for cast alloys, a capital letter (*A, B, C*) before the digits indicates a variation in the chemical composition of the base 356 alloy with respect to the amount of Fe, which varies from 0.04 wt% (best primary metal, corresponding to the letter C) to 0.50 wt% (secondary metal), with typical primary levels in the 0.10 - 0.20 wt% range (letter A).Besides Si, other main alloying elements presents in the A356 alloys are Mg, Fe and Mn, which are added in form of master alloys by design or are unavoidably derived (as impurities) from the primary Al production, scrap recycling or manufacturing processes. Other elements such as Na, Sr, Sb, Ti and B, are also intentionally added in the melt during the casting process in order to induce specific transformation in the microstructural features modification. The as-cast microstructure consists of primary dendrites of α-Al containing magnesium and silicon in solution, surrounded by an Al/Si eutectic phase. The size and morphology of the eutectic silicon depends on the casting conditions, as well as the presence of chemical modifiers such as strontium, sodium or antimony. Without modification the eutectic silicon forms as coarse platelets, shown in Figure 3.a, whereas a fine ‘fibrous’ or ‘coral-like’ structure occurs in modified alloys, Figure 3.b. Other phases found in commercial A356 alloys include

Mg_2Si particles, which are taken into solid solution and precipitated during heat treatment, and Fe-rich phases including α-Al_5SiFe, β-Al_8Si2Fe and π-Al8Mg3Si6Fe, as Fe arise from the presence of melt impurities. The presences of the Fe-bearing compounds influence the ductility of the alloy [17]. Volume and shape of these intermetallic depend on the Mg content [18,19] and on the cooling rate respectively. In most cases the alloy is subject to heat treatment, and as a result, several combinations of tensile and other mechanical properties can be provided. According to Arnberg et al. [20], the solidification sequence, of this class of alloy includes: initiation of solidification at 610 °C and subsequent formation of α-Al dendrites, starting of the main eutectic reaction at 568 °C (from Liquidus to Al + Si + Al_5FeSi), precipitation of Mg_2Si at 557 °C (from Liquidus to Al + Si + Mg_2Si), finally precipitation of complex eutectic phases at 550 °C (from Liquidus to Al + Si + Mg_2Si+ $Al_8Mg_3FeSi_6$). During the nucleation of α-Al starts at 610°C, equiaxed dendritic crystal begins evolving, and become coherent at 604°C. The eutectic reaction starts at 568°C, and the fist β-Al_5FeSi platelets begin to appear. Under continued solidification the Mg_2Si phase and the π-$Al_8Mg_3FeSi_6$ phase precipitate.

Table 1- *Chemical composition of the A356 foundry alloy in accordance with EN 1676-2010 specification. No specific information about the maximal tolerable Cr, Ni, Pb and Sn concentration is given.*

A356 - EN AB-42100

Element	**Composition [wt.%]**
Si	6.50 - 7.50
Mg	0.30 - 0.45
Fe	0.15
Cu	0.03
Mn	0.10
Zn	0.07
Ti	0.18
Others	0.03 (each) 0.10 (total)
Al	bal.

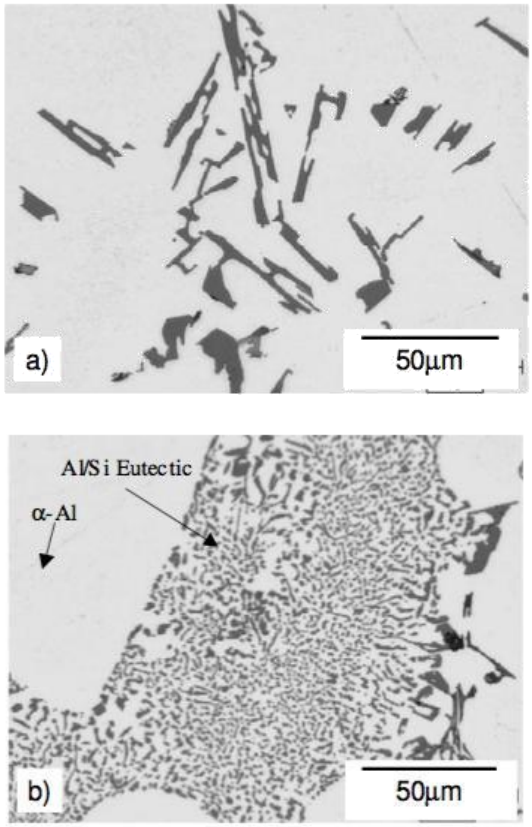

Figure 2 - *Microstructure of Al/Si eutectic phase in an as-cast A356 aluminum alloy;(a) Unmodified alloy, (b) Modified with an addition of 156ppm strontium [21].*

1.3.1 The influence of Mg in A356 alloy

Magnesium is generally added into the A356 foundry alloy with the aim to induce age hardening through the precipitation of fine Mg_2Si dispersoids into α-Al matrix, and hence blocking dislocation movement, improving significantly the mechanical properties. Edwards et al. [22] reported the following precipitation sequence upon ageing: Supersaturated Solid Solution (SSSS) → independent clusters of Mg and Si, co-clusters of Si and Mg → Guinier-Preston (GP) zones → Si rich phase → β'' → β' → β. GP zone are clusters of solute atoms (meta-stable phases or precipitates) crystallographically coherent with the matrix. When Mg is added to the alloy in the composition range of 0.30 - 0.45 wt. % (as specified in Table1), GP zones are observed as fine plates with a thickness of one atomic layer (≈ 2.5 nm) and a length of about 30 nm. GP zones are generated

randomly in the matrix and their distribution impact also the matrix dislocations [23-25]. GP zones consists of interchanging arrangement of columns of Mg and Si atoms along the $(100)_\alpha$ direction, with a chemical composition of Mg:Si = 1. They might continue to cluster with increasing aging time, and in this case, their morphology evolves to form needle like precipitates. The β'' transition phase, whose chemical composition is Si:Al:Mg = 6:3:1, also shows a needle-like shape (Figure 3.a). Calorimetric studies revealed that the formation of GP zones and β'' precipitates are parallel and competitive processes [26] and that the transition from GP zones to β'' proceeds without the dissolution of the former precipitates [22]. These two phases are easily sheared by dislocations due to their coherency with the matrix and small size. The high degree of dispersion homogenizes the slip distribution in under aged alloys, so that local strain concentration at grain boundaries and consequent intergranular fracture are reduced. The following sequence concerns the transformation of β' phase (Figure 3.b), which offer a lower Mg:Si ratio (≈ 1.7) as compared to the equilibrium phase β-Mg_2Si [27]. The β' precipitates are partially coherent with the matrix and also lie along the $(100)_\alpha$ direction. However, they cannot be shared by dislocations due to their rod-like morphology. Henceforward, the β' transition precipitates contribute to strength's enhancement by Orowan looping (Figure 4). Further aging leads to the final precipitation of the equilibrium phase β-Mg_2Si, which consists of non-coherent platelets that marginally support the strength of the alloy [28].

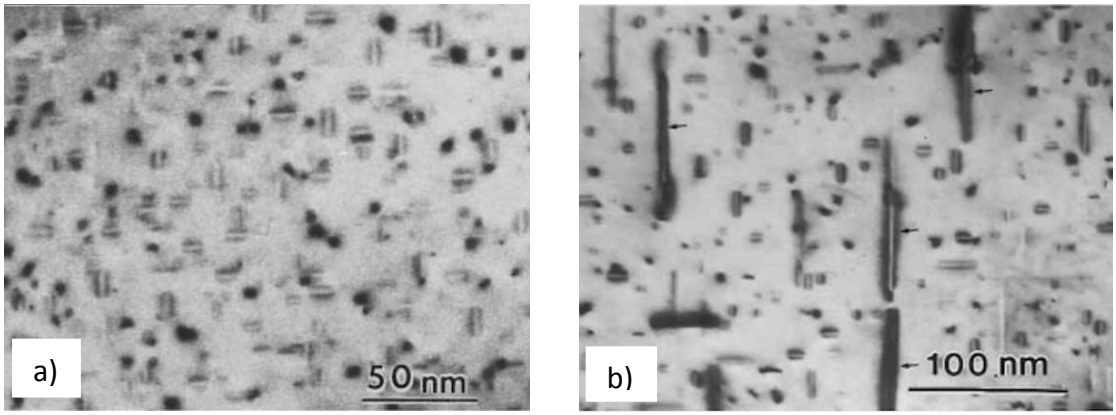

Figure 3 - *TEM images of Mg-rich precipitates at different stages of artificial ageing: a) β'' needle-shaped dispersoids after 4h at 175 °C, b) β' rod-like precipitates after 20h at 200 ◦C [*22].

Besides the role played by the Mg in solid solution strengthening and hence precipitation hardening, his undesirable tendency to promote casting defects [19,30] represent a critical drawback for structural application; moreover, β-Mg_2Si precipitates tend to become coarse at high temperature [31].

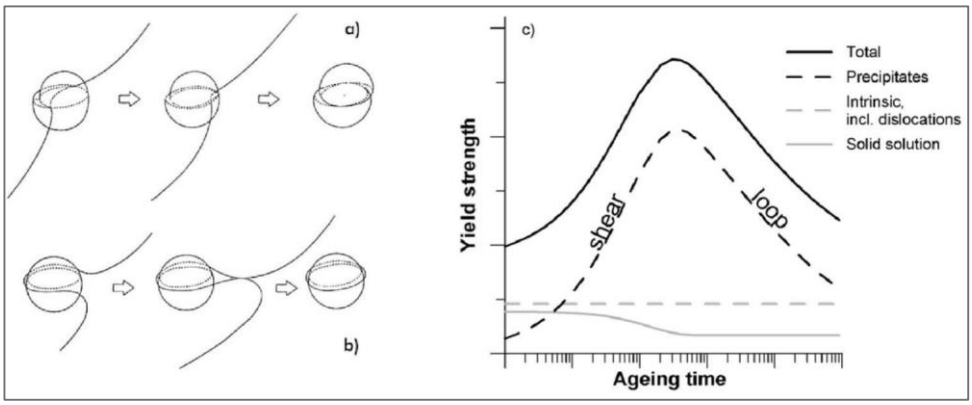

Figure 4 – *Orawan dislocations passing mechanism: a) shearing, b) looping, c) different strength contributions to the total yield strength [29]*

1.3.2. The addition of Cu in A356 alloy

As just mentioned, precipitation hardening is an efficient strengthening mechanism at room temperature, however high operating temperatures may strongly reduce the ability of precipitates to hinder dislocation movement. After long-term high temperature exposure, in fact, precipitates gradually undergo to coarsening. The mechanism at the basis of precipitates coarsening with overaging is usually referred to as Ostwald ripening, and consist in the growth of precipitates at the expense of the smaller ones. Ripening process is governed by diffusion: shrinking precipitates gradually loose atoms, moving towards the growing ones. The variation of precipitates average size with time is described by Lifshitz-Slyozov-Wagner in [32,33]. In view of the current increase in the maximum operation pressure/temperature of combustion engines, however, it is necessary to increase thermal resistance of aluminum alloys. In this concern, the addition of Cupper (Cu) to traditional Al-Si-Mg alloys has been recently investigated [34-36]. In particular, the concomitant presence of both copper and magnesium in Al-Si-Cu-Mg alloys should in fact enable the precipitation of more stable Cu-based intermetallic precipitates, leading to enhanced thermal stability of the T6 heat treated alloys [37]. Further than β' (Mg_2Si) and θ' (Al_2Cu)

precipitates, present in ternary Al-Si-Mg and Al-Si-Cu alloys [37–42], reinforcing compounds such as the S' phase (Al_2CuMg) [41,43,44] and the Q' phase (whose general stoichiometry is $Al_5Cu_2Mg_8Si_6$) are found in quaternary Al-Si-Cu-Mg alloys. It is worth to mention that the type and the volume fraction of Cu-rich and Mg-rich precipitates are highly dependent on the heat treatment regimes, the Cu content and the Cu/Mg ratio [35,45-47], As recently reported by Farkoosh et al. [34], the quaternary Q' phase is expected to give the most relevant contribution to thermal stability enhancement, being the only age-hardening stable phase after soaking at 300 °C for 100 h [34].The mechanisms which confer higher coarsening resistance to Q phases are still however under debate [34,48,49].

1.4. Heat Treatment in Al-Si-Mg and Al-Si-Cu-Mg alloys

Ternary Al-Si-Mg and quaternary Al-Si-Cu-Mg alloys are generally subjected to heat treatment. Heat Treatment encompasses three main steps: (i) Solutionizing, (ii) Quench, (iii) Aging. (i) Solutionizing, is the process of heating a metal alloy to form a homogeneous solid solution. Further, under solutionazing temperatures (490- 540 °C), coarse Mg- and Cu-bearing intermetallic particles, formed during solidification, are dissolved. (ii) Quench, is a cooling process, usually performed out in hot (~ 50-60 °C) or room temperature, meant to retain Mg and Cu atoms in supersaturated solid solution. (iii) The process of aging is designed to induce the precipitation of strengthening phases from the supersaturated solid solution. Aging can be natural or artificial. The former is conducted at room temperature for long time exposures. The latter, is usually carried out in the range 150-200 °C for times varying from 1 h to 24 h, depending on the alloy chemical composition and on the treatment scope.

1.4.1. Solutionizing Treatment in Al-Si-Mg and Al-Si-Cu-Mg alloys

Solutionizing treatment parameters in Al-Si casting depend on the nature of the diffusing atoms, on the temperature chosen and on the material microstructural fineness (i.e. to SDAS) [22,50]. The coarse intermetallic particles formed during solidification in Al-Si-Mg and Al-Si-Cu-Mg show different tendency to dissolution. β-Mg_2Si and θ-Al_2Cu phases

are generally easy to dissolve; on the contrary, other Cu bearing phases, such as the Q-$Al_5Cu_2Mg_8Si_6$ are usually reported to be rather stable with solution treatment. Further, Fe-rich phases are usually difficult to be dissolved, such as the α-$Al_{15}(Fe, Mn)_3Si_2$ phase or the typical needle like β-Al_5FeSi, which undergoes gradual dissolution only after long term solution at high temperature. One of the most characteristic phases found in the as-cast microstructures of Cu containing cast aluminum alloys (both Al-Si-Cu and Al-Si-Cu-Mg) is the θ-Al_2Cu phase. θ particles nucleate both around β-Al_5FeSi plates or in the proximity of eutectic Si particles during the last solidification stages. θ-Al_2Cu phases are generally observed in two main morphologies: blocky and eutectic. Nevertheless, mixed morphologies have been also observed [51,46]. It is reported that high solidification rate may promote the formation of eutectic morphology, whereas, the addition of Sr as modifier may promote the formation of θ blocky phases [52]. The dissolution of eutectic Al_2Cu occurs through necking, gradual shperoidization of the smaller particles after necking and diffusion of Cu atoms into the adjacent aluminum matrix [51,53,54], while in the case of block-like Al_2Cu there is no necking, and spheroidization and diffusion take place at a lower rate (Figure 5) [51,53].

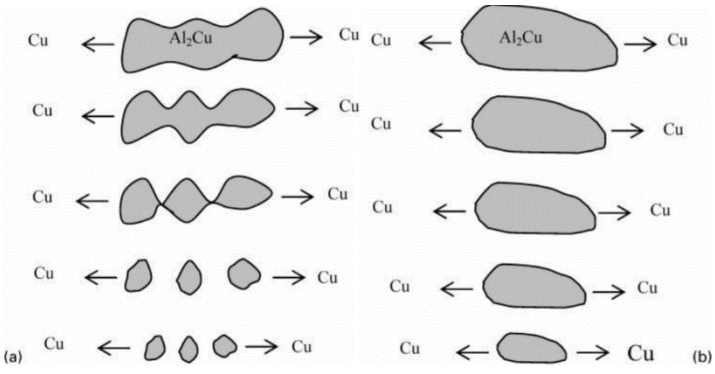

Figure 5 – *A schematic presentation of the dissolution of a) eutectic and b) blocky Al2Cu [51,53]*

Compared to the θ particles the dissolution of Mg_2Si phases in Al-Si-Mg or Al-Si-Cu-Mg alloys are faster, thanks to the high diffusion rate of Mg in Al. Further in Al-Si-Mg alloys, the rapid dissolution of Mg_2Si is assisted to the high solution temperature (~540 °C), which may be significantly higher than that employed in Al-Si-Cu-Mg, aiming to avoid the incipient melting of Cu-low melting phases. In this concern, many studies have been conducted to stablish the influence of Mg on the dissolution time parameters [55-57].

Moreover, Fe-based phases are generally present in these classes of alloys. Fe-bearing phases show a lower tendency to dissolution in comparison to the previous ones, due to the high melting point associated to Fe. As a matter of fact, the β-Al5FeSi phase is reported to fragment and gradually dissolve only after long time and high temperature solution treatment [58]. In Al-Mg-Si, another Fe-rich phase, namely: π-$Al_6Mg_3FeSi_6$, may be found and, depending on the Mg fraction, may evolve to form the β-Al_5FeSi phase. In particular, when a low content of Mg is present, the transformation is quick, while for higher Mg contents (0.6-0.7 wt%), the process may be inverted, leading to the formation of π-$Al_6Mg_3FeSi_6$ from the β-Al_5FeSi [59-61]. In addition to the above mentioned phases, Q-$Al_5Mg_8Si_6Cu_2$ particles are typically observed in quaternary Al-Si-Mg alloys. Q phase are found to nucleate in the proximity of Al_2Cu particles during the last stages of solidification [62]. Also in this case, Q phase sizing appear to be strictly dependent of the Mg content. The dissolution of this phase is reported to be influenced from both solutionizing parameters and Mg/Cu ratio. An interesting study proposed by Zheng et al. [63] reported that the high Cu/Mg ratio promotes the formation of θ-phase and Q-phase, while under the same Cu/ Mg ratio, the increase of Cu and Mg simultaneously increases both of θ -phase and Q-phase. Evidence of Cu- rich phases in the as-cast case are reported in Figure 6. Figure 7 presents the backscattered EPMA images of the aged alloys. As compared with the as-cast state (Figure 6), the secondary phases appeared partly dissolved into the a-Al matrix after solid solution treatment. Although all the alloys were heat treated at the same regimes, the dissolution of secondary phases is related to the Cu/Mg ratio and the Cu content in the alloy. It can be seen from Figure 6, that several bright intermetallic compounds still exist in the alloys, whereas the low Cu/Mg ratio (Figure 6.b) and the high Cu content (Figure 6.d) show high level of surplus primary intermetallic compounds. At high solutionizing temperature (i.e. 530°C), Q phases were observed to dissolve [64,65], where at lower temperatures (i.e. 430°C), in high Cu alloys (~4wt%) were not observed to dissolve, independently from the Cu content [46,55]. Conversely, when lower Cu content (~1.4wt%) and high Mg (1.3wt%) are present, transformation of the binary Mg_2Si into the quaternary Q is observed, with a general increase of the total Q fraction [64]. Farkoosh et al. [34] reported the dissolution of Q phases after double step solution (500°C + 530 °C) in an Al-Si7-Cu0.5-Mg alloy. In addition, the authors detected dissolution of π-$Al_6Mg_3FeSi_6$ phase for low Mg (0.3wt%) and small amounts of undissolved particles for higher Mg content (0.7wt%). Q phases were observed to dissolve at 495 °C for fine microstructure (~9 μm), in an Al-Si alloy containing 3wt% of Cu, where no variation in

the area fraction was shown in coarser microstructures (~28 and 49 μm) [66], indicating that also microstructural coarseness plays an important role on particles dissolution.

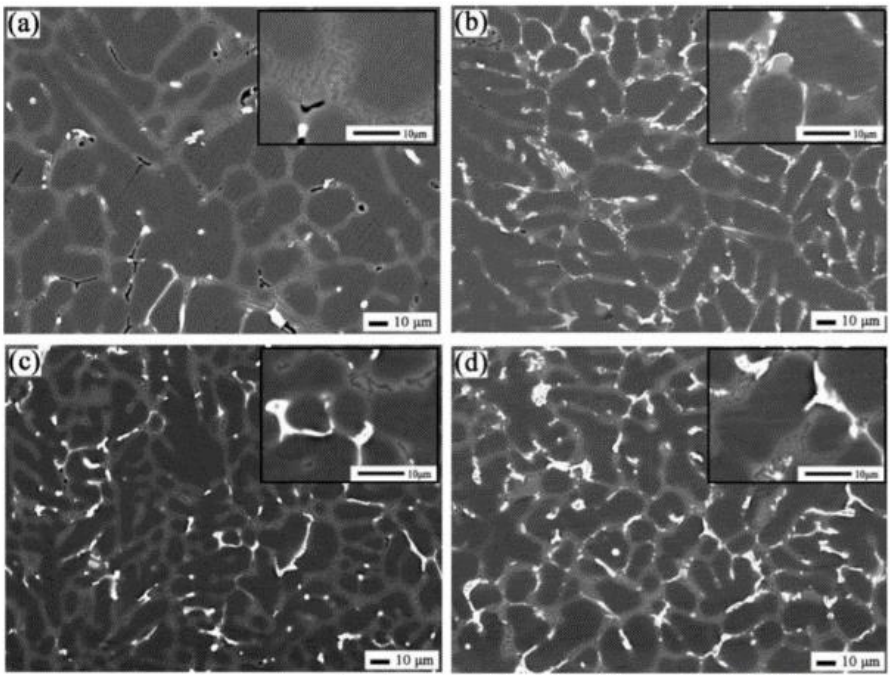

Figure 6 - *Back-scattered EMPA images of as cast alloy with varying Cu/Mg ratio (a) =2, (b)= 1, (c)=4, (d) =4 [63]*

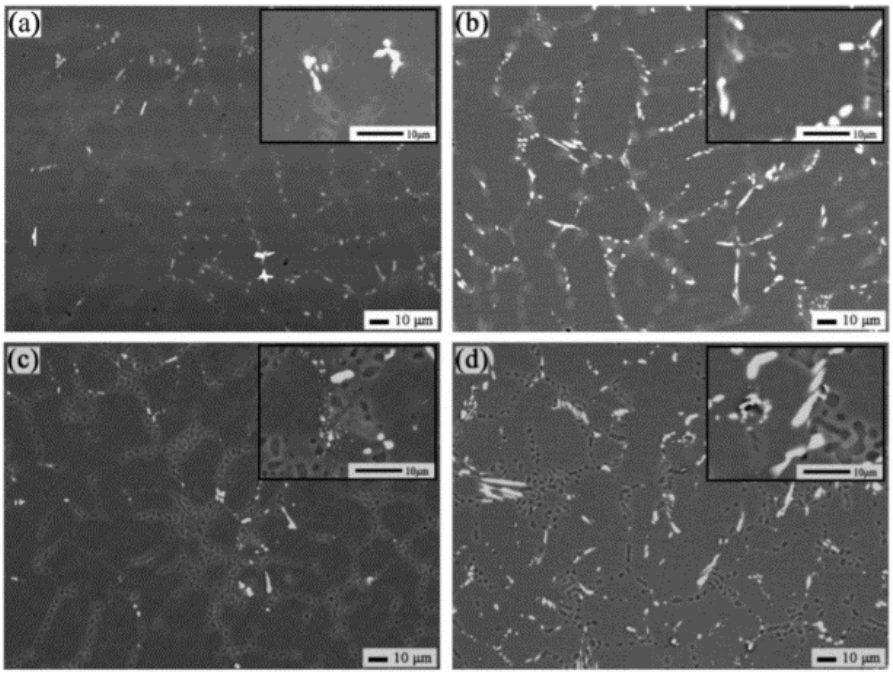

Figure 7 - *Back-scattered EMPA images of heat treated alloy with varying Cu/Mg ratio (a) =2, (b)= 1, (c)=4, (d) =4 [63]*

1.4.2. Aging Treatment in Al-Si-Mg and Al-Si-Cu-Mg alloys

It is of knowledge that age-hardening is one of the most important methods for strengthening aluminum alloys, which results in the breakdown of the supersaturated matrix to nanosized particles capable of being sheared by dislocations [67,68]. By controlling the aging time and temperature, a large variety of mechanical properties may be obtained; tensile strengths can be increased, residual stresses can be reduced, and the microstructure can be stabilized. The precipitation process can occur at room temperature or may be accelerated by artificial aging at temperatures ranging from 90 to 250 °C. After solution treatment and quenching the matrix has a high supersaturation of solute atoms and vacancies. Clusters of atoms form rapidly from the supersaturated matrix and evolve into Guinier-Preston (GP) zones. Metastable coherent or semicoherent precipitates form either from the GP zones or from the supersaturated matrix when the GP zones have dissolved. The precipitates grow by diffusion of atoms from the supersaturated solid solution to the precipitates [67]. Al-Si-Mg-Cu, if properly heat-treated, are characterized by superior mechanical properties in comparison to the more traditional ternary alloys, i.e. Al-Si-Mg and Al-Si-Cu. Type, morphology and size of precipitates strongly depend on the alloy chemical composition and thermal treatment. The typical precipitation sequences which characterize Al-Si-Mg and Al-Si-Cu alloys, respectively, are the following [37-42]:

$$\alpha(SSS) \rightarrow GP\,zones \rightarrow \beta'' \rightarrow \beta' \rightarrow \beta$$

$$\alpha(SSS) \rightarrow GP\,zones \rightarrow \theta'' \rightarrow \theta' \rightarrow \theta$$

where, β”, β’, B’ and θ”, θ’ are the intermediate precipitates, while β and θ the stable incoherent phases.

Al-Si-Mg precipitation sequence usually starts with the formation of spherical GP zones, consisting in local enrichment of Si and Mg atoms; such clusters become, with further aging, acicular and coherent with the Al matrix (β’’- Mg_2Si phase). Precipitates grow, becoming at first semi-coherent (β’) then stable incoherent particles [69]. The time necessary to peak aging usually decreases with increasing aging temperature, unless too high temperatures (>210 °C) are used, leading to the formation of uncoherent precipitates inducing strength decrease. Composition of metastable precipitates was reported to vary, depending on the content of excess Si after quenching and during aging process itself [70]. Strength of the alloy generally increases for increase of Mg content up to 0.5 wt.% [71].

As regarding Al-Si-Cu alloys, GP zones are characterized by agglomeration of Cu atoms. They are generated at room temperature on the dislocations formed during quenching, as a result of the differences in the thermal expansion coefficients of the Al matrix and eutectic Si. At high temperature, at first GP zones dissolve, leading to a strength decrease; subsequently, they are replaced by coherent θ" phases (also named GP2 zones), which transform in the metastable θ' (semi-coherent) and then in the θ incoherent stable phase. Different kinds of precipitates were observed by some authors on dislocations and Al-matrix. Coarse semi-coherent θ' particles and coherent, fine and evenly distributed θ'' phases were observed in correspondence of high density dislocation regions and dislocation free areas, respectively [72]. Peak hardness usually decreases with increasing aging temperature and longer times are needed to reach the peak condition in comparison to Al- Si-Mg and Al-Si-Cu-Mg alloys [72]. On the account of the concomitant presence of Cu and Mg, the strength improvement which can be reached in quaternary Al-Si-Cu-Mg alloys is far superior in comparison to that of ternary alloys. Even if some author reported no variation in time to peak hardness between Al-Si- Mg and Al-Si-Cu-Mg alloys, inferring no variation in precipitates type [73], it is currently accepted that different precipitates may co-exist in these alloys [41,43,44,74,75]. The same time to peak was rdetected also by Reif et al. [76] between Al-Si9-Cu3.5 and Al-Si9-Cu3.5-Mg0.5 alloys, showing sensible higher peak hardness values for the quaternary alloy. By the way, most of the works found in literature reported longer times to peak for Al-Si-Cu alloys in comparison to Al-Si-Cu-Mg, due to acceleration and intensification of the precipitation-hardening processes owing to Mg addition. In fact, while θ' phases nucleate preferentially on dislocations located around Si particles, Q' phases have the capability to nucleate in lower surface energy locations, i.e. throughout the α-Al matrix. The more homogeneous distribution of the quaternary phase would lead to lower diffusion distance, therefore requiring shorter time to aging [72,74]. The formation of θ' phase seems therefore to be somehow related to Cu content. In particular, it has been reported [63] that the low Cu content and Cu/Mg ratio tend to form precursor of β' precipitate, while the high Cu/Mg ratio preferably forms precursors of Q and/or θ precipitates, whereas the high content of Cu and Mg is found to form a large number of θ' precipitates and leads to the coarsening of Q' phase (see Figure 8). Despite it is not generally agreed, it should be pointed out that, double aging peak has been sometimes observed in Al-Si-Cu-Mg alloys by Li et al. [77]. Double-peak response was obtained under aging temperatures higher than 175 °C. The first peak showed higher hardness values in comparison to the second one. Such behavior, not observed in ternary Al-Si-Cu and Al-

Si-Mg alloys, was connected to the formation and dissolution of GP zones, and to the consequential formation of metastable phases.

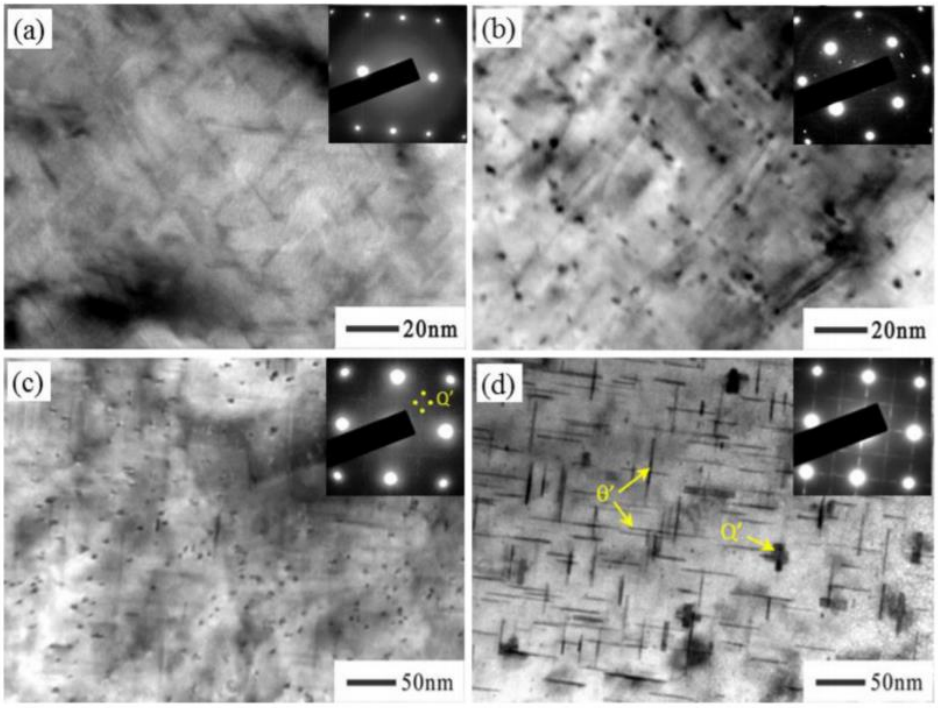

Figure 8 - *Bright-field TEM images of heat treated alloy with varying Cu/Mg ratio (a) =2, (b)= 1, (c)=4, (d) =4 [63].*

1.5. Fracture toughness of aluminum casting

1.5.1 Introduction to fracture toughness

Fracture Toughness of a material can be defined the critical value of the stress intensity factor, where the latter depend on a combination of the stress at the crack tip and the crack size results in a critical value. The local stress σ_{local}, shown in Figure 9, scales as) for a given value of r, where σ is the remotely applied stress, σ_{local} is the stress in the proximity of the crack at a distance r from the tip and c is the crack length; this combination is called the Stress Intensity Factor (K). For the type of load shown (tensile load) K is designated as K_I. Thus,

$$K_I = Y \sigma (\pi c) \quad (1)$$

where Y is a dimensionless constant standing for the crack geometry. K_I has units of MPa $m^{1/2}$. Brittle fracture occurs when K_I reaches a critical value, denoted by K_{IC} . If crack tip incurs to plasticity, instability arises at this critical value, leading to fracture. Besides that, fracture toughness can be explained as the measure the resistance of the material to separate under load when a near-atomistically sharp crack is present. The stress intensity factors are typically classified by the subscript I for "opening mode", II for "shear mode" and III for "tearing mode". The opening mode is the most extensively investigate and hereafter only K_I will be considered. Under load, a metallic material first undergoes elastic deformation and plastically deforms when its yield stress is exceeded. Fracture occurs when the ability to plastically deform under load is exhausted. The leading factor of the plastic deformation is rules by the movement of dislocations and the resistance to its movement causes increased plastic flow stress and facilitates the fracture.

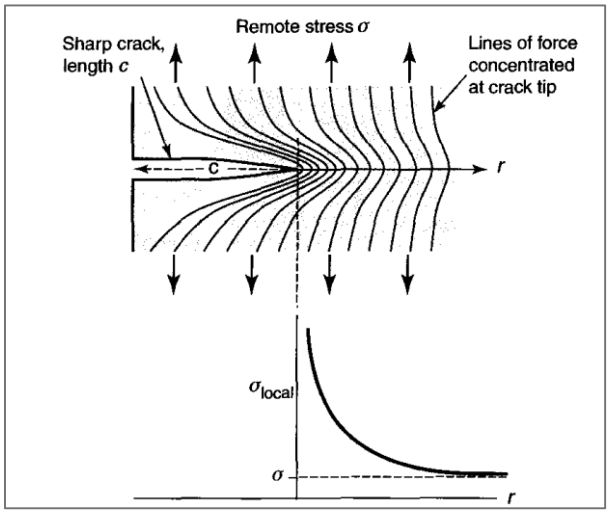

Figure 9 - *Lines of force and local stress variation from a body with sharp crack. Source: M.F. Ashby, et al [78]*

Srinivasan and S. Seetharamu in [79] described both the 'Linear Elastic' and 'Elastic Plastic' Fracture Mechanic approaches, correspondently: LEFM and EPFM. The Linear Elastic fracture mechanics approach is defined as a method of analysis of fracture that can determine the stress required to unstable fracture in a component [80].

The following assumptions are made in applying LEFM to predict failure in components [81]: (i) A sharp crack or flaw of similar nature already exists; the analysis deals with the propagation of the crack from the early stages. (ii) The material is linearly elastic. (iii) The material is isotropic. (iv) The size of the plastic zone near the crack tip is small compared to the dimensions of the crack. (v) The analysis is applicable to near-tip region. Standardized test specimens recommended for LEFM testing are reported in Figure 10. Each specimen has three characteristic dimensions: the crack length (a), the specimen thickness (B) and the specimen width (W). In general, W=2B and a/w = 0.5 with some exceptions. Regarding the test setting, it is customary to introduce a sharp crack at the tip of the machined notch. Introducing a sharp crack through fatigue precracking is the most efficient and the most applied method of introducing a sharp crack. It is worth underline, that care must be taken to respect following two conditions:1) the crack-tip radius at failure must be much larger than the initial radius of the pre- crack and, 2) the plastic zone produced after precracking must be small compared to the plastic zone at fracture. This is particularly necessary for metal castings as many exhibit plasticity; a remarkable exception is flake graphite cast iron castings made in sand molds. In deep details on the LEFM tests are described ASTM E 399 [82].

In specimens showing significant plasticity the crack tip (much less than what is required to cause total plastic collapse) the most appropriate methods to measure the sharp crack growth resistance at the crack tip are the J-integral method and the Crack-tip Opening Displacement (CTOD). The recent tendency however, is to use the J-integral method. Standard ASTM E 1820 [83] reports two alternative methods: the basic procedure and the resistance curve procedure. The basic procedure necessitates of large number of specimens, while the resistance curve test method involves only one specimen and the crack growth is monitored throughout the test. The principal drawback of this method is the additional instrumentation and skill required.

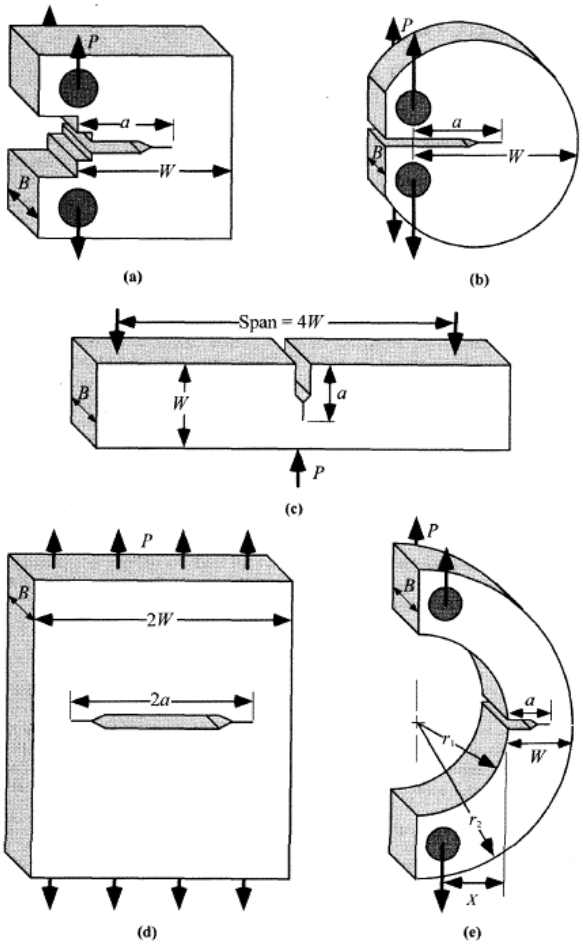

Figure 10 - *Standardized fracture mechanics test specimens: (a) compact tension (CT) specimen, (b) disk-shaped compact tension specimen, (c) single-edge-notched bend (SEB) specimen, (d) middle tension (MT) specimen and (e) arcshaped tension specimen. [84].*

1.5.2 Determining Ductile Fracture Toughness

The J-integral and/or the crack growth resistance (J-R) curve methods for determinate the ductile fracture toughness determination, represent key tool for evaluating a material's structural integrity in the presence of preexisting defects. The J-R curve can assess the work (energy) per unit of fracture surface area needed to drive crack growth. A typical J-R curve is shown in Figure 11. Following the procedure described in ASTM standard E1820-11 [85], the material fracture toughness near the initiation of stable crack growth (Jq) can be obtained. Different types of specimens can be used for the J-R curve test. Figure 12 illustrates three commonly used configurations: A standard compact C(T) specimen,

single edge bend SE(B) specimen, and standard disk-shaped compact DC(T) specimen. After machining, the specimen is subjected to a cycle of fatigue precracking in order to generate the initial sharp crack. Initial crack size is usually controlled to be ~a/W=0.5 where a is the crack size and W is the specimen width. The two servo-hydraulic and electromechanical load frames are commonly used for the J-R curve test. Figure 13 shows the experimental apparatus for performing this test on a C(T) specimen. The J-R curve test apparatus for a C(T) specimen involves a pair of clevises with pins for loading the specimen and a displacement gage for measuring the specimen's crack mouth opening displacement (CMOD). For both C(T) and SE(B) specimen configurations, a load cell measures specimen load.

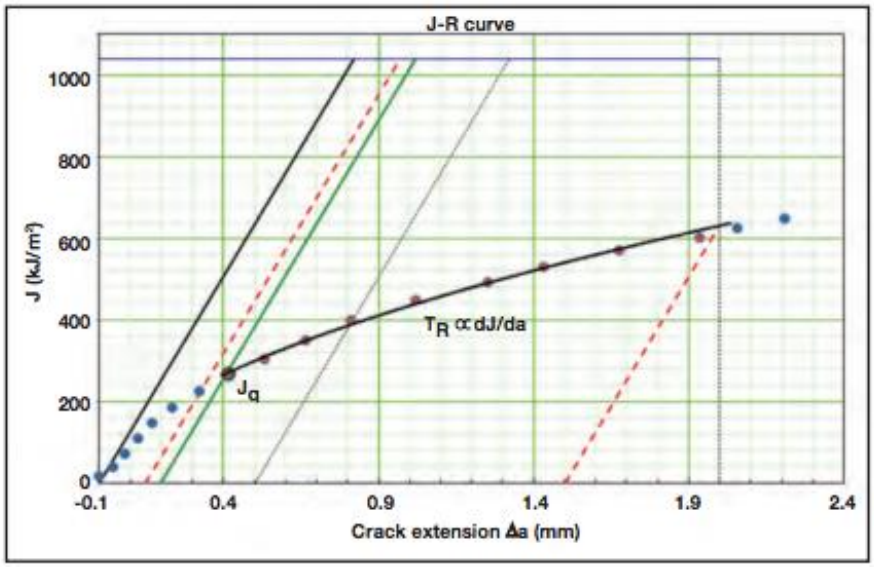

Figure 11- *Typical J-R curve shows the fracture toughness near the initiation of stable crack growth (Jq) [86]*

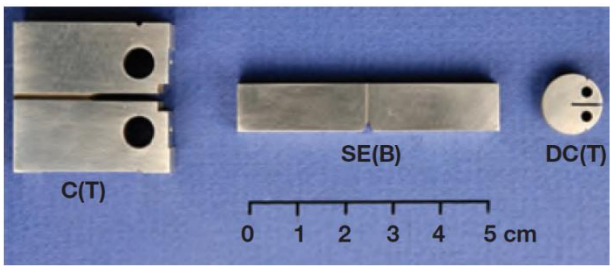

Figure 12 - *Three commonly used specimen configurations for the J-R curve test. Left to right: Standard compact C(T) specimen, single edge bend SE(B) specimen, and standard disk-shaped compact DC(T) specimen. [86]*

Figure 13 - *shows the experimental apparatus for fracture test with a C(T) specimen.*

J-R curve method encompasses two parts: J-Integral and crack growth; aiming to obtain the curve, evaluation of both aspects is required. In elastic unloading compliance, the J-Integral is calculated as:

$$J_{(i)} = J_{el(i)} + J_{pl(i)} \quad (2)$$

where $J_{el(i)}$ and $J_{pl(i)}$ are the elastic and plastic components of J-Integral, respectively.

For $J_{el(i)}$:

$$J_{el(i)} = K_{(i)}^2 (1-\nu^2) / E \quad (3)$$

where ν is Poisson's ratio, E is Young's modulus, and $K_{(i)}$ is the stress intensity factor. $K_{(i)}$ depends on specimen configuration, load level, crack size, and other factors.

he equation for calculating $J_{pl(i)}$ follows:

$$J_{pl(i)} = [J_{pl(i-1)} + (\eta_{pl(i-1)} / b_{(i-1)})*(A_{pl(i)} - A_{pl(i-1)} / B_N)]*[1-\gamma_{pl(i-1)}*(a_{pl(i)} - a_{pl(i-1)} / b_{(i-1)})] \quad (4)$$

where $a_{(i)}$ is the current crack size, $b_{(i)}$ is the unbroken ligament size, B_N is the specimen net thickness, $A_{pl(i)}$ is the plastic area under the load versus load-line displacement record for the specimen, $\eta_{pl(i-1)}$ equals 1.9 for a SE(B) specimen and $(2+0.522b_{(i-1)}/W)$ for a C(T) or

DC(T) specimen, and γ equals 0.9 for a SE(B) specimen and $(1+0.76b_{(i-1)}/W)$ for a C(T) or DC(T) specimen. In order to obtain the real time crack growth value, Elastic unloading compliance measures the material compliance (the ratio of displacement increment to force increment) by periodic unloading and reloading of the specimen. A typical load-displacement record for a J-R curve test using Elastic Unloading Compliance is shown in Figure 14. Each short straight line in Figure 14 represents an unloading-reloading sequence. The rest of the curve resembles a load displacement curve in a tensile test, i.e., initial elastic deformation followed by plastic deformation and load drop after passing the maximum load level. Once the material compliance value is obtained, equations in ASTM standard E1820-11 [85] can be applied to convert the compliance result to the estimated real-time crack size. Finally, the J-Integral curve and crack growth values are integrated and, as results, the J-R curve is obtained.

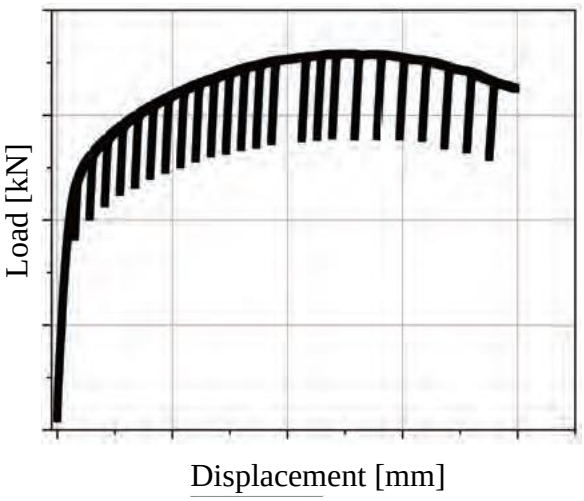

Figure 14 - *Load-displacement record for a J-R curve test with elastic unloading compliance [86]*

1.5.3 Literature overview

So far, the lack of knowledge towards the fracture toughness of these alloys had limited their use to field where fracture toughness related properties were not relevant. Though, fracture toughness evaluation in Al-Si alloys might represent a key step to understand the metallurgical features which control the toughness and hence will might allow proper material specifications to be settled for those applications where toughness-related failure must be prevented. In this concern, previous studies [87] reported the fracture toughness

of a series of Al-Si castings and defined a ratio (λ / DE_{Si}) where λ is the silicon particle spacing and DE_{Si} is the equivalent silicon particle diameter. Tirakiyoglu [88] examined the fracture toughness potential of cast Al-7%Si-Mg alloys as a function of yield strength value. Tohgo and Oka [89] focused on the influence of coarsening treatment of the fracture toughness of Al-Si-Mg alloys. Lee et al. [90] investigated the effect of the Si-particles on the fracture toughness of A356 alloy cast, using different casting technologies. The comprehensive conclusion rising up from these studies is that the resistance to crack growth increases with enhancing the degree of refining of dendrite cells and eutectic silicon, whereas the crack tip plastic is higher in slowly solidified microstructure (sand castings) and lower in permanent mold or, die casting. Hence, the factors favoring the fracture toughness would be decreased dendritic cell size and refinement of Si-eutectic and intermetallic, the opposing factor would be reduced plasticity due to increase in yield strength, both due to primary cell and eutectic refinement. Further, the influence of minor chemical modification has been analyzed by Alexopoupolos [91]. However, as reported by Staley [92] there are several extrinsic factors such as porosity, oxides and inclusions that tend to affect the fracture toughness of these class of alloy.

1.6. Al-Si-Mg alloys in Selective Laser Melting (SLM)

1.6.1. The SLM technology

Additive Manufacturing (AM) is an innovative technology that is currently influencing the trend of the manufacturing industry. So far, both industry and academia have been focusing their attention on AM technology, leading, to date, to outcomes such as: review papers [93-100] and ISO and ASTM standards [101-105]. AM technologies enable layer-by-layer fabrication of complex parts directly from CAD files without part-specific tooling, offering, as compared to the conventional manufactured methods, the advantages of customized geometry without wasting materials or increasing cost. Among all metal AM techniques, selective laser melting (SLM), has experienced a large growth in the past few years due to his high flexibility, versatility and customizability and it is now suiting most sectors of industrial production. In the SLM process, a layer of powder (generally 20–100 μm thick) is spread over the building area, using a powder spreading system. Once the layer of powder is deposited on the building platform, which can be pre-heated, a laser source is directed

onto the powder bed, and selectively fuses the material. After scanning one layer, the platform is lowered by one-layer thickness and another layer of powder is spread on the formerly solidified top surface. This layer-upon-layer deposition process is repeated to build a solid three-dimensional component according to the instructions provided by CAD files. Figure 15 graphically shows the SLM process mechanisms.

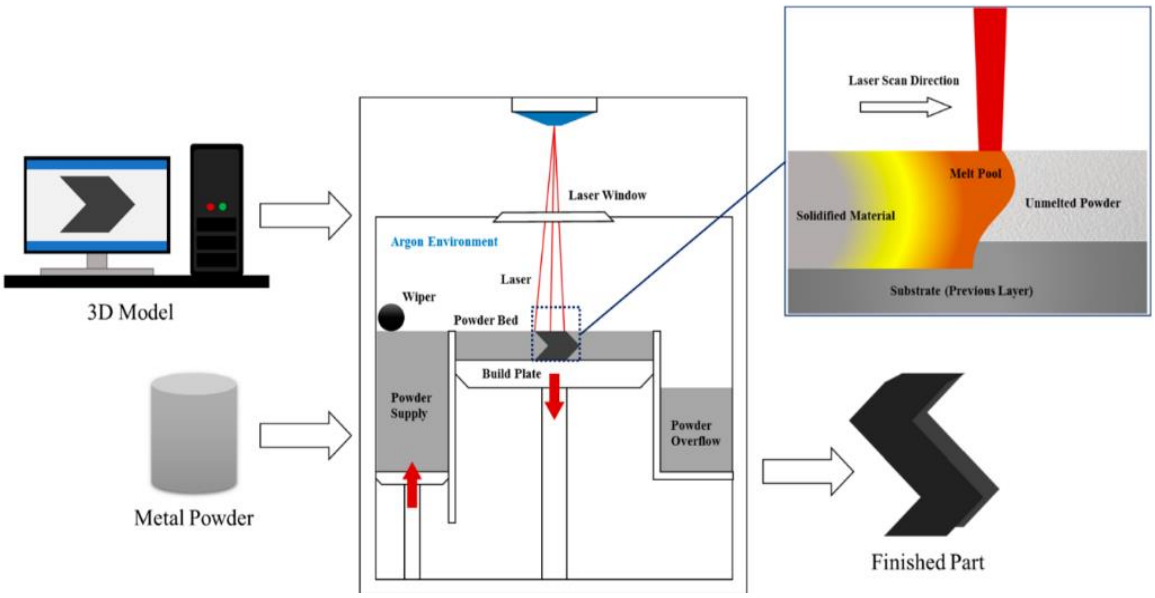

Figure 15 – *Graphic representation of the SLM process mechanism [106].*

Figure 16, show an example a schematic of beam scanning in the powder bed system, whose values are referred to standard conditions for AlSi10Mg/EOS as studied in [107]. It can be seen (Figure 16) that the layer thickness corresponds to the perpendicular movement of the substrate after selectively fusing one powder layer and, hatch spacing is the lateral distance between adjacent laser tracks in the same layer. Rapid movement of the melt pool (melt pools speed ≈ 1 m/s) in the SLM process implies high cooling rates and directional solidification, thus resulting in: non-equilibrium microstructure (metastable phases, non-equilibrium compositions, solute trapping), fine and ultra-fine grains, occasionally anisotropically elongated, and metallurgical defects (porosity due to unmelted powders and/or gas entrapment) [108-109]. In addition, high localized thermal gradients and very short interaction times, which leads to rapid volume changes, causes substantial residual stress development. As a result, the mechanical properties of SLM parts can differ substantially from one another and from those produced by conventional techniques.

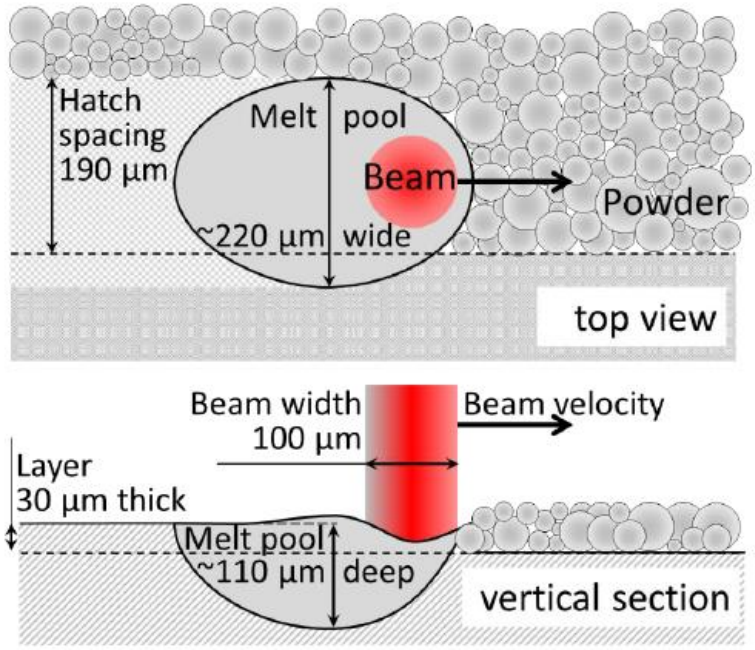

Figure 16 - *Schematic of beam scanning in the powder bed system [107].*

1.6.2. AlSi10Mg in SLM application

As, widely discussed in this thesis, aluminum alloys are known for their good combination of low density, high thermal conductivity, good mechanical properties and fluidity, and are consequently widely employed in automotive and aerospace industries [110].

Thanks to its high fluidity, low shrinkage tendency, good weldability and high corrosion resistance [111,112], the AlSi10Mg is the Al alloy most applied for selective laser melting. With the aim to address the great demand for Al–Si–Mg alloys for many applications, e.g. motor racing, automotive industry, aerospace and heat exchanger products, numerous studies have been performed on these alloys, considering such aspects as the starting powders up to the possible final applications of lightweight lattice structures [113-115]. The two major alloying elements in the alloy are silicon and magnesium. The 10 wt. % Si imparts high fluidity where, the addition of Mg, is meant to induce the formation of Mg2Si for precipitates. Lam et al. [116] described two different microstructures generated in the AlSi10Mg under the SLM technology: (i) a cellular-dendritic structure of α-Al, (ii) a

network of the eutectic Si phase along the boundary adjacent the α-Al phase. The sizes of the Al cellular dendrites, measured by TEM analysis, corresponded to 500-1000 nm, that is, much lower values than the ones of the cast parts. In this concern, a previous study [117] showed how the SLM process kinetically favored the cellular solidification of α-Al and extended solubility of Si into Al. The residual amount of Si was segregated at the cellular boundaries, which had a thickness of about 200 nm. The overall macrostructure of the AlSi10Mg samples obtained by means of SLM, which was constituted by the overlapping of subsequent scan tracks, depended on the scanning strategy and process parameters that were adopted. Figures 17 and 18 illustrates examples of different macrostructures produced by means of different scanning parameters in SLM technology [118,119].

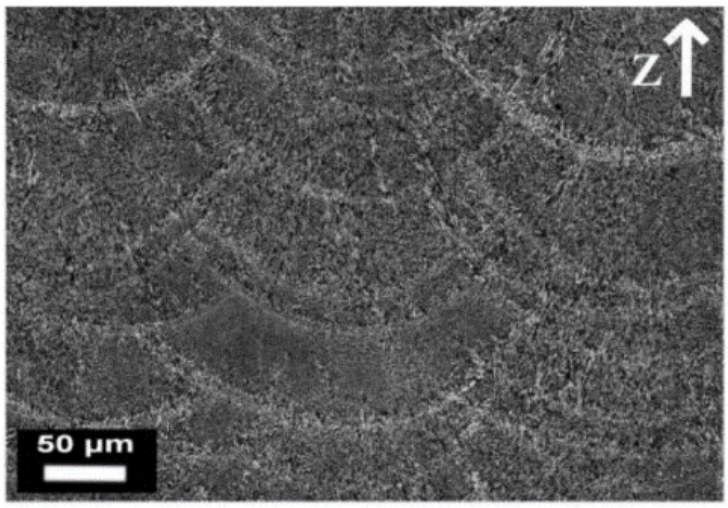

Figure 17 - *Optical micrographs of AlSi10Mg samples produced by means of SLM using a unidirectional scanning strategy (along the x axis) [118].*

Manfredi et al. [118,119] studied the AlSi10Mg microstructure, and described a heat affected zone of between adjacent melt pools. Thijs et al. [114] investigated the effects of different scanning strategies on the of AlSi10Mg parts. It was demonstrated that when the cellular solidification mode was active, the preferential growth direction of the cells was along the ⟨100⟩ crystal direction, going towards the centreline of the melt pool.

The obtained face centered cubic aluminum cells appeared decorated with a diamond-like silicon phase. This fine distribution leads to a high hardness of the SLM parts, of about 127 Hv0.5. Moreover, the fineness of the cells is seen to change from below 0.7 µm, at the melt pool border, to 0.4 µm in the middle of the scan track. Furthermore, on the basis of this study, it could be stated that a more anisotropic or isotropic part can be obtained according to which scanning strategy is applied.

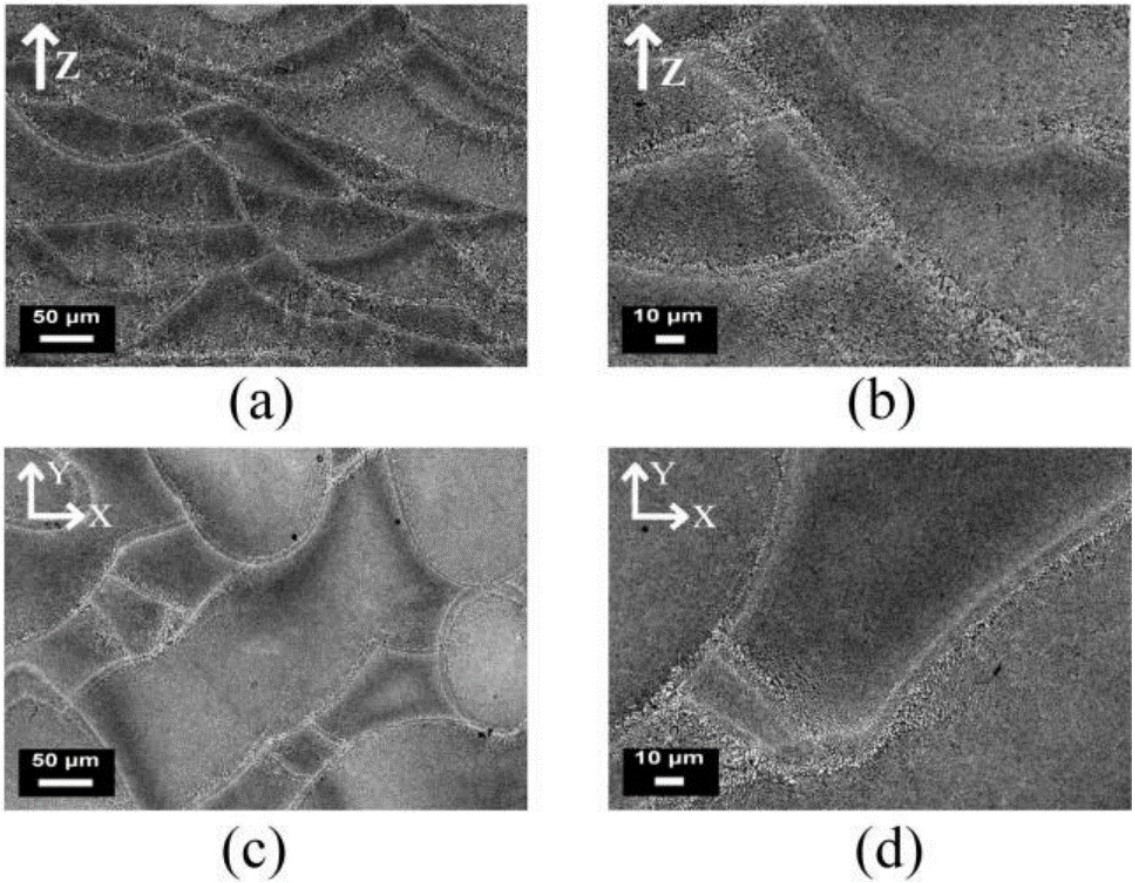

Figure 18 - *Optical micrographs of AlSi10Mg samples obtained by means of SLM, built using a rotated scanning strategy (67° of rotation between subsequent layers), at different magnifications: (a,b) describe a vertical section of the part along the building direction (z axis); while (c,d) show the section parallel to the building plane (xy-plane) [119].*

Several papers have reported the applications of various heat treatments for additive manufactured AlSi10Mg parts, in order to modify solidification microstructure and enhance mechanical properties [120-123]. Li et al. [120] investigated the effect of the

solution and artificial aging heat temperatures on the morphology and fraction of phases, solid solution and tensile properties. They measured the peak shift in XRD spectra to quantify the concentration of Si in solution and found that 8.9 at% of Si was dissolved in Al matrix in the as-built condition, decreased rapidly during heat treatment at 500°C, and further reduced after artificial aging at 180°C. Si phase was originally in a fibrous network form in as-built parts and precipitated out of solution and spheroidized into particles during heat treatment. Brandl et al. [121] studied the effect of T6 heat treatment (heat treatment with artificial aging) on the fatigue resistance of printed AlSi10Mg parts, and they found that this heat treatment could significantly improve the fatigue life by at least an order of magnitude as compared to the as-built components. The enhancement of the fatigue life by the heat treatment could be attributed to the higher strength [115]. Fiocchi et al. [122] investigated the effect of annealing temperatures (263°C, 294°C, 320°C) on microstructure evolution of AlSi10Mg alloy and applied DSC (differential scanning calorimetry) to distinguish two exothermic phenomena during heating: Mg2Si precipitation at 226°C and Si precipitation at 295°C.

1.6.3. Mechanical behavior of AlSi10Mg/SLM

As far as the mechanical behavior of SLM parts is concerned, it is possible to affirm that SLM parts have a higher tensile strength and, at the same time, a comparable ductility and a lower fatigue life than parts produced by means of traditional manufacturing techniques. The reason why AlSi10Mg parts produced by SLM present higher hardness, and tensile strength than traditionally cast ones can be mainly imputable to these three factors [116]: (i) the ultrafine-grained microstructure, contributing to the grain boundary strengthening, (ii) the alloying elements, enabling the solid solution strengthening, and (iii) the strengthening promoted by the interactions of dislocations. Buchbinder et al. [115] tested AlSi10Mg alloy samples produced by means of SLM using two different building parameter sets: 240 W laser power and a 500 mm/s scanning distance for the first one, 960 W laser power and a 1000 mm/s speed for the other. The ultimate tensile and yield strengths appeared to be independent of the laser power, and comparable values were obtained in both cases (UTS = 400–450 MPa; YS = 210–240 MPa). The elongation at break of samples produced with high laser power was 25% higher than low power case. Additionally, with reference to the elongation, attention was paid to the three main aspects which appeared to

govern the anisotropy in an SLM process: defects and pore presence, grain orientation and texture, interfaces between melt tracks and layers. Contrasting results were reported by Rosenthal et al. [124], who showed higher elongation at break for specimens built horizontally than those built vertically. To support these assumptions fracture surfaces were analyzed showing that vertically built specimens exhibited a predominantly ductile failure located between weakly bonded layers, while fracturing occurred within each layer in the horizontally built ones. Kempen et al. [114] obtained similar results, and obtained a mean elongation at break of 5.55% for horizontal samples and 3.47% for vertical ones. Large pores, which were responsible for fracture initiation during the tensile test, became the preferential sites for inhomogeneous deformation at a high stress level (around 395 MPa), and consequently for cracking initiation. These defects were found to be more numerous in vertical samples than in horizontal ones. Read et al. [125], analyzing fracture surfaces, found the presence of thick oxide layers on the particles: these un-bonded regions gave rise to large cracks during failure. These un-bonded areas appeared flat or faceted, in comparison to the fracture regions where ductile deformation occurred [126]. There has been limited work exploring the dynamic response of AlSi10Mg SLM parts. [121,127-129]. Brandl et al. [121] reported that platform temperature, build direction and heat treatment (peak-hardening) all affected the fatigue life of AlSi10Mg parts produced by SLM, with heat treatment having the largest effect (by improving the strength [115]). Maskery et al. [129] also found that heat treatment (heat treatment for 1 hour at 520°C, followed by artificial aging for 6 hours at 160°C) significantly improved the ductility and fatigue performance of AlSi10Mg parts built by SLM (without subsequent machining), although heat treatment caused some loss of strength. Siddique et al. [130] reported that increasing the base temperature (to 200°C) during selective laser melting (of a slightly different alloy, AlSi12) decreased residual stress, eliminated large pores and decreased scatter in fatigue results, but causing lower static strength and lower average fatigue strength.

2. Summary and Conclusions from the Articles

The use of Al-Si alloys in various applications such as automotive and aerospace has recently increased in the light of their good castability, lightness, low strength-to-weight ratio and corrosion resistance. Among this class, Al-Si-Mg foundry alloys are found to give good results since they show concurrently excellent casting characteristics and mechanical properties. In view of the two room and high temperature applications, enhanced static and dynamic properties are required and, indeed, coarsening resistant strengthening phases are needed. To pursue this goal, two main paths can be followed, namely: (i) chemical modification of Al-Si-Mg alloys; (ii) Heat Treatment Optimization. Both the paths are meant to induce the formation of thermally stable strengthening phases. In this perspective, *article 1* offers a comparative study on the high-temperature tensile properties of an unmodified A356 alloy with and without the addition of Ni or V in traces (600 and 1000 ppm of Ni and V, respectively). Samples obtained from sand and permanent mold castings, were investigated in the as-cast and T6 heat-treated conditions. Tensile tests and fracture surfaces showed that neither Ni nor V addition had a detrimental effect on high-temperature tensile properties. Aging curves showed a strong loss of hardness affecting the T6 class between 30-min and 1-h exposure time. After 6-h aging, no evidence of aging treatment persisted on hardness of the tested material, might being a serious issue for industrial engine applications, where temperatures commonly exceed 200 °C. Moreover, the hardness values did not reveal any significant difference between the reference alloy and the Ni- and V-containing alloys in both casting conditions, in complete analogy with the tensile properties. Unmodified eutectic silicon particles provided inhomogeneity in the a-Al matrix and acted as the principal source of stress concentration leading to fracture. Besides Ni and V modification, the addition of Cu as a way to enhance the high temperature mechanical response is widely considered in the foundry sector. In this light, *article 2* evaluate the influence of Cu on A356 as cast alloy. Stress-Strain curves clearly showed improvement in strength with increasing Cu content, for the three B (bottom), C (center), and T (top) specimens, without significant reduction of elongation. In parallel, tensile curves also revealed how the specimen cutting position influences the mechanical properties leading to an enhancement in strength by approximately 10% and 20% for the Cu-free and the Cu-containing alloys, respectively, moving from the Top to the Bottom.

B, C and T`s SDAS values for the three Cu0 (Reference), Cu0.5 and Cu1 alloy variants range between 30, 35 and 40 µm, respectively. The 10 µm shift, albeit its impressive effect on a small scale (12 mm), seems not to be the sole cause behind the tensile behavior.

Cu content exerted a prominent influence in increasing the hardness response of this alloy. eutectic phases, indicated as Al-Q-θ, are found along the interdendritic regions. The bottom samples, richer in Si particles and Si-/Mg-/Cu-bearing compounds, offer the highest tensile strength and the lowest hardness. In line with these findings, electrical conductivity (EC) values decrease moving from the bottom to top position, indicating a higher content of solute atoms in the α-matrix of the top samples as compared to the α-matrix of the bottom samples. When it comes to the Heat Treatment Optimization (ii), a growing interest toward the addition of Cu rise up. In light of this, the influence of the aging parameters on the tensile response has been widely investigated on high Cu alloys (up to 5 wt. %), while few works were conducted on Al-Si-Cu-Mg alloys containing up to 1 wt. % Cu. In *article 3*, two solutionizing temperatures (500 °C and 530 °C) and two aging temperatures (155 °C and 190 °C) were tested in Al-Si-Mg alloys having 0 wt.%, 0.5 wt.%, and 1 wt.% Cu content. Aiming to achieve maximum dissolution of the strengthening elements in the Al matrix and to avoid incipient melting of Cu-rich phases, the temperature of 530 °C and an exposure of 5 h have been selected as the optimized solutionizing parameters. Double aging peaks have been observed in the Cu-containing alloys, while the Cu-free alloy has an increasing hardness tendency with aging time. Under aged (4 h at 155 °C and 2 h at 190 °C) and peak aged (10 h at 155 °C and 4 h at 190 °C) have been chosen for the tensile testing. Adding 0.5 wt.% and 1 wt.% of Cu did not turned into a proportional strength of the tensile response, as the improvement is strength in the Cu1 variant appeared much more pronounced compared to the Cu0.5 case. Optimizing the SHT resulted in higher strength and elongation as compared to the commercial A356 Aluminum foundry alloys. When comparing the precipitation in the three alloys, it becomes clear that the needle-lengths decrease significantly with increasing Cu addition. Refining the precipitates, result in increase in UTS and HV for higher Cu-additions, due to a higher dislocation density and impediment potential.

With improving molten metal quality and foundry technology, cast alloys are expected to be used more commonly in critical applications. The demands for improved damage tolerance of cast aluminium alloys have increased the importance of fracture-related properties. In this view, *article 4* proposes a study on the fracture toughness of a A356 Al alloy and its Cu-containing (1wt.%) variant, under four different aging conditions. In order

to assess the mutual influence of casting defects and alloys hardness, as resulting after aging treatments, hardness results have been composed together with porosity values, and finally integrated with the JIC values. Results indicates that the early stage of the fracture test, when a small load is applied, microcracks are initiated at the eutectic Si particles in interdendritic regions. Besides the fact that porosity appeared to be the foremost fracture leading parameter, there is evidence of eutectic microstructure contribution toward the fracture toughness. J-R curves evidenced higher trends for the Cu-containing alloys as compared to the A356 reference alloys. Where the crack initiation is mainly ruled by the mutual cooperation between casting defects and alloy (eutectic network + α-Al matrix) hardness response, the crack propagation appears to be controlled by the content of hardening precipitates, enriching the α-matrix.

Good castability of Al-Si alloys, characterized by high melt fluidity, narrow solidification range associated with eutectic, and low shrinkage with low hot tearing tendency, makes Al-Si alloys readily available for the emerging additive manufacturing (AM) technology. Among the AM technologies, the Selective Laser Melting (SLM), has been experiencing a large growth since the past few years due to his high flexibility, versatility and customizability and it is now suiting most sectors of industrial production. The SLM technology involves layer by layer melting of the metallic powder by means of a high-power laser beam according to the instructions provided by CAD files. The process is characterized by high temperature gradients leading to rapidly solidified, non- equilibrium microstructures, causing a substantial residual stress development. As a consequence, the mechanical properties of SLM parts can differ substantially from one another and from those produced by conventional techniques. In order to meet the full potential that the SLM has to offer, especially for flight-critical components, *article 5* examines the high cycle fatigue crack growth behavior in the linear region of da/dN vs. ΔK diagrams (described by the Paris law) of AlSi10Mg alloy for different experimental conditions. The Fatigue Crack Growth (FCG) curves revealed the beneficial influence of the heat treatment on the FCG response, as compared to the as-built case. On the other hand, the latter' fatigue crack growth behavior was found to be strongly dependent on the material orientation. The fracture mode was found to be responsible for the observed direction-dependence on the FCG response. Specifically, the heat-affected zones (HAZs) around interlayer boundaries are the weakest link in the material, because Si particles finely distributed around the α-Al

grains along the boundaries between adjacent melt pools are the dominant contributor to fracture initiation and propagation.

Cracks propagating along planes oriented perpendicular to the layers therefore encounter more resistance than they do when propagating parallel to the layers, as in the latter case they can easily move along the weak HAZs. Cracks propagating transversally along the entire thickness of the as-built sample exhibit the lowest fatigue crack growth rates as they are constantly forced to open up bottom layers subjected to compressive residual stresses. After a T6-heat treatment, homogenization of the microstructure and of residual stresses minimizes the dependence of crack growth rate on crack orientation. Restructuring of the Si precipitates into large, rounded particles, farther away from one another than are the fine Si precipitates in as-built condition, enhances the fatigue resistance as the crack is forced to propagate across tough, pure α-Al regions.

3. References

1. V.S. Zolotorevskiĭ, N.A. Belov, and M.V. Glazoff, *Casting aluminum alloys*. Elsevier Science Ltd (2007).
2. J.L. Murray and A.J. McAlister: *Bull. Alloy Phase Diagr.*, 1984, vol. 5, pp. 74-84.
3. J. G. Kaufman and E. L. Rooy, *Aluminum Alloy Castings: Properties, Processes and Applications.* ASM International (2004).
4. J. Grandfield and J. Taylor, *Material Science Forum*, vol. 630, 2009, pp. 129-136.
5. G. Jha, F. Cannova, and B. Sadler, *Light Metals*, TMS, 2012, pp. 1303-1306.
6. C. Coney, L. Crabtree, J. Gavin, W. Marcrum, A.Weber, L. Edwards Sadler B.A. (eds) Light Metals (2013).
7. J.Grandfield, L.Sweet, C.Davidson, J.Mitchell, A.Beer, S.Zhu, X.Chen, and M. Easton., *Light Metal*, 2013, pp. 39-45.
8. S. Zhu, J.Y.Yao, L. S wee, M .Easton, J.Taylor, P. Robiso, and N.Parson, *JOM*, vol.65, 2013, pp. 584-592.
9. J.A. Garci, C. Hinojosa, R. Gonzalez, C.M. Gonzalez and Y. Houbaert, *J. Mater. Process. Tech.*, vol. 143-144, 2003, pp. 306-310.
10. T.H. Ludwig, P.L.Schaffer, L.Arnberg, *Metall. Mater. Trans. A*, vol. 44 A, 2013, pp.3783-3796.
11. F.Stadler, H.Antrekowitsch, W. Fragner, H. Kaufmann, and P.J. Uggowitzer: *Mater. Sci. Forum*, vol.690, 2011, pp. 27-277.
12. D. Casari, T.H. Ludwig, L. Arnberg, M. Merlin, and G.L.Garagnani: *Mater. Sci. Eng. A*, vol. 610, 2014, pp. 414-26.
13. I.J.Polmear.Light Alloys: From Traditional Alloys to Nanocrystals Butterworth-Heinemann, 2005, pp 30-31.
14. U. Mannweiler, W. Schmidt-Hatting, D. Rodriguez, and A. Maitland, *Light Metals*,1989, pp 449-454.
15. L.F. Mondolfo, *Aluminum Alloys: structure and properties*. 1976, London: Butterworth.
16. T.H. Ludwig, P. Schaffer, L. Arnberg. TMS Light Metals 2013.
17. M.Merlin, G.L.Garaganani, *Metallurgical Science and Technology* , Vol. 27-1, 2009.
18. Couture, A.in AFS Int. Cast Met.J., 6, 1981, pp. 9-17.

19. C.H. Càseres, C.J. Davidson, J.R. Griffiths, and Q.C.Wang., *Metall. Mater. Trans. A*, 30A, 1999, pp. 2611-2618.
20. L.Arnberg L.Bäckerud, G.Chai, Solidification Characteristics of Aluminum Alloys.Vol III. Dendrite Coherency, Illinois, AFS.
21. S. Nafisi, R. Ghomashchi, *Materials Science and Engineering A*, vol. 415, 2006, pp. 273-28.
22. G. A. Edwards, K. Stiller, G. L. Dunlop, and M. J. Cooper, *Acta Mater*., vol. 46, 1998, pp. 3893–3904.
23. K. Matsuda, H. Gamada, K. Fujii, Y. Uetani, T. Sato, A. Kamio, and S. Ikeno, *Metall. Mater. Trans. A*, vol. 29, 1998, pp. 1161–1168.
24. D. W. Pashley, J. W. Rhodes, and A. Sendorek, *J. Inst. Metals*, vol. 94, 1966, pp. 41–49.
25. M. H. Jacobs, *Phil. Mag.*, vol. 26, 1972, pp. 1–13.
26. I. Dutta and S. M. Allen, J. *Mater. Sci. Let*., vol. 10, 1991, pp. 323–326.
27. J. Andersen, H. W. Zandbergen, J. Jansen, C. Træholt, U. Tundal, O. Reiso, *Acta Mater*., vol. 46, 1998, pp. 3283–3298.
28. G. E. Totten and D. S. MacKenzie, Handbook of Aluminum - Vol.1 Physical Metallurgy and Processes. Marcel Dekker (2003).
29. A.M.A. Mohamed, and F.H. Samuel, Intech, (2012).
30. M. Yıldırım, D. Ozyürek, *Mater. Des.*, vol. 51, 2013, p.p. 767-774.
31. H.W. Zandbergen, S.J. Andersen, J. Jansen, *Science*, vol. 277, 1997, pp. 5.
32. I.M. Lifshitz, V. V Slyozov, *J. Phys. Chem. Solids*, vol. 35, 1961, pp. 35.
33. C. Wagner, *Electrochemie*, vol. 65, 1961, pp. 581
34. A.R. Farkoosh, M. Pekguleryuz, *Mater. Sci. Eng. A*, vol. 621, 2015, pp. 277.
35. A.R. Farkoosh, M. Javidani, M. Hoseini, D. Larouche, M. Pekguleryuz, *J. Alloys Compd*., vol. 551, 2013, pp. 596.
36. A. Farkoosh, X. Chen, M. Pekguleryuz, in *Mater. Sci. Technol*. Conf. Exhib., Montreal, Canada, 2013, pp. 1220-1227.
37. J. Man, L. Jing, S. G. Jie, *J. Alloys Compd*., vol. 437, 2007, pp. 146.
38. M. Murayama, K. Hono, M. Saga, M. Kikuchi, Mater. Sci. Eng. A 1998, 250, pp. 127.
39. L. Zhen, W. Fei, S. Kang, H. King, *J. Mater. Sci*., vol. 32, 1997, pp.1895
40. W. F. Miao, D. E. Laughlin, *Scr. Mater*., vol. 40,1999, pp. 873.
41. D. G. Eskin, J. Mater. Sci. 2003, 38, 279.

42. S. K. Son, M. Takeda, M. Mitome, Y. Bando, T. Endo, *Mater. Lett*., vol. 59, 2005, pp. 629.
43. S. C. Wang, M. J. Starink, N. Gao, *Scr. Mater*., vol. 54, 2006, pp. 287.
44. P. Ratchev, B. Verlinden, P. De Smet, P. Van Houtte, *Scr. Mater*., vol. 38, 1998, pp. 1195.
45. I. Aguilera-Luna, M.J. Castro-Roman, J.C. Escobedo-Bocardo, F.A. García-Pastor, M. Herrera-Trejo, *Mater. Charact.*, vol. 95, 2014, pp. 211-218.
46. Y. Han, A.M. Samuel, H.W. Doty, S. Valtierra, F.H. Samuel, *Mater. Des*., vol. 58, 2014, pp. 426-438.
47. G.Q. Wang, Q.Z. Sun, L.M. Feng, L. Hui, C.N. Jing, *Mater. Des*., vol. 28, 2007, pp. 1001-1005.
48. A. Biswas, D. J. Siegel, D. N. Seidman, *Acta Mater*., vol. 75, 2014, pp. 322.
49. K. Matsuda, D. Teguri, Y. Uetani, T. Sato, S. Ikeno, *Scr. Mater*., vol. 42, 2002, pp. 833.
50. E. Sjölander, *J. Mater. Process. Technol*., vol. 210, 2011, pp. 1249.
51. Z. Li, A. Samuel, F. Samuel, C. Ravindran, S. Valtierra, *J. Mater. Sci*., vol.38, 2003, pp. 1203.
52. E. Samuel, A. Samuel, H. Doty, *AFS Trans.*, 1996, pp. 893-901.
53. Li, A.M. Samuel, F.H. Samuel, C. Ravindran, S. Valtierra and H.W. Doty, *AFS Transactions*, vol. III, 2003 pp. 3-100.
54. Y. M. Han, A. M. Samuel, F. H. Samuel, S. Valtierra and H. W. Doty, *AFS Trans*, vol. 116, 2008, pp. 79-90.
55. P. Rometsch, L. Arnberg, D. Zhang, *Int. J. Cast Met. Res*., vol.12 1999, pp. 1.
56. D. Zhang, L. Zheng, D. St. John, *J. Light Met*., vol.2, 2002, pp. 27.
57. S. Shivkumar, J. S. Ricci, C. Keller, D. Apelian, *J. Heat Treat*., Vol.8, 1990, pp. 63.
58. N. Crowell, S. Shivkumar, *AFS Trans*., vol. 107, 1995, pp. 721.
59. A. Dons, L. Pedersen, S. Brusethaug, *Aluminium*, vol. 76, 2000, pp. 294.
60. J. Taylor, D. St. John, J. Barresi, M. Couper, *Mater. Sci. Forum.*, vol.331, 2000, pp. 277.
61. P. Rometsch, G. Schaffer, J. Taylor, *Int. J. Cast Met. Res*., vol. 14, 2001, pp. 59.
62. A. Samuel, P. Ouellet, F. Samuel, H. Doty, *AFS Trans*., vol. 105, 1997, pp. 951.
63. Y. Zheng, W. Xiao, S. Ge, W. Zhao, S. Hanada, C. Ma, *J. Alloys Compd.*, vol. 649, 2015, pp. 291-296.
64. L. Lasa, J. Rodrigues-Ibabe, *J. Mater. Sci*., vol. 39, 2004, pp. 1343.

65. S. Chaudhury, D. Apelian, *Met. Mater. Trans*. *A*, vol. 37, 2006, pp. 2295.
66. E. Sjölander, S. Seifeddine, *Metall. Mater. Trans. A*, vol. 45(4), 2013, pp. 1916-1927.
67. ASM metals handbook, Vol 15, Ch. 1, 2008
68. J. Gauthier, P.R. Louchez and F. H. Samuel, Cast Metals, vol. 8, 1995, pp. 91-106.
69. D. Shivkumar, S., Keller, C., Apelian, *AFS Trans.*, vol. 98, 1990, pp. 905.
70. N. Maruyama, R. Uemori, N. Hashimoto, M. Saga, M. Kikuchi, *Scr. Mater*., vol. 36, 1997, pp. 89.
71. J. A. Taylor, D. H. St John, J. Barresi, M. J. Couper, *Int. J. Cast Met. Res.,* vol.12. 2000, pp. 419.
72. H. G. Kang, M. Kida, H. Miyahara, K. Ogi, *AFS Trans*., vol. 27, 1999, pp. 507.
73. Y. J. Li, S. Brusethaug, A. Olsen, *Scr. Mater*., vol. 54, 2006, pp. 99.
74. D. Chakrabarti, D. E. Laughlin, *Prog. Mater. Sci*., vol. 49, 2004, pp. 389.
75. B. Cayron, P. a. Buffat, *Acta Mater*., vol. 48, 2000, pp. 2639.
76. W. Reif, J. Dutkievicz, R. Ciach, S. Yu, J. Krol, *Mater. Sci. Eng. A*, vol. 165, pp. 234-236.
77. R. Li, R. Li, Y. Zhao, L. He, C. Li, H. Guan, Z. Hu, *Mater. Lett*., vol. 58, 2004, pp. 2096.
78. Ashby, M. F., Shercliff, H., & Cebon, D. *Mat. Eng. Sci. Proc. Des*., vol. 167, 2007.
79. M. Srinivasan, S. Seetharamu, *Science and Technology of Casting Processes-INTECH*, Chapt. 10, 2012, pp. 285-312.
80. http://www.termwiki.com/EN:linear_elastic_fracture_mechanics., 2012.
81. http://www.public.iastate.edu/~gkstarns/ME417/LEFM, 2012.
82. E399-97. Standard Test Method for Plane Strain Fracture Toughness of Metallic Materials, 1997.
83. E1820-01, Standard Test Method for Measurement of Fracture of Toughness, ASTM, 2001.
84. T. L Anderson., *Fracture Mechanics*, 2005, pp. 300.
85. E1820-11, Standard Test Method for Measurement of Fracture Toughness, ASTM, 2011.
86. X.Chen, R. K. Nanstad, M.A. Sokolov, E. T. Manneschmidt, Advanced Materials & Processes, 2014, pp.19-23.
87. M. F. Hafiz, T. Kobayashi, *Journal of Materials Science*, vol. 31, 1996, pp. 6195-6200.

88. M. Tirayakioglu, *Mat. Sci. Eng. A.*, 497, vol. 2008, pp. 512-514.
89. K., Tohgo, M. Oka, *Key Engineering Materials*, 2004, pp. 261-263.
90. K. Lee, Y. N. Kwon, S. Lee, *J. Alloys Compd.*, vol. 461, 2008, pp. 532-541.
91. N. D. Alexopoulos, M. Tirayakioglu, *Metall. Mater. Trans. A*, vol. 40, 2009, pp. 702.
92. J. T. Staley, ASTM STP, vol. 605, 1976, pp. 71-96.
93. W. J. Sames, F. A. List, S. Pannala, R. R. Dehoff, and S. S. Babu, *Int. Mater. Rev.*, 2016, vol. 61, pp. 315-360.
94. W. E. Frazier, *J. Mater. Eng. Perform.*, vol. 23, 2014, pp. 1917-1928.
95. C. Gu, W. Meiners, K. Wissenbach, and R. Poprawe, *Int. Mater. Rev.*, vol. 57, 2012, pp. 133-164.
96. C. Herderick, *Mat. Sci. Tech.*, vol. 2, 2011, pp. 1413-1425.
97. J. Kruth, M. Badrossamay, E. Yasa, J. Deckers, L. Thijs, and J. Van Humbeeck, *Proceedings of the 16th international symposium on electromachining*, 2010.
98. A.M. Beese, B. E. Carroll, *JOM*, 2016, vol. 68, pp. 724-734.
99. J. J. Lewandowski and M. Seifi, *Annu. Rev. Mater. Re*s., 2016, vol. 46, pp. 151-186.
100. A.I. Mertens, J. Delahaye, and J. Lecomte-Beckers, *Adv. Eng. Mater*., 2017, pp. 1-13.
101. ASTM Committee F42, "ISO / ASTM 52900-15: Standard Terminology for Additive Manufacturing Technologies - General Principles - Terminology," ASTM International, 2015.
102. ASTM Committee F42, "ISO/ASTM 52921-2013: Standard Terminology for Additive Manufacturing - Coordinate Systems and Test Methodologies," ASTM International. ASTM International, West Conshohocken, PA, 2013.
103. ASTM Committee F42, "ASTM F3122-14: Standard Guide for Evaluating Mechanical Properties of Metal Materials Made via Additive Manufacturing Processes," ASTM International. ASTM International, 2014.
104. ASTM Committee F42, "ASTM F3049-14: Standard Guide for Characterizing Properties of Metal Powders Used for Additive Manufacturing Processes," ASTM International. ASTM International, 2014.
105. ASTM Committee F42, "ASTM F2924-14: Standard Specification for Additive Manufacturing Titanium-6 Aluminum-4 Vanadium with Powder Bed Fusion," ASTM International. ASTM International, 2014.
106. A.E. Patterson, S.L. Messimer, P.A. Farrington, *Technologies*, vol. 5, 2017, pp. 15.

107. M. Tang. Inclusions, Porosity and Fatigue of AlSi10Mg Parts Produced by Selective Laser Melting, PhD. Dissertation, Carnegie Mellon University, 2017, p. 903.
108. M. Seifi, A. Salem, J. Beuth, O. Harrysson, J.J. Lewandowski, *JOM,* vol. 68(3) 2016, pp. 747-764.
109. S. Gorsse, C. Hutchinson, M. Gouné, R. Banerjee, *Sci. Technol. Adv. Mater*., vol. 18(1), 2017, pp. 584-610.
110. K. Kempen, L. Thijs, J. Van Humbeeck, and J.-P. Kruth, *Mater. Sci. Technol.,* vol. 31(8), 2015, pp. 917-923.
111. J. E. Hatch, "Constitution of Alloys," in Aluminum: Properties and Physical Metallurgy, Metals Park, Ohio: American Society for Metals, 1984, pp. 48.
112. J. F. Major, R. T. Alcan, ASM Handbook Volume 15: Casting, ASM International Handbook Committee, 2008, pp. 1059-1084.
113. Sercombe T.B., Li X., *Mater. Technol.,* vol.31, pp. 77-85.
114. Kempen K., Thijs L., Van Humbeeck J., Kruth J.P., *Phys. Procedia*., vol. 39, 2012, pp. 439-446.
115. C. Buchbinder, W. Meiners , K. Wissenbach, R. Poprawe, *J. Laser Appl,* vol.27, 2015.
116. L.P. Lam, D.Q. Zhang, Z.H. Liu, C.K. Chua, *Virtual Phys. Prototyp*., vol. 10, 2015, pp. 207-215.
117. K.G. Prashanth, S. Scudino, H.J Klauss, K.B. Surreddi, L. Löber, Z. Wang, A.K. Chaubey, U. Kuhn, J. Eckert, *Mater. Sci. Eng. A.*, vol. 590, pp. 153-160.
118. D. Manfredi, F. Calignano, M. Krishnan, R. Canali, E.P. Ambrosio, S. Biamino, D. Ugues, M. Pavese, *Light Metal Alloys Applications,* 2014. pp. 3-34.
119. D. Manfredi, F. Calignano, M. Krishnan, R. Canali, E.P. Ambrosio, E. Atzeni. *Materials,* vol. 6, 2013, pp. 856-869.
120. W. Li, S. Li, J. Liu, A. Zhang, Y. Zhou, Q. Wei, C. Yan, Y. Shi, *Mater. Sci. Eng. A,* vol. 663, 2016, pp. 116-125.
121. C. Brandl, U. Heckenberger, V. Holzinger, and D. Buchbinder, *Mater. Des*., vol. 34, 2012, pp. 159-169.
122. J. Fiocchi, A. Tuissi, P. Bassani, C.A. Biffi, *J. Alloys Compd*., vol. 695, 2016, pp. 3402-3409.
123. X. P. Li, X. J. Wang, M. Saunders, A. Suvorova, L. C. Zhang, Y. J. Liu, M. H. Fang, Z. H. Huang, T. B. Sercombe, *Acta Mater*., vol. 95, 2015, pp. 74-82.

124. I. Rosenthal, A. Stern, N. Frage, *Metallogr. Microstruct. Anal.*, vol. 3, 2014, pp. 448-453.
125. N. Read, W. Wang, K. Essa, M.M. Attallah, *Mater. Des.*, vol. 65, 2015, pp. 417-424.
126. E. Louvis, P. Fox, C.J. Sutcliffe, *J. Mater. Process. Technol.*, vol. 211, 2011, pp. 275-284.
127. A. Tridello, C.A. Biffi, J. Fiocchi, *Fatigue Fract. Eng. Mater. Struct.*, vol. 41, pp. 1918-1928.
128. S. Bagherifard, N. Beretta, S. Monti, *Mater. Des.*, vol. 145, 2018, pp. 28-41.
129. I. Maskery, N. T. Aboulkhair, C. Tuck, R. D. Wildman, I. A. Ashcroft, N. M. Everitt, and R. J. M. Hague, *Solid Freeform Fabrication Symposium, Austin, TX*, 2015, pp. 1017–1025.
130. S. Siddique, M. Imran, E. Wycisk, C. Emmelmann, F. Walther, *J. Mater. Process. Technol.*, vol. 221, 2015, pp. 205-213.

Articles

Article 1

The Influence of Ni and V Trace Elements on High-Temperature Tensile Properties and Aging of A356 Aluminum Foundry Alloy

M.T. Di Giovanni, E. Cerri, M. Merlin, D. Casari, G.L. Garagnani, L. Arnberg

Metallurgical and Materials Transactions A, vol. 47(5), 2016, pp. 2049-2057

The influence of Ni and V trace elements on high temperature tensile properties and aging of A356 aluminium foundry alloy

M.T. Di Giovanni*, E. Cerri*, L. Arnberg°, M. Merlin§, G.L. Garagnani§

*Dip. Ingegneria Industriale, Università di Parma, v.le G. Usberti 18/A, 43124-Parma (ITALY)

° Dept. Materials Science and Engineering, N.T.N.U. A. Getz vei 2, N-7491 Trondheim (NORWAY)

§ Dip. Ingegneria, Università di Ferrara, v. Saragat 1, 44122-Ferrara (ITALY)

ABSTRACT

High-temperature tensile properties of unmodified A356 alloy with and without the addition of Ni or V in traces (600 and 1000 ppm of Ni and V, respectively) were investigated by analysing samples obtained from sand and permanent mold castings in the as-cast and T6 heat-treated conditions. Tensile tests were performed at 508 K (235 °C) at a crosshead speed of 1 mm/min. In addition, samples were subjected to artificial aging at 508 K (235 °C) for different times, and corresponding hardness curves were plotted. Microstructures and fracture surfaces, analyzed by FEG-SEM equipped with energy dispersive X-ray spectroscopy, showed that neither Ni nor V addition had a detrimental effect on high-temperature tensile properties. Aging curves showed a strong loss of hardness affecting the T6 class between 30-min and 1-h exposure time. After 6-h aging, no evidence of aging treatment persisted on hardness of the tested material. Hardness values did not reveal any significant difference between the reference alloy and the Ni- and V-containing alloys in both casting conditions, in complete analogy with the tensile properties. Unmodified eutectic silicon particles provided inhomogeneity in the a-Al matrix and acted as the principal source of stress concentration leading to fracture.

Introduction

In the last decades, aluminum alloys have been re-focused in terms of lightweight material for vehicles. Replacing cast iron with aluminum alloys can result in a significant weight reduction and consequently better fuel efficiency [1,2]. High-temperature performance is a critical characteristic affecting an alloy's suitability for various automotive power-train applications. Contemporary automotive engines operate at the highest temperatures reaching up to 523 K (250 °C) [3]. This creates demanding operating requirements for the existing Al-Si-Cu and Al-Si-Mg alloys that typically lose strength above 423 K (150 °C) [4-7]. Industries have also shown a growing interest in the effect of increased Ni and V levels on the mechanical properties of aluminum alloy products. In fact, the deterioration in the coke quality and, as a result, in the quality of the anodes used in the Hall-Heroult process has led to an increase in the amount of these metal impurities in the downstream products. In the next years, the levels of Ni and V are expected to rise to 420 and 1080 ppm, [8] respectively. At present, there is no cost efficient method available for the removal of these impurities, and the response to the problem is mainly monitoring the Ni and V levels and checking for any negative influence [9]. Therefore, considering the new trends, it might be interesting to understand which role is played by Ni and V additions on the high-temperature mechanical behavior. A previous study investigated the room temperature tensile properties of sand cast and permanent mold cast unmodified A356 alloy containing 600 and 1000 ppm of Ni and V, respectively [10]. It was found that Ni and V strongly affect both the yield strength ($Rp_{0.2}$) and ultimate tensile strength (UTS) of the sand cast alloy in the as-cast condition. In particular, Ni reduces $Rp_{0.2}$ and UTS by 87 and 37 pct., respectively, whereas V increases $Rp_{0.2}$ and UTS by 42 and 25pct. Hence, the objective of this work is to evaluate the influence of Ni and V trace elements on the high-temperature tensile properties of the unmodified A356 foundry alloy in the as-cast and T6 heat-treated condition, solidified by means of both sand and permanent mold casting processes. High-temperature tensile tests and hardness measurements were performed to assess the mechanical properties. Observing the small elongation values, it is reasonable to assume that the kinetic of the strain hardening mechanism is mostly ruled by the effect of the temperature than to the effect of dynamic strain. Hence, aging curves were plotted in order to verify if the samples are susceptible to aging at the testing temperature. Moreover, microstructure and fracture surfaces were observed by means of Optical Microscopy (OM) and Scanning Electron Microscopy (SEM).

Experimental Details

Material

In this study, the hypoeutectic A356 foundry alloy was used as base alloy. As described in a previous work [10]. the as-received ingots were melted in charges of 16 kg each in a boron nitride-coated clay graphite crucible. Trace elements were added in concentrations of 600 and 1000 ppm of Ni and V, respectively. Neither Sr nor Na was added as modifier agent. Samples from the three different casting trials were obtained and subsequently analyzed by Optical Emission Spectroscopy (OES). The chemical compositions of the A356 reference alloy and the Ni- or V-containing alloys are given in Table 1.

Table 1. - *Chemical composition (wt %) of A356 reference alloy and Ni/V- containing alloys as measured by OES.*

Alloy	Addition (ppm)	Si	Fe	Mg	Ni	V	Al
A356	-	7.054	0.092	0.355	0.003	0.007	bal.
A356 + Ni	600	6.902	0.087	0.344	0.061	0.007	bal.
A356 + V	1000	6.992	0.094	0.349	0.003	0.108	bal.

Casting and Heat Treatment

After the melt preparation, the alloys were poured in both sand and steel molds. Sand castings were obtained using an improved version of the tensile testing bars proposed by Dispinar and Campbell [10,11]. The cooling rate in the middle of the sand cast specimen was 1.3 K/s. In accordance with the UNI 3039 specification, an L-shaped steel mold was chosen for the permanent mold castings. The temperature of the die was kept at 573 K (300 °C) during the casting trials. The cooling rate in the middle of the permanent mold cast specimen was 4.2 K/s. Part of the samples originating from both the casting methods were subjected to a T6 heat treatment. They were solubilized at 813 K (540 °C) for 4 hours, quenched in a water bath at 293 K (20 °C), and finally aged at 433 K (160 °C) for 6 hours. Twelve different experimental conditions were investigated (Table 2), and at least five specimens were tested for each condition.

High-Temperature Tensile Tests

High-temperature tensile tests were performed on a MTS 880 universal testing machine (10 tons) equipped with a furnace chamber and a MTS Teststar control unit. All the specimens were tested at 508 K ± 5 K (235 °C ± 5 °C), at a crosshead speed of 1 mm/min and with the applied load restricted to 40 kN. To ensure the thermal stability in the whole specimen, the sample was exposed to the preset temperature for 15 min before the beginning of the test. One dummy specimen was used to directly check the temperature by placing a thermocouple at its center plane. A specifically designed clip-on stainless steel axial extensometer connected to an optical position measuring system was used to collect the stress-strain data.

Table 2. - *Specimens condition specification.*

Alloy	Mold	Condition	Alloy Code
A356	Sand	as-cast	A356 AC
		T6	A356 T6
A356 + 600 ppm Ni	Sand	as-cast	N AC
		T6	N T6
A356 + 1000 ppm V	Sand	as-cast	V AC
		T6	V T6
A356	Permanent Mold	as-cast	A356 PM AC
		T6	A356 PM T6
A356 + 600 ppm Ni	Permanent Mold	as-cast	N PM AC
		T6	N PM T6
A356 + 1000 ppm V	Permanent Mold	as-cast	V PM AC
		T6	V PM T6

Microstructure Analysis

After tensile tests, the specimens were prepared for the microstructural analysis. Samples for fractographic investigation were sectioned parallel to the fracture surface and cleaned in an ultrasonic bath to remove all debris, grease or oils due to the cutting process. Samples for metallographic investigation were sectioned perpendicular to the fracture surface and embedded in a low-viscosity epoxy resin. The grinding procedure was performed by SiC papers, from 320 up to 2400, by applying a force of 15 N for 60 s. The samples were then

polished using MD-Mol (3 µm) at 15 N for 6 min and subsequently MD-Nap (1 µm) at 15 N for 6 min. Microstructures and fracture surfaces were observed by means of a HITACHI SU-6600 Field Emission Scanning Electron Microscope (FEG-SEM) equipped with Energy Dispersive X-ray Spectroscopy (EDS).

Ageing and Vickers Hardness Evaluation

A set of samples not subjected to mechanical test underwent Vickers Hardness Test. Cylindrical samples about 1 cm in diameter were cut and artificially aged at 235±3 °C to determine the ageing curves. The exposure times were 5 min, 10 min, 15 min, 20 min, 30 min, 1 h, 2 h, 4 h, and 6 h. After ageing, hardness samples were ground flat and testing surfaces where finished with 1200 SiC paper. Vickers microhardness tests (HV) were performed in the center of the cylindrical samples' base at a load of 300 g and a dwell time of 15 s, according to UNI EN ISO 6507 specification.

Results and Discussion

High Temperature Tensile Properties

Figures 1 and 2 collect the average values of the high temperature tensile properties of the sand cast and permanent mold cast alloys. No relevant differences between the reference alloy and the Ni- and V-containing alloys were found in both casting conditions.
This indicates that neither Ni nor V addition (600 and 1000 ppm, respectively) influences the high temperature mechanical behavior. $Rp_{0.2}$ and UTS data have small error bars indicating the reproducibility and the reliability of the data, whereas A% error bars are larger. This is most likely due to the microstructure, in particular to the faceted flake-like shape of the eutectic Si particles, which affect the fracture initiation and propagation.
Figure 1 summarizes the high temperature tensile properties of the sand cast alloys (A356 and Ni/V- containing alloys), in the as-cast (Figure 1(a)) and in the T6 condition (Figure 1(b)) respectively. With respect to the sand cast case, the precipitation of fine coherent Mg_2Si particles in the α-Al matrix, promoted by the T6 heat treatment, exerts a strong effect on the strength of the material [9]. This is clearly indicated by the significant increase in yield strength ($Rp_{0.2}$) and in ultimate tensile strength (UTS) by 78% and 54%, respectively, compared to the as-cast samples. The coherent Mg2Si precipitates with their needle-like

shape can counteract the glide of dislocations, which accumulate and significantly strengthen the α-Al matrix.

Despite this improvement and the α-Al matrix is more easily susceptible to cracking. As a result, when the fracture of the brittle eutectic particles begin, the propagation of crack through the matrix is easier, requiring a lower amount of energy. Hence, this leads to a remarkable reduction in the ductility (in terms of elongation A%) of the T6 treated alloy compared to the corresponding as-cast alloy. Moreover, as-cast specimens showed a lower $Rp_{0.2}$/UTS ratio than the T6 treated samples.

This is probably due to the presence of reinforcing precipitates that block the motion of the dislocations and lead the heat treated material to require higher stress to yield. Figure 2 summarizes tensile test results at 235 °C for the permanent mold cast alloys, in both as-cast (Figure 2(a)) and T6 conditions (Figure 2(b)). In general, their mechanical properties are higher than those obtained for the sand cast alloys. As shown in Figure 1 and 2, the increase in permanent mold cast samples' yield strength is not substantial (average increments range from 3 to 15 MPa). It is worth noting, however, that yield strength data do not overlap each other's except for a couple of conditions, i.e. for the A356-AC and N-T6 alloys. Hence, the slight increase in yield strength is statistically relevant and can reasonably be ascribed to the finer microstructure obtained through permanent mold casting. Comparing the T6 heat treated samples with the as-cast ones, $Rp_{0.2}$ and UTS increased by 65% and 47%, respectively.

Considering the analogy with the sand cast case, the effect of precipitation hardening on the tensile properties at elevated temperature of permanent mold cast samples will not be discussed. The elongation (A%) values show a low scattering of data in both conditions. In absence of casting defects, ductility of A356 alloys is controlled by SDAS, size and aspect ratio of eutectic particles, which are strongly dependent on the cooling rate [10].

The increase of the cooling rate during solidification decreases the SDAS and subsequently divides the eutectic liquid into many small pockets rather than the large eutectic regions present in the low cooling rate structure [7].

A finer structure with smaller and more rounded particles, as well as long dislocation slipping distances within the grains, results in a lower particle cracking rate and hence a higher ductility [11]. With respect to the elongation, it is observed in Figure 2(a) and 2(b) that the ductility improvement linked to the necking and spheroidization eutectic Si particles during the solubilization stage is less meaningful than the contribution given by the higher cooling rate. Therefore, the cooling rate is the leading parameter affecting the

ductility of this class of materials. Elongation values evidenced a uniform trend for all the classes considered, except for the as cast Ni-containing alloy, which slightly differs from the tendency. A lower $Rp_{0.2}$ /UTS ratio is observed in the permanent mold samples compared to the sand cast samples, mostly due to the higher ultimate tensile strength resulting from this casting technology. Concerning the as-cast condition, (Figures 1(a) and 2(a)) permanent mold tensile samples show slightly improved mechanical properties compared to the sand cast ones: 8% for the $Rp_{0.2}$ and 11% for the UTS (average values). Consistently with the conventional knowledge, the slowly solidified structure of the sand cast samples offers a more segregated eutectic structure. The size and the amount of large Si particles are larger, which strongly affects the mechanical behavior. When it comes to the A%, the first data that leap out is the discontinuity ruled by the Ni, in both cases. The effect of Ni-bearing intermetallic was already discussed in the first part. In addition, considering the large error bars, improvements in ductility, promoted by the grain refining, has no statistic relevance. Regarding the T6 condition, experimental results are quite similar for the two casting methods (Figures 1(b) and 2(b)).This proves that the solidification microstructure, whose size and shape are linked to the cooling rate, is less influent than the Mg_2Si precipitation hardening on the mechanical properties at elevated temperature.

Microstructural Analysis

Microstructural investigations were performed by analyzing the fracture profiles of the samples. Backscattered electron (BSE) images of the A356 reference alloys as well as of Ni- and V- containing alloys in as-cast and T6 heat treated conditions are shown in Figure 3. For the sake of clarity, only the sand cast samples are presented.

The main features are α-Al dendrites and needle- like Si eutectic particles. Fe-bearing phases such as π-$Al_8FeMg_3Si_6$ and β-Al_5FeSi, Ni-rich intermetallic compounds (Al_3Ni and Al_9FeNi), as well as Mg_2Si particles are also observed.

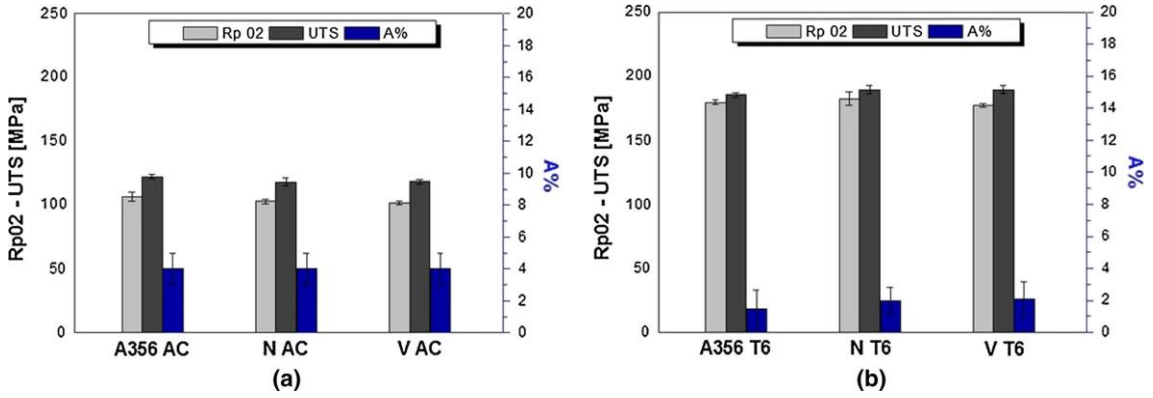

Figure 1 – *High temperature tensile properties of the sand cast A356 reference and Ni/V-containing alloys a) in the as-cast condition and b) in the T6 condition.*

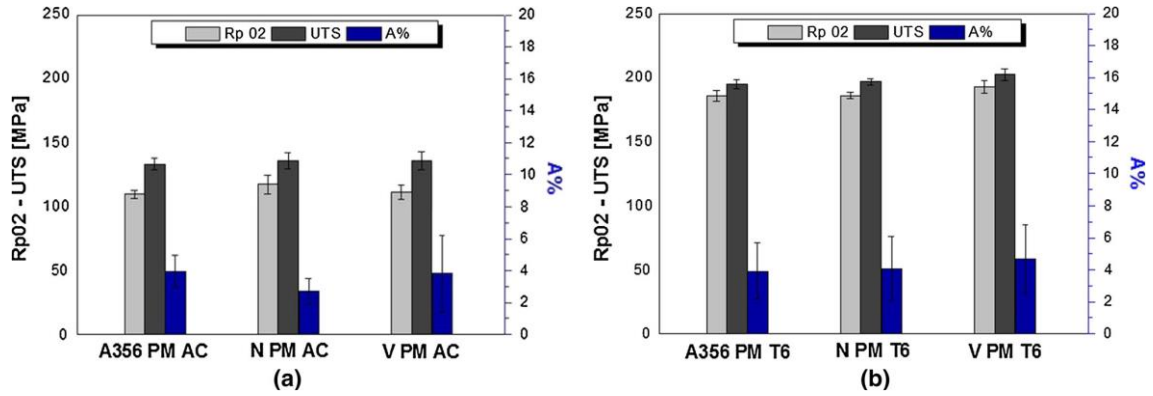

Figure 2 – *High temperature tensile properties of the permanent mould reference and Ni/ V- containing alloys a) in the as-cast condition and b) in the T6 condition.*

In the eutectic region, platelet-like *β-Al_5FeSi* intermetallics are occasionally found associated with the "Chinese Script" *π-$Al_8FeMg_3Si_6$* phase (Figure 3(c)). Ni-based intermetallics phases, exhibiting a polyhedral shape, are observed in the sand cast alloy with Ni addition (Figure 3(c),(d)). A slight increase in the amount of *π-$Al_8FeMg_3Si_6$* and Mg_2Si intermetallic compounds is observed in the V- containing samples (Figure 3(e),(f)). As reported in [7], this may be related to a competition with Mg as a solid solution element in α-Al matrix. By entering solid solution, V allows more Mg to be available in the remaining liquid during solidification, which in turn yields to a larger amount of Mg-containing intermetallics in the eutectic region. A moderate spheroidization of eutectic

Si particles is noted in the T6 heat-treated samples due to solution heat treatment. Fe-bearing compounds have a more marked tendency to spheroidize, as shown in Figure 3(b),(d).

Fractographic Observations

Figure 4 shows the fracture profile of the A356 reference alloy (Figure 4(a),(b)), Ni-containing (Figure 4(c),(d)) and V-containing (Figure 4(e),(f)) alloys in as-cast and T6 heat treated conditions. It is evident that the fracture path mainly follows the eutectic region, as indicated by the arrows in Figure 4(a),(b). A significant plastic deformation of α-Al dendrites is also noticed in all the investigated alloys (Figure 4(c)). Below the main fracture, multiples cracks oriented perpendicularly to the applied stress are observed in both Si particles and Fe-bearing phases (Figure 5). Similar fracture paths are observed in the T6 heat treated alloys. SEM micrographs of the fracture surfaces (Figure 6) are in line with room temperature findings [7], and confirm the Si-driven quasi cleavage nature of the fracture, as evidenced by the number of cleavage planes and brittle Si-flakes. Few dimples are detected, as shown in Figure 6(a),(b). In the absence of modifier elements such as Sr or Na, the selected solution heat treatment holding time appears to be insufficient to obtain complete necking and spheroidization of the Si particles. In fact, the majority of eutectic Si crystals still show an elongated acicular morphology. These elongated particles, acting as the principal source of stress concentration generally initiate fracture [12,13]. Larger eutectic silicon particles cluster along both cell and grain boundaries generating a nearly continuous wall of eutectic silicon particles around the dendrite cell. Microcracks originated in those Si particles propagate through the α-Al matrix and subsequently connect to each other to produce the main crack. Eutectic Si particles segregated along cells were cracked first and the fracture of the Si-eutectic causes the formation of flat areas, cleavage planes as indicated by circle in Figure 6 (a),(b). Al-dendrite cells behave similar to grains where the strong interaction between particles and slip bands at the cell boundaries, originated during the plastic deformation process, is capable to counteract crack propagation. Where the soft α-Al matrix presents low E, the intermetallics and the eutectic Si-Crystal are hard and present high E. When this material is subject to external loads, difference in the nature of the component, turns into an inhomogeneity in stress distribution.

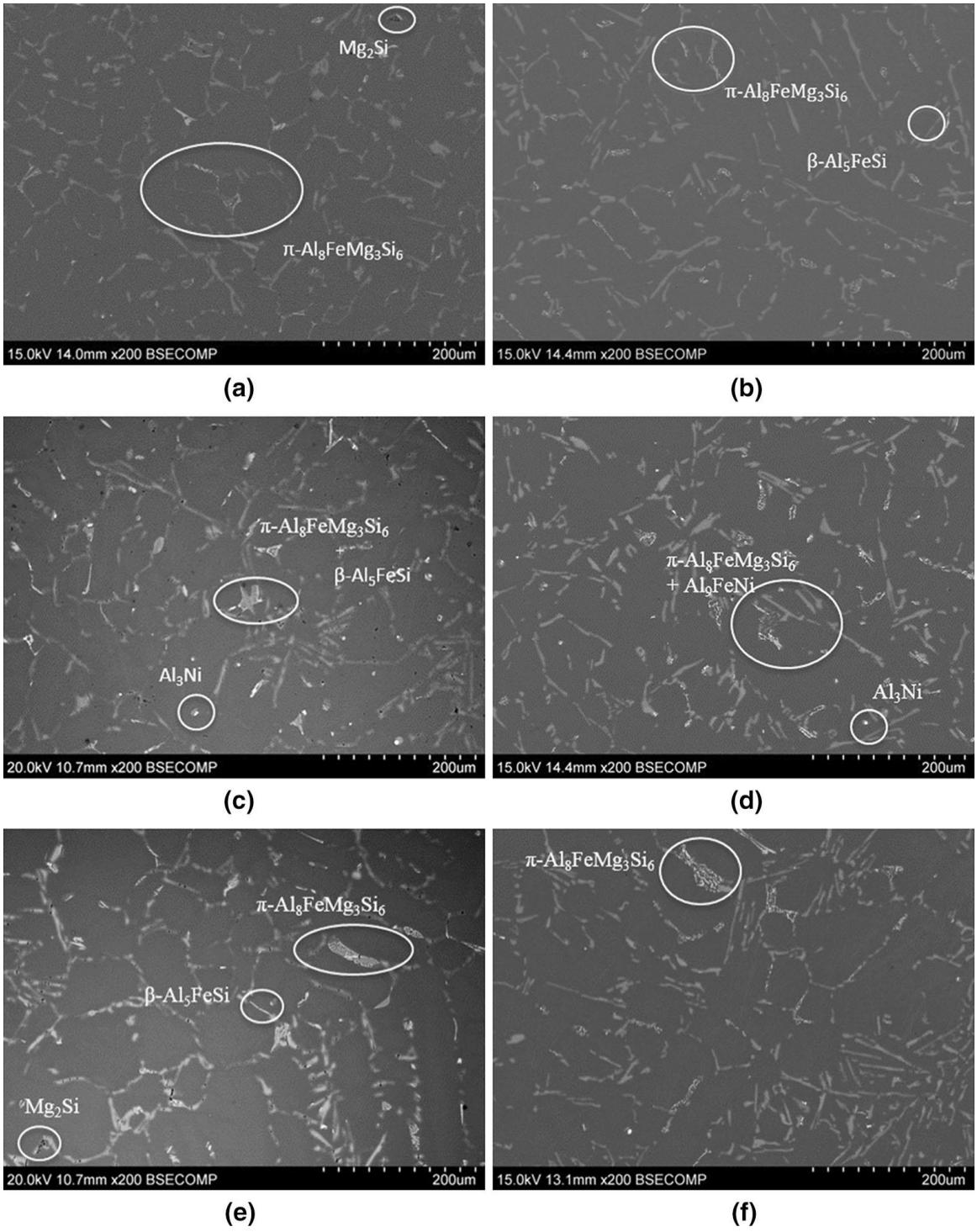

Figure 3 - *BSE micrographs of sand cast reference, Ni and V- containing alloys in as-cast and T6 conditions tested at elevated temperature: (a) A356-AC, (b) A356-T6, (c) N-AC, (d) N-T6, (e) V-AC, (f) V-T6; Aluminium dendrites are in dark grey, eutectic Si crystal in light clear grey, π-$Al_8FeMg_3Si_6$ and β-Al_5FeSi in light clear grey, Mg_2Si in black and Ni-rich intermetallics in white.*

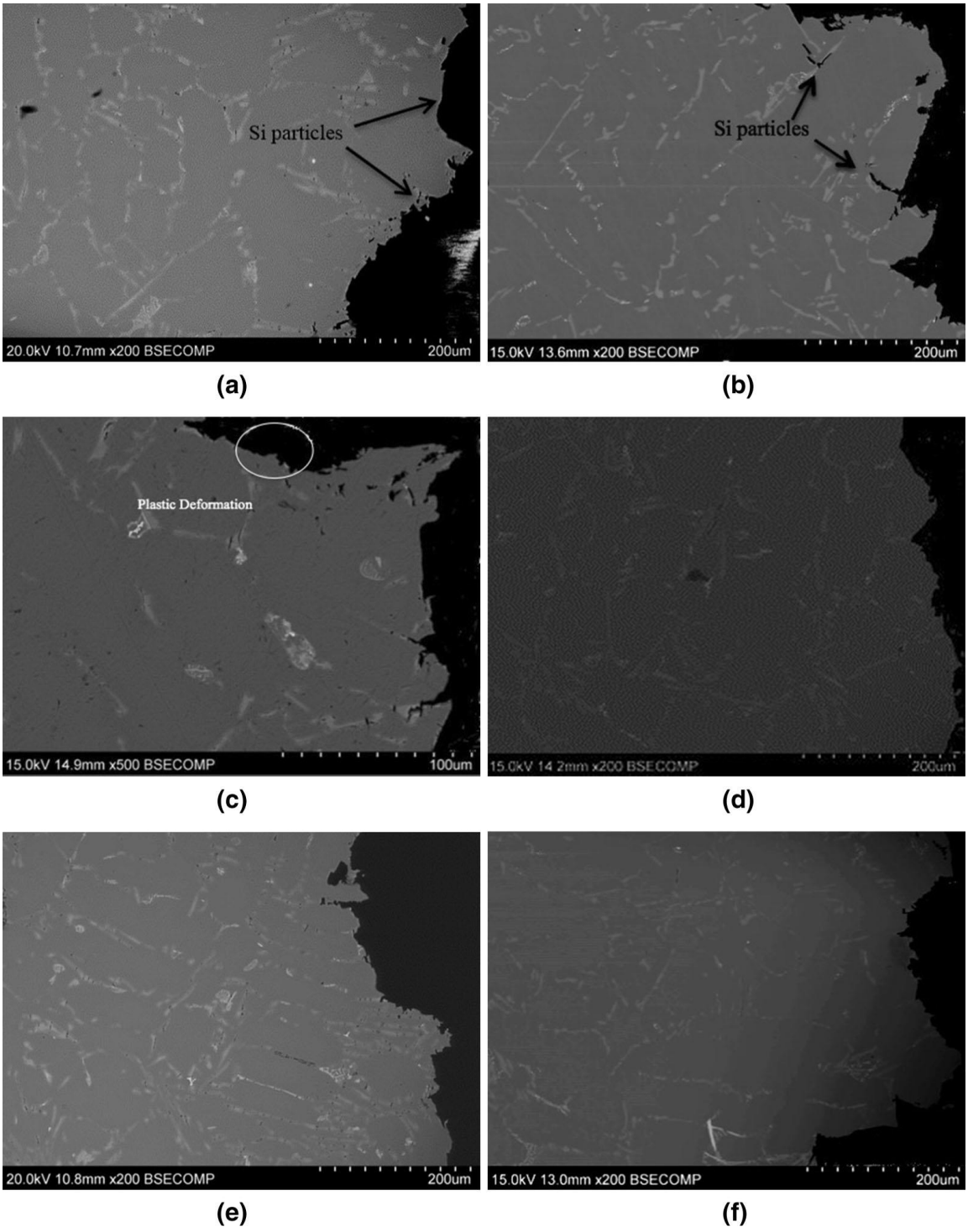

Figure 4 - *BSE micrographs of the fracture profile of sand cast A356 reference, Ni- and V- containing alloys in as-cast and T6 conditions tested after high temperature tensile test: (a) A356-AC, (b) A356-T6, (c) N-AC, (d) N-T6, (e) V-AC, (f) V-T6. A Si-driven quasi-cleavage and matrix crack are the main fracture mode. No significant differences between crack paths of as-cast and T6 heat treated alloys are observed.*

Harder particles generally reinforced the matrix by bearing the main part of the applied load, in perfect analogy with the composite materials. If the stress induced at the particles or at the matrix-particles interface exceeds a critical value, then fracture of the particles or decohesion occurs [14,15]. Under the high temperature condition, the α-Al matrix is more capable to be deformed, the internal stress originated by the non- homogeneity is partially recovered at the expense of the matrix. Hence fracture occurs at lower strength values compared with the room temperature case [7], but offer higher elongation. After T6 heat treatment, the precipitation of fine coherent Mg2Si phases in the α-Al matrix exerts a strong effect on the tensile properties of both the sand cast and permanent mold cast samples. Despite this improvement, the α-Al matrix is prone to crack more easily due to the hardening particles, in fact when the fracture of brittle particles begins, the following microcrack linking process is faster and leads to a slightly lower ductility compared to the corresponding as-cast alloys [7]. In order to offer a comprehensive evaluation of the influence of Ni and V trace elements on the mechanical properties, their effect on the microstructure (when evident) are reported. Ni-rich intermetallics compounds are detected in sand cast alloys with 600 ppm Ni (Figure 6(c) and (d)).

Aging and Vickers Hardness Evaluation

Vickers hardness tests were carried out in order to endorse the hypothesis of artificial aging occurred during the high-temperature tensile tests. The poor ductility exhibited by the alloys in all the experimental conditions (Figures 1 and 2) allowed us to compare the aging occurring in static condition to the one achieved through the tensile test at elevated temperature, where it is reasonable to assume that the kinetic of the strain hardening mechanisms is mostly ruled by the effect of the temperature than by dynamic strain. Vickers Hardness measurements were obtained after aging the A356 base alloy and the Ni- and V-containing alloys at 508 K (235 °C) (testing temperature) with different aging times (Figure 7). The first values (t = 1 s) are representative of the as-given samples, which are taken as reference values for the aging evaluation. Vickers Hardness curves are organized as follows: on the left side the as-cast samples, sand (Figure 7(a)) and permanent mold (Figure 7(c)) casting methods; on the right side the T6 heat-treated samples, sand (Figure 7(b)) and permanent mold (Figure 7(d)) casting techniques.

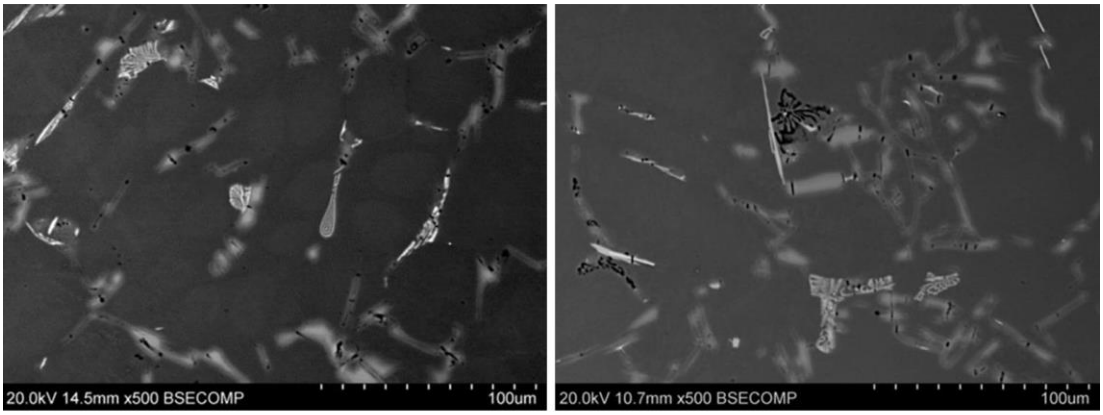

Figure 5 - *BSE micrographs of the not treated sand cast A356 alloy close to the fracture surface, showing Si-particles and Fe-bearing compounds cracked.*

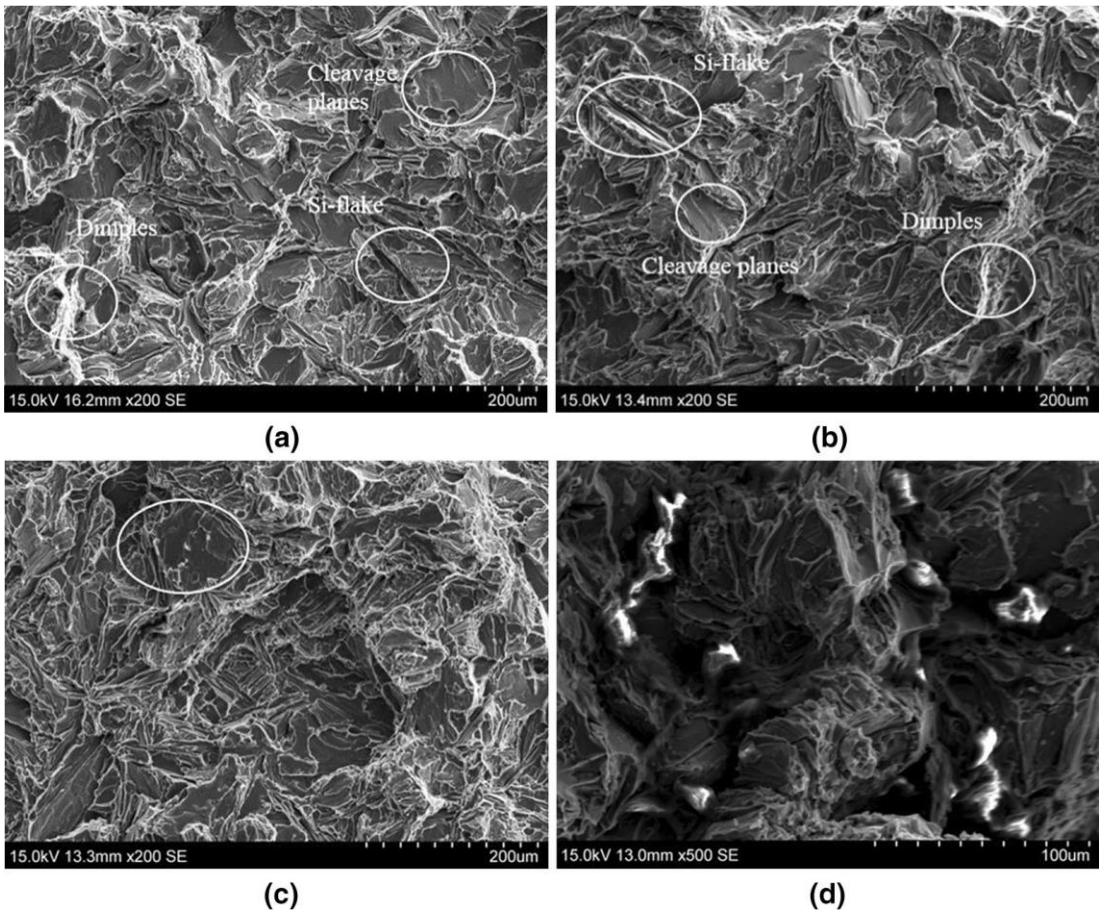

Figure 6 - *BSE micrographs of the fracture surfaces of sand cast A356 reference in as-cast (a) and T6 conditions (b) tested after high temperature tensile test showing the typical features of ductile-brittle mixed fracture. The flake-like morphology of Si particles persists after the solution heat treatment. Ni-rich intermetallics compounds detected in a sand cast as-cast alloy with 600 ppm Ni (c),(d).*

At t = 1 s, the as-cast and T6 samples poured in the permanent mold present slightly higher hardness values (~5, ~3HV) than the sand cast samples, in agreement with the tensile values presented in [10]. After a 5-min aging time, a clear strengthening is observed for each experimental condition. The effect becomes more evident after 10 and 20 minutes, where the as-cast and the T6 classes achieve their hardness peak, respectively. The alloys in the T6 condition are subjected to a strong hardness decrease. After a 6-hour aging, an average reduction of 56 and 60 HV (approximately 50 pct. lower than the peak hardness) can be observed for the sand cast and permanent mold cast alloys, respectively. In contrast, the alloys in the as-cast condition exhibit a smoother hardness variation: after the peak values of 75 HV (sand cast) and 82 HV (permanent mold), a slight decrease in hardness by 16 and 25 pct. is observed at 6 hours aging, and minimum values of 63 HV (sand cast) and 61 HV (permanent mold) are measured. It is worth noting that the as-cast samples did not receive any solution treatment before aging. Therefore, the strengthening attained during this process, depending on the volume fraction and the size of the particles precipitated and on the nature of the interaction of the particles with dislocations, is based on the presence of metastable Mg and Si atoms in the solidified a-Al matrix. Hence, the increase in yield strength at high temperature, as compared to room-temperature experiments [10], could be attributed to the artificial aging activated during tensile test (15 min + test duration at 508 K (235 °C)). As far as the T6 heat-treated alloys are concerned, a strong loss of hardness is evidenced between 30-minutes and 1-hour exposure time. This might be a serious concern for industrial engine applications, where temperatures commonly exceed 473 K (200 °C). In accordance with previous findings [19], it is confirmed that the hardness and thus the mechanical properties of peak-aged [20,21] T6 heat-treated castings could be further modified by the in service conditions of the component, especially after prolonged high-temperature exposure. It is also reasonable to affirm that the combination of temperature (508 K (235 °C)) and duration time (15 min + test duration) of high-temperature tensile tests yields an over-aging of the alloys. In this study, the over-aging was demonstrated through a combination of tensile and hardness tests. However, in order to analyze the microstructural evolution of the Mg_2Si precipitate, a Transmission Electron Microscopy investigation is recommended. With the exception of the A356 PM T6 alloy (Figure 7(d)), the comparison of hardness values did not reveal any significant difference between the reference alloy and the Ni/V-containing alloys in both casting conditions, in complete agreement with the tensile properties.

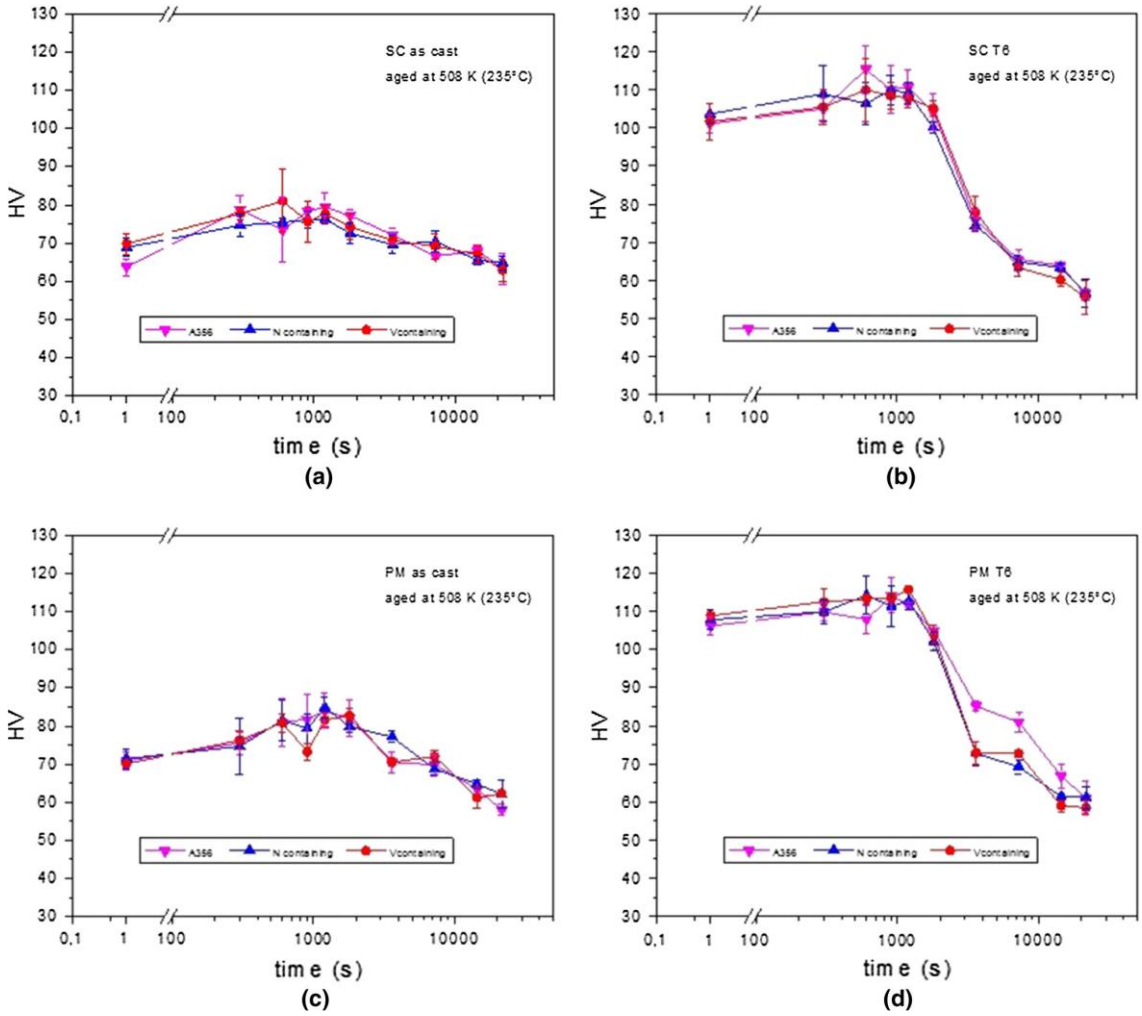

Figure 7 – *Ageing curves at 235°C for the A356 reference, Ni- and V- containing alloys in the 4 different experimental conditions: (a) sand cast as-cast, (b) sand cast T6, (c) permanent mold as cast, (d) permanent mold T6.*

Conclusions

The influence of Ni and V trace elements on the high temperature tensile properties of the unmodified A356 aluminum foundry alloy in as-cast and T6 heat treated conditions was assessed. Both sand and permanent mold casting processes were taken into account. High temperature tensile tests and Vickers hardness measurements were performed to evaluate the mechanical properties. Further, microstructural and fractographic investigations were carried out to analyze the microstructural features involved in the fracture process. The following conclusions can be drawn from this study:

No differences in high temperature tensile properties are observed between the A356 reference alloy and the Ni- and V-containing alloys.

Owing to the finer microstructure, a slight increase in yield strength *(*$Rp_{0,2}$), ultimate tensile strength (UTS) and elongation (A%) is found in the permanent mould cast alloys compared to the sand cast alloys.

The T6 heat treatment is more efficient than the permanent mould casting technique in terms of mechanical reinforcement.

The combination of temperature (235 °C) and duration time (15 min + test duration) of high temperature tensile tests can lead to an over-ageing of the alloys.

Ageing curves show a significant loss of hardness in the T6 alloys between 30 min and 1 h exposure time at 235 °C. After 6 h ageing, no evidence of heat treatment is observed in the investigated alloys. This might be a serious issue for industrial engine applications, where temperatures commonly exceed 200 °C.

SEM investigations of the fracture profiles and surfaces highlight the Si-driven quasi- cleavage nature of the fracture, as proved by the number of cleavage planes and brittle Si- flakes. Few dimples are detected in the fracture surfaces. No significant differences in the fracture paths are observed between the as-cast and the T6 heat-treated alloys.

References

1. W. Kasprzak, D. Emadi, M. Sahoo, and M. Aniolek: Mater. Sci.Forum, 2009, vols. 618-619, pp. 595-600.
2. R. Dhingra and S. Das: J Clean Prod., 2014, vol. 85, pp. 347-58.
3. W. Kasprzak, Z. Deng, J. Powell, M. Niewczas: JILM, 2010, pp. 669-74.
4. R. Molina, P. Amalberto, and M. Rosso: Metall. Sci. Tech., 2011, vols. 29-1, pp. 5-15.
5. R. Molina, P. Amalberto, and M. Rosso: Metall. Sci. Tech., 2011, vols. 29-2, pp. 5-13.
6. Z. Asghar, G. Requena, and F. Kubel: Mater. Sci. Eng. A, 2010, vol. 527, pp. 5691-98.
7. Y. Li, Y. Yang, Y. Wu, L. Wang, and X. Liu: Mater. Sci. Eng. A, 2010, vol. 527, pp. 7132-37.
8. G. Jha, S. Ningileri, X. Li, R. Bowers, B. Sadler (eds.), Light Metals, Wiley, New Jersey, 2013, pp. 929-34.
9. J. Grandfield and J. Taylor: Mater. Sci. Forum, 2009, vol. 630, pp. 129-136.
10. D. Casari, T.H. Ludwig, L. Arnberg, M. Merlin, and G.L.Garagnani: Mater. Sci. Eng. A, 2014, vol. 610, pp. 414-26.
11. D. Dispinar and J. Campbell: Mater. Sci. Eng. A, 2011, vol. 528, pp. 3860-65.
12. G.E. Dieter: Mechanical Metallurgy, 3rd ed., Mc Graw-Hill Book Co., New York, 1986, pp. 188-228.
13. Q.G. Wang: Metall. Mater. Trans. A, 2003, vol. 34A, pp. 2887-99.
14. S.G. Shabestari and F. Shahri: J. Mater. Sci., 2004, vol. 39, pp. 2023-32.
15. Q.G. Wang, C.H. Casaeres, and J.R. Grifhits: Metall. Trans. A, 2003, vol. 34A, pp. 2901-12.
16. I. Fadavi, A. Boostani, and S. Tamanthas: J. Alloys Compd., 2009, vol. 481 (1–2), pp. 220–27.
17. I. Sinclair and P.J. Gregson: Mater. Sci. Techonol., 1997, vol. 13, pp. 709-26.

18. M. Huang and Z. Li: Int. J. Solid. Struct., 2009, vol. 43, pp. 634-41.

19. B. Baradarani and R. Raiszadeh: Mater. Des., 2011, vol. 32, pp. 935-40.

20. P.A. Rometsch and G.B. Schaffer: Mater. Sci. Eng. A, 2002, vol. 325, pp. 424-34.

21. Metals Handbook, 2 Edn, Heat Treating of Nonferrous Alloys,1998, p. 1035.

Article 2

How Slight Solidification Rate Variations within Cast Plate Affect Mechanical Response: A Study on As-Cast A356 Alloy with Cu Additions

M.T. Di Giovanni, E. Cerri, T. Saito, S. Akhtar, P. Åsholt, Y. Li, M. Di Sabatino

Advances in Materials Science and Engineering, vol. 2018(3), pp. 1-11, 2018

How Slight Solidification Rate Variations within Cast Plate Affect Mechanical Response: A Study on As-Cast A356 Alloy with Cu Additions

Maria Teresa Di Giovanni,[1] Emanuela Cerri ,[1] Takeshi Saito ,[2] Shahid Akhtar,[2] Petter Asholt,[2] Yanjun Li,[3] and Marisa Di Sabatino[3]

[1]*Department of Engineering and Architecture, University of Parma, Viale G. Usberti 18/A, 43124 Parma, Italy*

[2]*Hydro Aluminium, Research and Technology Development (RTD), 6601 Sunndalsøra, Norway*

[3]*Department of Materials Science and Engineering, Norwegian University of Science and Technology, Alfred Getz vei 2B, 7491 Trondheim, Norway*

ABSTRACT

The present work investigates a narrow range of secondary dendrite arm spacing (SDAS), in an as-cast A356 alloy with and without copper (Cu) additions. Cu was added to the base A356 alloy melt to reach the target concentration of 0.5 and 1 wt.%. Samples were selected from 3 different positions within the cast plate, offering 30, 35, and 40 μm SDAS variants. Tensile curves revealed a strong influence between the specimen cutting position and strength, with a pronounced effect in the Cu-containing alloys. Hardness measurements did not confirm the tensile response; hence, to understand the phenomenon, microstructural features have been investigated in detail. Eutectic silicon (Si) particle equivalent diameter (ED) size decreased from the top (T) to the bottom (B) position of the cast. Eutectic Si particle surface area (A%) was found to be denser at the B as compared to the T and simultaneously in the Cu-containing alloy as compared to the Cu-free reference alloy. Backscattered electron (BSE) images were employed to investigate the nature of the Cu-rich intermetallic phases. In conclusion, electrical conductivity measurements were performed to confirm the trends observed.

Introduction

Alloy composition and cooling rate play a key role on the castability [1,2] and also on the mechanical properties of Aluminum-Silicon cast alloys. The cooling rate controls the microstructural features of the material including the Secondary Dendrite Arm Spacing (SDAS), which is often used as measure of the grain size of the material, and thus as measure of the mechanical response. The fraction, size, shape and distribution of eutectic silicon particles and intermetallic phases in the aluminum matrix [2,3] also give a crucial contribution in connection with microstructure optimization. Eutectic Si particles, providing inhomogeneity in the α-Al matrix, act as the principal source of stress concentration points [4-6] and therefore, industrial castings are regularly modified by strontium (Sr) additions. Eutectic silicon particles alter their shape from needle-like into fibrous morphology obtaining a more ductile material. Among the Al-Si foundry alloys, the most commonly used are the A356 and the A357, where magnesium (Mg) is the main alloying element due to its appreciable tendency to promote metastable precipitates under age-hardening treatment. Industries, especially in the automotive sector, are showing a growing interest in finding suitable chemical compositions for cast aluminum alloys for high temperature applications (e.g. currently diesel engine cylinder heads reach up to 250° C). In this concern, the addition of copper (Cu) to traditional Al-Si-Mg alloys has been recently investigated [7-9]. In particular, the concomitant presence of the two copper and magnesium in Al-Si-Cu-Mg alloys should in fact enable the precipitation of more stable Cu-based intermetallic precipitates at higher temperatures, leading to enhanced thermal stability of the T6 heat treated alloys [10]. Further than β' (Mg_2Si) and θ' (Al_2Cu) precipitates, present in ternary Al-Si-Mg and Al-Si-Cu alloys [10-15], reinforcing compounds such as the S' phase (Al_2CuMg) [14,16,17] and the Q' phase (whose general stoichiometry is $Al_5Cu_2Mg_8Si_6$) are found in quaternary Al-Si-Cu-Mg alloys. In this context, many studies attested that improvement in strength is achieved at the expense of elongation [3,10]; others instead, reported an increase in high temperature strength due to the addition of Cu up to 0.5 wt.%, without loss of ductility [18,19]. Seifeddine et al. [2,20] found Cu and Mg to promote the formation of bands of coarse Si particles, and to enlarge the solidification interval, increasing risk in forming shrinkage porosity, thus compromising the ductility.

Whereas the most pertinent literature focuses on the influence of a single variable on the mechanical properties of cast Al-Si-Mg alloy, the present study proposes a combined

overview on the well-known A356 foundry alloy. The two aspects of SDAS and Cu additions were correlated in series and parallel. Samples were selected from 3 different positions in the cast, offering 30, 35, 40 µm SDAS variant. Cu was added to the cast to reach the target concentration of 0.5 and 1 wt.%. In addition to the above mentioned issues, Eutectic Si particles size and distribution were analyzed over the six different conditions, and the influence of Cu on the Cu/Mg/Fe-rich phases were examined by scanning electron microscope (SEM) and energy dispersive X-ray spectroscopy (EDS).

Materials and methods

Commercial Sr-modified A356 alloy was melted in a boron-nitride coated clay-graphite crucible at 750 °C, and grain refined by Al-5Ti-1B master alloys additions. Cu was added to the melt in form of pure copper grains according to the targeted nominal concentrations of 0.5 and 1 wt.%. Molten metal was successively stirred and allowed to settle for 30 min to ensure complete dissolution.

Alloys were then degassed with argon for 5 min just prior to be poured in a copper mold of 65x103x40 mm^3. The die was pre-heated at 50 °C for all the casting trials. Samples from the three different melts were taken and analyzed by optical emission spectroscopy (OES). The chemical compositions of the alloys are given in Table 1.

Table 1

Chemical composition (wt.%) of A356 reference alloy and Cu-containing alloys as measured by OES and their classification.

Alloy	Si	Mg	Fe	Cu	Ti	B	Sr	Al	Code
A356 (Reference)	6.624	0.216	0.086	0.006	0.103	4.6 ppm	14. ppm	bal.	**Cu0**
A356 + 0.5 wt.% Cu	6.587	0.258	0.082	0.454	0.105	5.6 ppm	80.8 ppm	bal.	**Cu0.5**
A356 + 1 wt.% Cu	6.915	0.262	0.091	0.983	0.086	5.6 ppm	74.5 ppm	bal.	**Cu1**

The experimental setup for thermal analysis measurements is described as follows: a graphite crucible was preheated at 750°C and placed on the top of the skimmed and thoroughly stirred melt. After the temperatures of crucible and melt had reached equilibrium, samples were taken by submerging the graphite crucibles into the melt. The

filled crucibles were then placed on Fiberfrax board and a K-type thermocouple was lowered into the melt. The thermocouple tip was positioned at the center of the melt. A Campbell logger (Campbell Scientific, Inc., USA) recorded the temperature-time curve at a frequency of 50 Hz. Prior to and after a measurement the range of eventual thermocouple drift was checked against high purity aluminum (Al5N grade) assuming a solidus temperature of 660°C.

Tensile tests were performed at room temperature, using an MTS 810 Universal Testing Machine. The crosshead speed was 1mm/min. The specimens, with a gauge length of 7 mm and cross section of 4 mm x 4 mm, were cut from three different positions in the ingot: at 4 mm from the cast bottom skin, at 8 mm, and 12 mm, respectively referred as Bottom (B), Center (C) and Top (T) (Fig. 1), expecting different solidification rates. Stress-strain curves were obtained by attaching a knife-edge extensometer at the specimens' gauge length and the tensile properties, such as yield strength, ultimate tensile strength and percentage elongation ($Rp_{0.2}$, UTS and A%, respectively) were determined.

Vickers micro hardness tests (HV) were performed at the Bottom, Center and Top of the cast ingots at a load of 300 g and a dwell time of 15 s, according to UNI EN ISO 6507 specification [21]. Further hardness examinations were conducted by means Rockwell hardness measurements, with a load of 60 kgf, and 1/16'' ball intender (HRF) according to UNI EN ISO 6508-2 specification [22]. Electrical conductivity was measured by a Foerster Sigmatest operating at 60 kHz. Samples for microstructural investigations were cut from the tensile specimens, embedded in phenolic resin and prepared using standard grinding and polishing procedures. Microstructure analyses were performed using a LEICA DMi8 polarized light optical microscope (OM) equipped with a LASX image analysis program. SDAS measurements were performed using the line intercept method. Secondary phases were investigated with a ZEISS ULTRA 55 field emission scanning electron microscopy (FE-SEM) and identified through energy dispersive X-ray spectroscopy (EDS), operated at an acceleration voltage of 20 kV. A statistical study on the eutectic Si particles equivalent diameters (ED) and surface areas (SA) has been also carried out. To analyze the particles a specific threshold has been defined: pixel color ranges have been restricted to the scale of light grey corresponding to eutectic Si particles. ED distributions were calculated on images detected at 1000X whereas representative eutectic Si particles surface area distribution over the B, C and T zones at 200X.

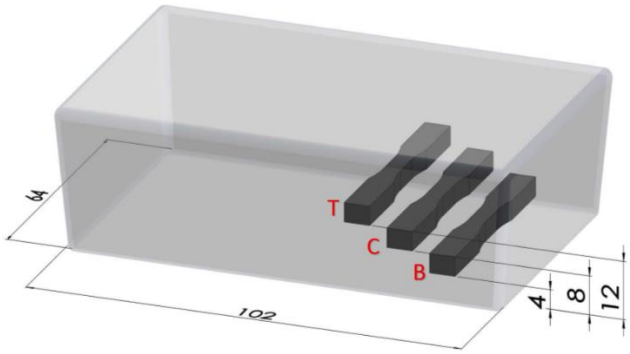

Fig. 1. Specimen cutting position. Respectively, B: Bottom specimen, C: center specimen and T: top specimen (values are given in mm).

Results and discussion

Thermal Analysis

Characteristic temperatures from thermal analysis of A356 reference alloy and Cu-containing A356 alloys are given in Table 2. The two reactions, nucleation and growth of the α-Al phase and start of main eutectic reaction are referred in Table 2 as $T_{N,\alpha}$ and $T_{N,eu,}$ respectively. Nucleation temperature of primary aluminum dendrites ($T_{N,\alpha}$) shifts to a lower temperature with increasing Cu content. According to Arnberg [23] and Bäckerud [24] in commercial unmodified A356 alloy, with a cooling rate of 1.1 K/s before solidification, the precipitation of α-Al starts at 610°C. This temperature varies within the range of 608-615°C with different cooling rates, whereas the Cu0, A356 reference alloy in this study, shows that formation and growth of primary α-Al dendrites begins at 621°C. The shift observed, is mainly imputable to the presence of Ti_2B, well known as excellent grain refiner for this class of material [25]. When it comes to Cu-rich variants, Cu0.5 and Cu1 dendritic networks start to grow at the temperatures of 615°C and 613°C, respectively. The results agree with those presented by Mackay [26] suggesting for an A356 alloy with high Cu content (0.61 wt%) the formation and growth of primary α-Al dendrites at 612°C. Approaching the eutectic transformation, we can observe similar trends and thus, as expected, the eutectic transformation of Cu0 variant occurs at 578 ± 1°C. The influence of Cu is more prominent in this reaction as the Cu0.5 and Cu1 T_{Neu} decrease sensibly by 18°C. Lower eutectic temperatures could be due to the formation of quaternary eutectic phases, as reported by Zeren et al [27].

Table 2
Characteristic temperatures for the nucleation of the α-Al phase and start of main eutectic reaction

Code	Cu conc.	$T_{N,\alpha}$	$T_{N,eu}$
	wt%	°C	°C
Cu0	-	621	578
Cu0.5	0.45	615	563
Cu1	0.98	613	560

Mechanical Properties

Fig.2 summarizes room temperature tensile curves of the three alloys as a function of Cu-content (a,b,c in Fig.2) and specimen cutting position (d,e,f in Fig.2). The curves a,b,c clearly evidence improvement in strength with increasing Cu content, for the three B,C, and T specimens. In parallel, the tendency showed by curves d,e,f in Fig.3 revealed how the specimen cutting position (hence, solidification rate and microstructure) strongly influences the mechanical properties leading to an enhancement in strength by approximately 10% and 20% moving from the top to the bottom in the cast for the Cu-free and the Cu-containing alloys, respectively. Comparing curves b, d and f in Fig.2 i the elongation (A%) decreases with increasing Cu-content. Although it is not straight forward to compare elongations to different studies having different casting conditions, Cu 0.5 and Cu 1 shows somehow range between 6-9% well above literature average [28].

The two phenomena might be related to the solidification mechanism and/or microstructural features. In this light, both these aspects will be investigated. A convenient and widely used measure of the effect of solidification conditions on dendrite structure is the secondary dendrite arm spacing (SDAS). The SDAS, which is the linear distance between two secondary aluminum dendrites (arms), was determined via the mean linear intercept (MLI) method. Fig.3 shows how cooling conditions are strongly subjected to specimen cutting position, even though the region interested is restricted to a distance of 12 mm (see Fig.1). Top SDAS measurements evidenced an increase by 50%, 35% and 25% for the Cu0, Cu1 and Cu0.5 case respectively, as compared to the bottom. B, C and T comprehensive SDAS values are addressed to the nominal 30 µm, 35 µm, 40 µm correspondent values. Results are consistent with material tensile response observed in Fig.2.

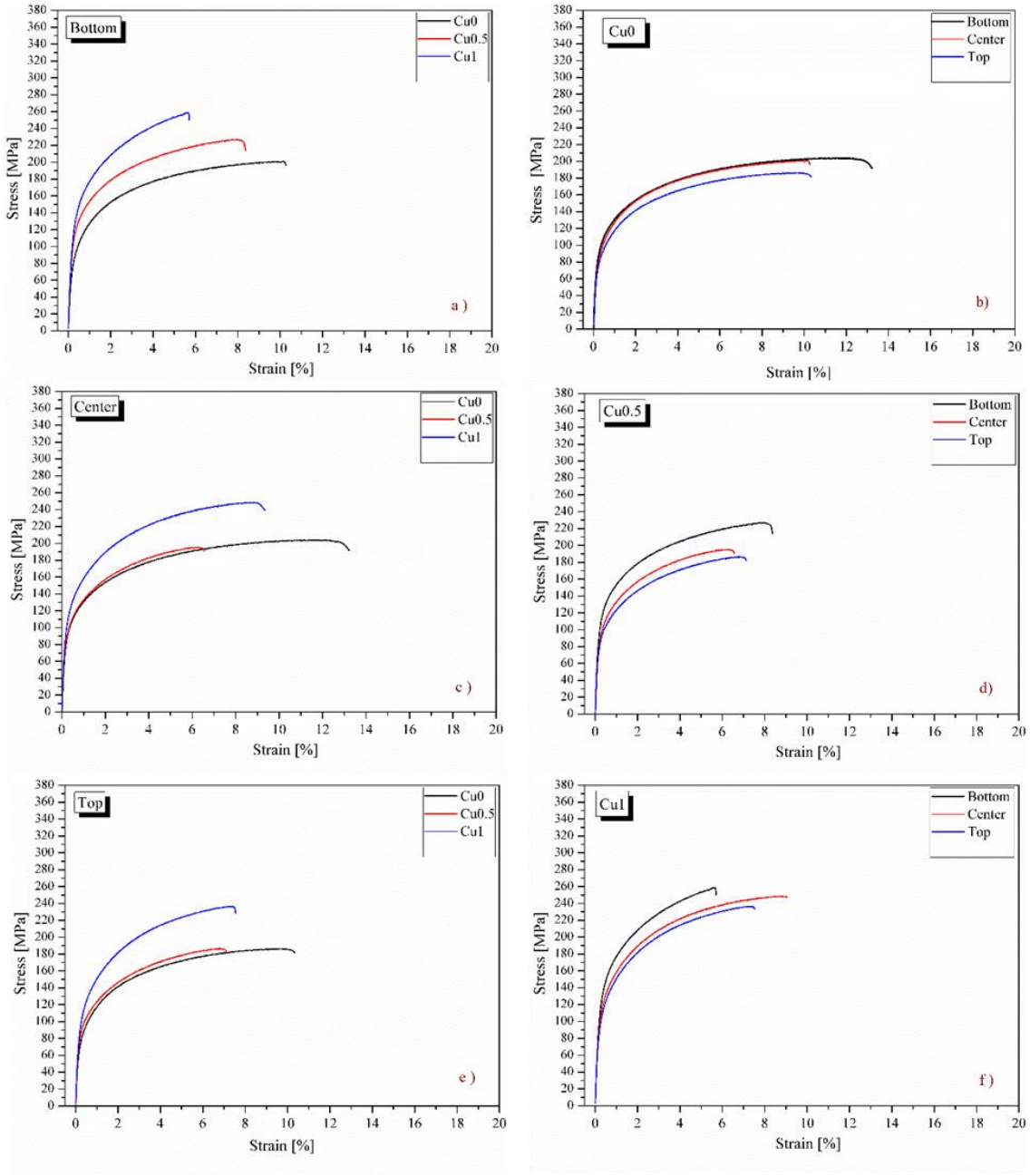

Fig. 2. Tensile strength-strain curves of the three investigated alloys as a function of both Cu-content (a,b,c) and specimen cutting position (d,f,g).

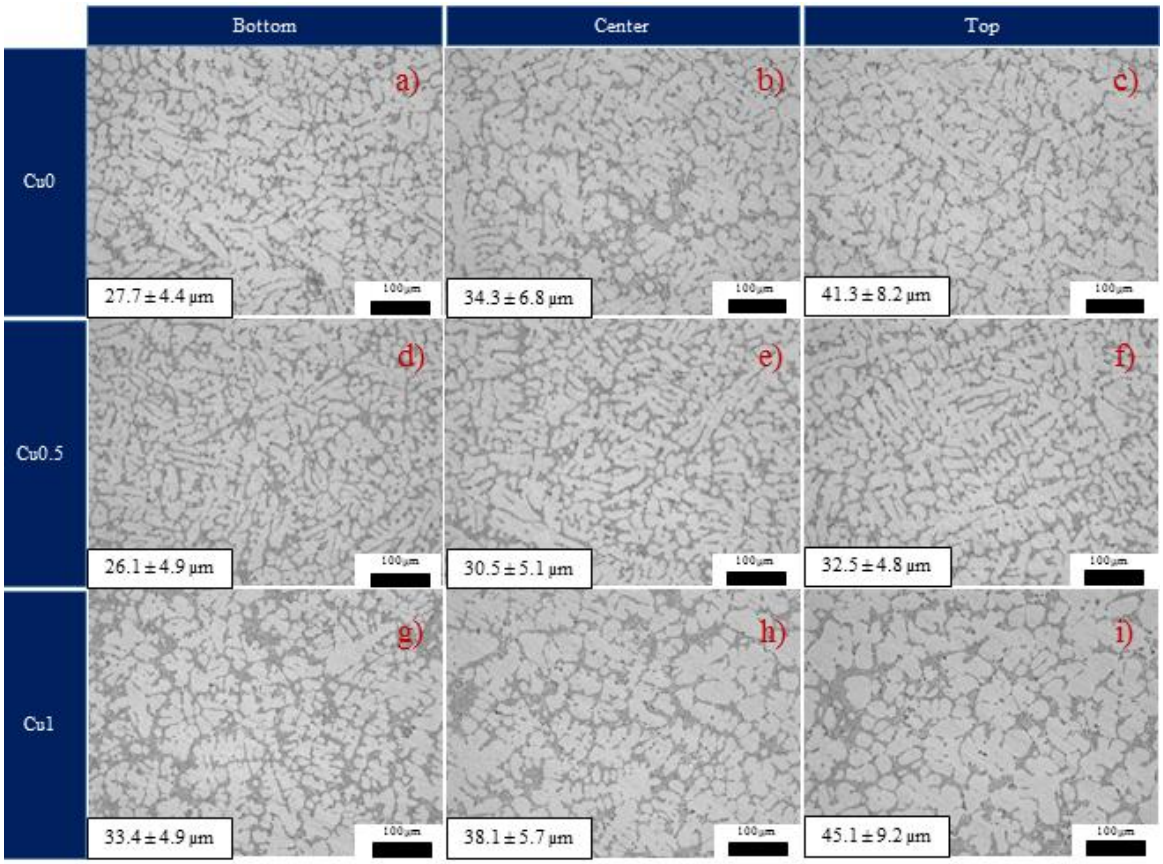

Fig. 3. Optical micrographs and SDAS measurements as function of Cu-content and specimen cutting position; (a)-(c) micrographs depict the microstructure of the Cu-free alloy; (d)-(f) of the 0.5% Cu alloy and (g)-(i) of the 1% Cu alloy with SDAS ranging from 30 up ~ 40 µm.

To further address the influences of both Cu contents and cooling rates on the alloy's mechanical response, hardness measurements were also conducted. Vickers micro hardness (HV) and Rockwell hardness (HRF) tests were performed over the bottom, center and top of the three alloys considered, and presented in Fig.4. HV and HRF measurements do not reveal a clear enhancement in hardness, moving from bottom to top, as expected with reference to the linear hardness-strength relationship reported by Tiryakioğlu [29] and the author [30], nor an enhancement has been measured at the bottom compared to the top, as expected from tensile flow curves (fig. 2b,d,f). Cu content, on the other hand, exerts a prominent influence in increasing the hardness response of this alloy from 60HV to 90HV in Cu0 and Cu1, respectively. At this point, tensile properties variance, resulting comparing

B and T sample (b, d, e and f, in Fig.2), has been interpreted trough SDAS measurements (Fig.3), and the 10 µm shift, albeit its impressive effect on a small scale (12 mm), seem not to be the sole cause behind the tensile behavior. Additionally, hardness measurements, did not confirm the tensile variation rather, indeed focusing on the HRF measures, it is possible to observe a slight increment in hardness, moving from the B to the T, in evident contrast to the tensile response evolution.

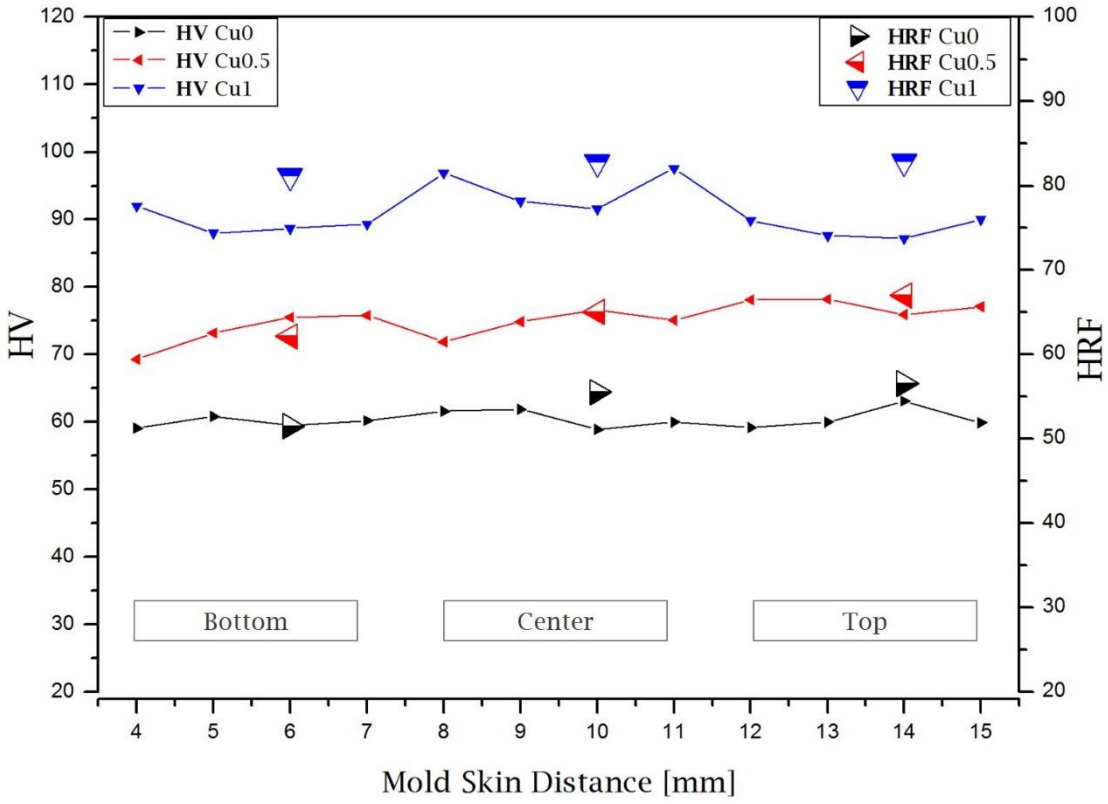

Fig. 4. Cast ingot hardness profile. Vickers Microhardness scale on the left, Rockwell Hardness scale on the right.

Microstructural Investigation

In order to deeply understand how the strength is correlated to the hardness, microstructural features have been investigated and in particular, eutectic Si particles equivalent diameter distribution and eutectic Si particles % area values have been presented in Fig. 5. The distribution histograms, obtained using chi-square goodness-of-fit test have been plotted for representative alloys which encompass reference (Cu0) and 1wt% Cu-containing (Cu1) alloys for the three bottom, center and top specimen cutting position. Cu0's equivalent

diameter (ED) distributions show a flatter tendency if compared to Cu1 cases. The shift observed in the eutectic nucleation temperature, assessing Cu0' and Cu1' $T_{N,eu}$ respectively to 578 °C and to 560 °C (Table 2), is believed to rule the eutectic Si particle size distribution. It is worth considered that Sr-modification strongly affects the eutectic Si particles dimension [31], and together with the Cu-content contributes to depress the eutectic reaction. Hence, the higher Sr-content of 75-80 ppm resulted after the casting in the Cu-containing alloys (Table 1) prevent us to address the decreasing eutectic Si particles size phenomenon, indicated by the distributions in Fig. 5, to the Cu addition.

On the other hand, frequency differences longitudinally across the different positions (a,b,c in Fig.5) highlight a feeble, though significant, lowering of the distribution histograms, suggesting an overall decrease in the eutectic Si particles ED size moving from the T to the B position. Focusing on the macro-scale (20x Leica DMi8 objective lens), eutectic Si particles surface area has been identified over the three interested zone: B, C, T. Measurements show eutectic Si particles surface area (A%) to be denser at the bottom as compared to the top, and in parallel show eutectic Si particles to be denser in the Cu-containing alloy.

Representative Backscattered electron (BSE) images and EDS spectra of the Cu-containing phases are presented in Fig. 6. Composition of the detected intermetallic phases as measured by semi-quantitative ESD are labelled in Table 3. For the sake of clarification, only the as cast Cu1 BSE micrographs are reported. Since heavy elements (high atomic number) backscatter electrons more strongly than light elements (low atomic number), and appear brighter in the image, BSE are used to detect contrast between areas with different chemical compositions. As a matter of fact, Cu-bearing phases appear in white and are found in different morphologies, resulting after Al-Si eutectic reaction. The θ-Al_2Cu phases, with the higher Cu content ~ 30 at. %, are presented in both blocky ('+4' in Fig. 6c '+6' in Fig. 6d) and eutectic shape (Fig. 6e). They are usually associated with β-Al_5FeSi plates or coarse eutectic Si particles, as result of the last stage of solidification. Others high-Cu-content particles have been identified as quaternary Q phases, $Al_5Mg_8Si_6Cu_2$. Because of the small size of the particles, it is not straight forward to determine by EDS the exact stoichiometry of Q phases. The results however were consistent with the most widely accepted composition [32-34]. Most of these phases are observed in form of isolated polygonal particles ('+5'in Fig. 6c) and the rest forming a fine rounded/ spherical ternary eutectic feature together with the θ phase ('+3'in Fig. 6b) as also reported by Han [35].

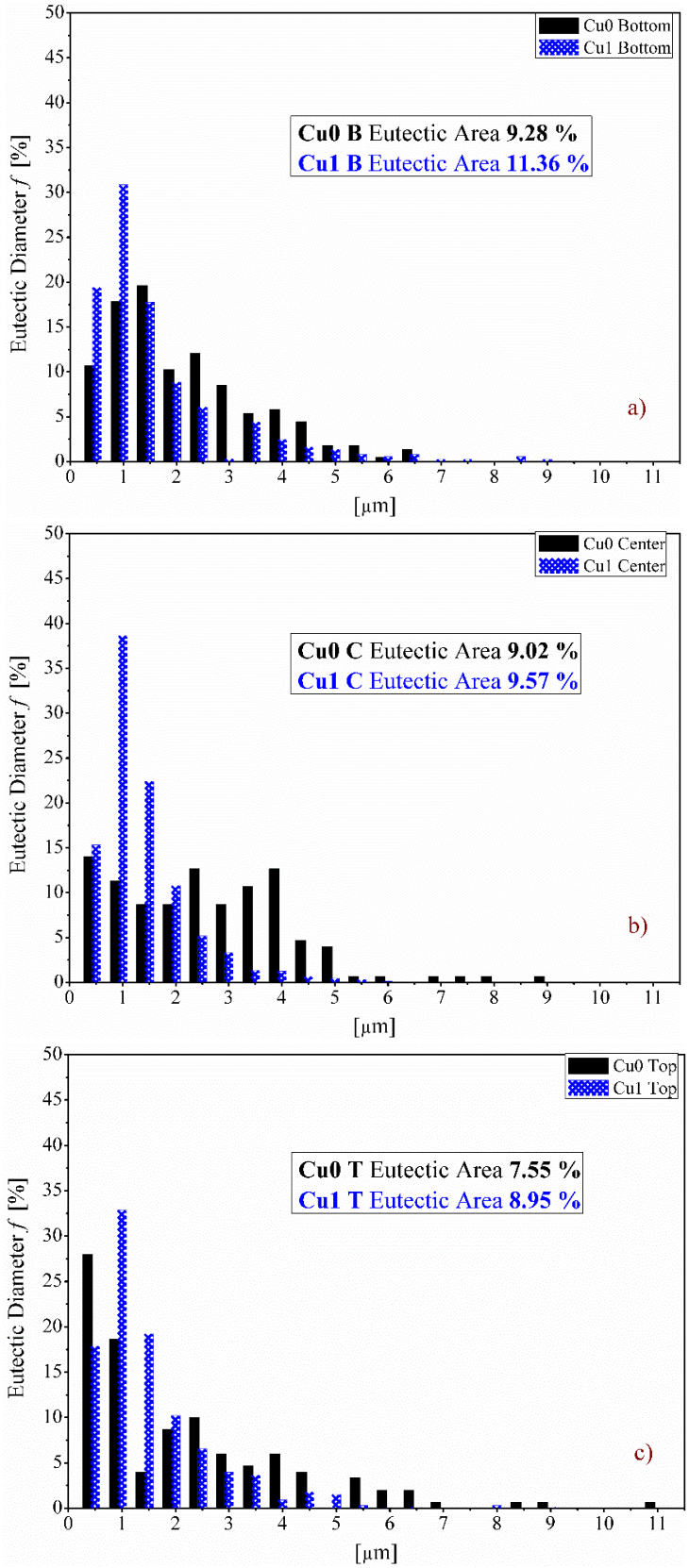

Fig. 5. Distribution of the Eutectic Si-Particles' equivalent diameter. Comparison between Cu-free and Cu-containing alloys (1 wt% Cu) in the three bottom (a), center (b) and specimen (c) cutting position.

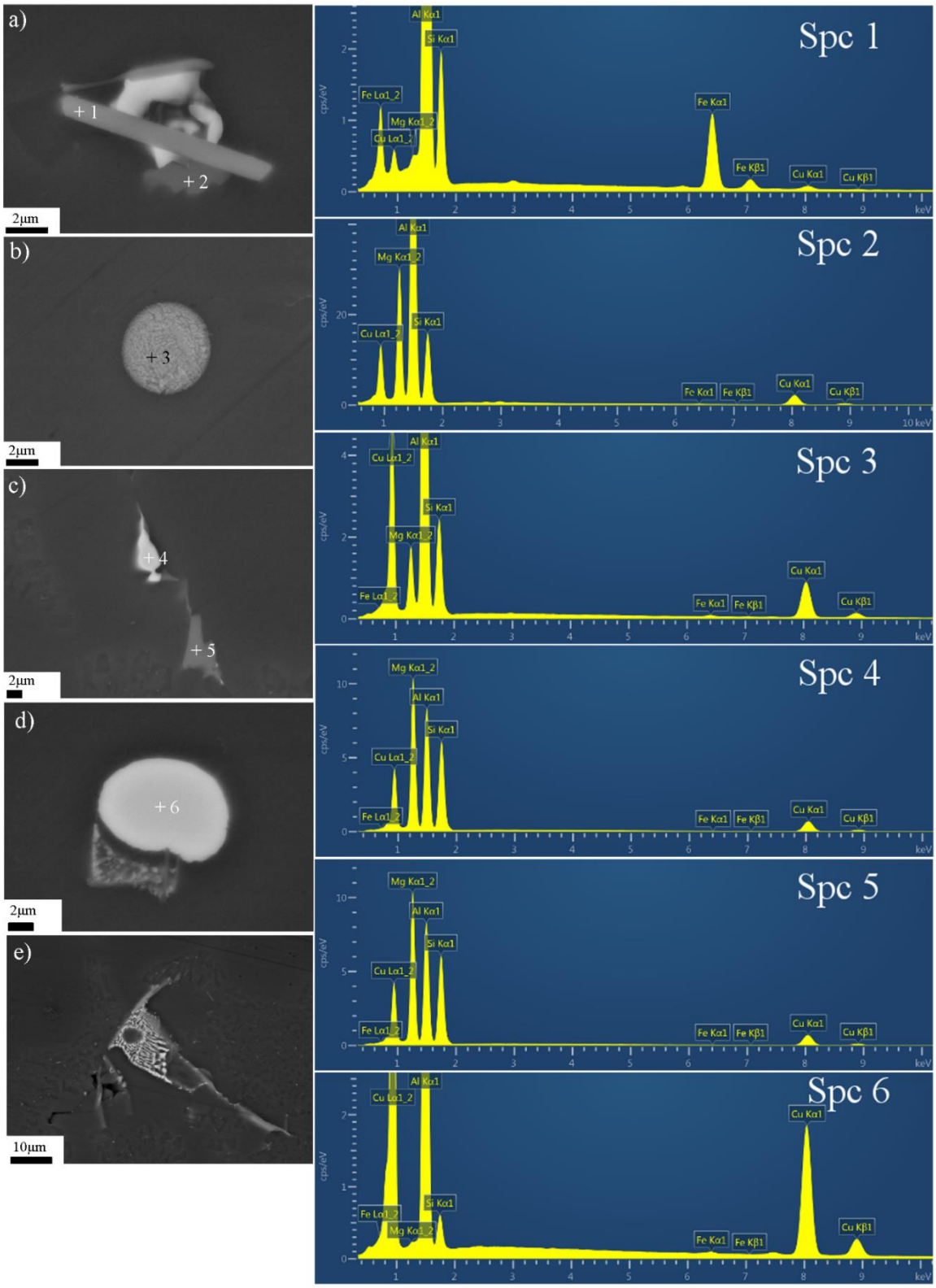

Fig.6. BSE images of some intermetallic phases detected in the Cu-containing alloy (Cu1), in the as cast condition. EDS measurements indicate the nature of the intermetallic compound as Al_2Cu, ß-Al_5FeSi and Cu/Mg bearing intermetallics.

In addition, light microscopy pictures of intermetallic phase distribution in the matrix are shown in Fig. 7. Macro overview of the Cu1 as cast microstructure is presented in Fig. 7 a. The rounded eutectic phases, indicated as Al-Q-θ, are found in the middle of the α-grains (Fig. 7b,c), whereas both eutectic and blocky forms of the Al_2Cu phases were observed in the interdendritic channels, or combined with the β -phase (Fig. 7c,d).

Table 3
Composition of the located intermetallic phases as measured by semi-quantitative EDS.

		Composition in (at. %)				
Spectrum	**Phase**	**Al**	**Si**	**Cu**	**Mg**	**Fe**
1	ß-Al_5FeSi	81.7	10.3	0.5	0.2	7.3
2	Q-$Al_5Mg_8Si_6Cu_2$	59.8	17.3	5.2	17.7	0.1
3	Al-Q- θ	67.5	14.2	11.5	6.5	0.3
4	θ-Al_2Cu	72.5	1.2	25.6	0.6	0.1
5	Q-$Al_5Mg_8Si_6Cu_2$	33.1	27.2	7.7	32	0.1
6	θ-Al_2Cu	67.5	3.8	28.3	0.2	0.2

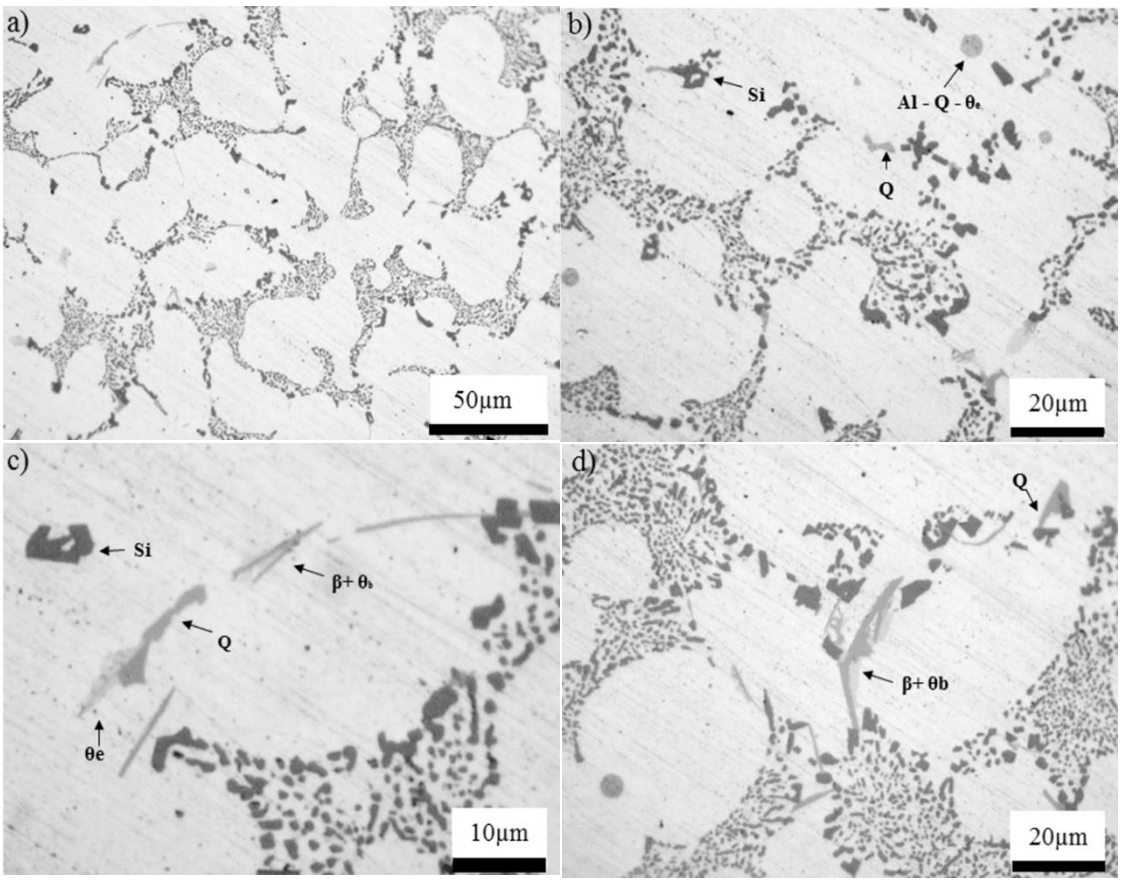

Fig.7 Optical micrographs of the Cu-Containing alloy (Cu1) where Fe-rich and Mg-/Cu-bearing phases are found as companion to the Si eutectic.

Electrical Conductivity measurements

Fig. 8 shows the electrical conductivity (EC) evolutions of the three alloys as a function of the specimen cutting position: bottom, center and top. Increasing the Cu content, it is expected a correspondingly electrical conductivity decrease as more solute atoms undergo to solid solution [36-39]. Cu0's EC response appears in contrast to the tendency predicted. The phenomenon could be addressed to the low Sr-content resulting after the casting (see Table 1). According to Mulazimoglu [40], the EC of Al-Mg-Si alloy is significantly affected by changes in morphology of the eutectic silicon; in particular, it has been found that the electrons flow more easily through ~~the~~ finer eutectic silicon in the modified alloy than in the coarse acicular silicon present in the unmodified alloys. Considering the global trend as a function of the mold skin distance, EC values (averaged over 8 measures) highlight a slight but significant decrease moving from bottom to top, revealing a higher content of solute atoms in the top α-matrix as compared with the bottom.

Assuming that the presence of eutectic Si particles is associated to the presence of Si-/Mg-/Cu- rich intermetallics, the higher is the Si eutectic content (see Fig.5) the higher is the intermetallics content. As a result, the bottom, richer of these Si-/Mg-/Cu- bearing compounds, achieved the highest tensile strengthening as compared to the center and top (see b, d, f in Fig.2). In parallel, α-Al matrix, impoverished by metastable solute Si, Mg and Cu atoms, showed in Fig.4 increasing hardness trends moving from bottom to top. The entire discussion is supported by EC results, that assessed higher content of solute metastable elements in the Top as compared to the Bottom.

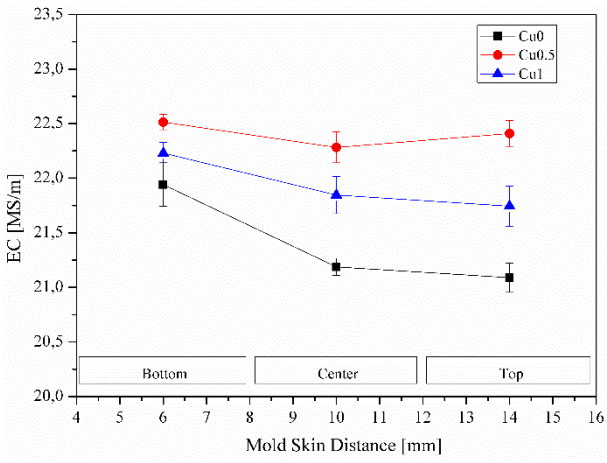

Fig.8 Cu0, Cu0.5 and Cu1 Electrical Conductivity measurements over the tree investigate positions: Bottom, Center and Top

Conclusions

In this work, 3 different sites within the cast plate, offering a narrow range of correspondent secondary dendrites arm spacing (SDAS) values, were compared. The investigation was performed on as-cast A356 alloy with and without copper (Cu) additions. Based on the results, the following conclusions can be summarized:

Stress-Strain curves clearly show improvement in strength with increasing Cu content, for the three B (bottom), C (center), and T (top) specimens, without significant reduction of elongation. In parallel, tensile curves also revealed how the specimen cutting position influences the mechanical properties leading to an enhancement in strength by approximately 10% and 20% for the Cu-free and the Cu-containing alloys, respectively, moving from the Top to the Bottom.

B, C and T`s SDAS values for the three Cu0 (Reference), Cu0.5 and Cu1 alloy variants range between 30, 35 and 40 μm, respectively. The 10 μm shift, albeit its impressive effect on a small scale (12 mm), seems not to be the sole cause behind the tensile behavior.

Cu content exerted a prominent influence in increasing the hardness response of this alloy. Hardness measurements did not confirm the tensile variation; rather it was possible to observe a slight increment in hardness, moving from the B to the T, which is in contrast with the material tensile response.

Frequency differences across the different positions did not indicate any specific trends, suggesting no correlation between the eutectic Si particle ED and the specimen cutting position and an overall decrease in the Si particle ED size moving from the top to the bottom position. Measurements also revealed Si particle surface area (A%) to be denser in the bottom samples compared to the top samples and, in parallel, showed Si particles to be denser in the Cu containing alloy.

θ-Al_2Cu phases are observed in both blocky and eutectic shape, usually associated with β-Al5FeSi plates or coarse eutectic Si particles, as result of the last stage of solidification. Others high Cu content particles have been identified as quaternary Q phases, $Al_5Mg_8Si_6Cu_2$. In addition, rounded eutectic phases, indicated as Al-Q-θ, are found along the interdendritic regions.

The bottom samples, richer in Si particles and Si-/Mg-/Cu-bearing compounds, offer the highest tensile strength and the lowest hardness. In line with these findings, electrical conductivity (EC) values decrease moving from the bottom to top position, indicating a

higher content of solute atoms in the α-matrix of the top samples as compared to the α-matrix of the bottom samples.

References

1. M. Di Sabatino, L. Arnberg, Castability of aluminium alloys, Trans. Indian Inst. Metals 62 (2009) 321-325.
2. S. Seifeddine, E. Sjölander, T. Bogdanoff, On the Role of Copper and Cooling Rates on the Microstructure, Defect Formations and Mechanical Properties of Al-Si-Mg Alloys, M.S.A. 4 (2013) 171-178, http://dx.doi.org/10.4236/msa.2013.43020
3. S.G. Shabestari, H. Moemeni, Effect of copper and solidification conditions on the microstructure and mechanical properties of Al-Si-Mg alloys, J. Mat. Pro. Tec. 153-154 (2004) 193-198, http://dx.doi: 10.1016/j.jmatprotec.2004.04.302
4. Q. G. Wang, C. H. Caceres, J. R. Griffiths, Damage by eutectic particle cracking in aluminum casting alloys A356/357, Metall. Mater. Trans. A 34(12) (2003) 2901-2912.
5. Fadavi, A. Boostani, S.Tamanthas, Fracture behavior of thixoformed A356 alloy produced by SIMA process, J. Alloys Compd. 481(1−2) (2009) 220-227.
6. C. Caceres, I. L. Svensson and J. Taylor, Strength-Ductility Behaviour of Al-Si-Cu-Mg Casting Alloys in T6 Temper, Int J. Cast Metal Res. 15(5) (2003) 531-543.
7. S. Seifeddine, I. L. Svensson, The Effect of Cooling Conditions and Variation of Alloying Elements on the Microstructural and Mechanical Properties of Al-7%Si Cast Alloys, Giessereiforschung 58(3) (2006) 50-54.
8. R. Farkoosh, M. Pekguleryuz, Enhanced mechanical properties of an Al–Si–Cu–Mg alloy at 300 °C: effects of Mg and the Q-precipitate phase, *Mater. Sci. Eng.* A *621* (*2015*) *277*-286.
9. A.R. Farkoosh, M. Javidani, M. Hoseini, D. Larouche, M. Pekguleryuz, Phase formation in as-solidified and heat-treated Al-Si-Cu-Mg-Ni alloys: Thermodynamic assessment and experimental investigation for alloy design, J. Alloys Compd. 551 (2013) 596-606.
10. J. Man, L. Jing, S. G. Jie, The effects of Cu addition on the microstructure and thermal stability of an Al-Mg-Si alloy, J. Alloys Compd. 437(2007) 146-150.

11. M. Murayama, K. Hono, M. Saga, M. Kikuchi, Atom probe studies on the early stages of precipitation in Al-Mg-Si alloys, Mater. Sci. Eng. A 250 (1998) 127-132.
12. L. Zhen, W. Fei, S. Kang, H. King, Precipitation behaviour of Al-Mg-Si alloys with high silicon content, J. Mater. Sci. 32 (7) (1997) 1895-1902.
13. W. F. Miao, D. E. Laughlin, Precipitation hardening in aluminum alloy 6022, Scr. Mater. 40 (7) (1999) 873-878.
14. D. G. Eskin, Decomposition of supersaturated solid solutions in Al-Cu-Mg-Si alloys, J. Mater. Sci. 38, (2003) 279-290.
15. S. K. Son, M. Takeda, M. Mitome, Y. Bando, T. Endo, Precipitation behavior of an Al-Cu alloy during isothermal aging at low temperatures, Mater. Lett. 59 (2005) 629-632.
16. S. C. Wang, M. J. Starink, N. Gao, Precipitation hardening in Al-Cu-Mg alloys revisited, Scr. Mater. 54 (2006) 287-291.
17. P. Ratchev, B. Verlinden, P. De Smet, P. Van Houtte, Effect of cooling rate and predeformation on the precipitation hardening of an Al-4.2wt%Mg-0.6wt%Cu alloy, Scr. Mater. 38(8) (1998) 1195-1201.
18. F. Feikus, Optimization of Al-Si cast alloys for cylinder head application, AFS Trans. 106 (1998) 225-223.
19. L. Heusler, F. J. Feikus, and M. O. Otte, Alloy and Casting Process Optimization for Engine Block Application, AFS Trans. 109 (2001) 215-223.
20. L. Dons, G. Heiberg, J. Voje, J. S. Maeland, J. O. Loland and A. Prestmo, On the Effect of Additions of Cu and Mg on the Ductility of AlSi Foundry Alloys Cast with a Cooling Rate of Approximately 3 K/s, Mat. Sci, Eng. A, 413 (2005) 561-566. http://dx.doi:10.1016/j.msea.2005.09.053
21. ISO 6507-1,2,3 (1997) Metallic materials -Vickers hardness test - Part 1: Test method, Part 2: Verification of testing machines, Part 3: Calibration of reference blocks.
22. ISO 6508-1,2,3:1999 Metallic materials -- Rockwell hardness test -- Part 1: Test method (scales A, B, C, D, E, F, G, H, K, N, T), Part 2: Verification and calibration of testing machines (scales A, B, C, D, E, F, G, H, K, N, T), Part 3: Calibration of reference blocks (scales A, B, C, D, E, F, G, H, K, N, T).
23. L. *Arnberg*, L. Bäckerud. *Solidification Characteristics of Aluminum Alloys*, Volume 3: Dendrite Coherency, Des Plaines, Illinois AFS, 1996.

24. L. Bäckerud, G. Chai and J. Tamminen, Solidification Characteristic of Aluminum Alloys, Volume 2: Foundry Alloys, AFS/SkanAluminium, Stockholm,1990.
25. *H.T. Lu, L.C. Wang, S.K. Kung, Grain Refining* in *A356 Alloys*, J. of *Chinese* Foundryman's *Association*, 29 (*1981*) *10-18.*
26. R. I. Mackay, J. E. Gruzleski, Quantification of magnesium in 356 alloy via thermal analysis, Int. J. Cast Metal Res., 10 (1998) 255-265. http://dx.doi.org/10.1080/13640461.1998.11819241
27. M. Zeren, E. Karakulak, S.Gümüş, Influence of Cu addition on microstructure and hardness of near-eutectic Al-Si-xCu-alloys, Trans. Nonferrous Mec. Soc. China 21 (2011) 1698-1702.
28. http://akademikpersonel.kocaeli.edu.tr/zeren/sci/zeren05.09.2011_12.01.38sci.pdf
29. S.A. Kori, M.S. Prabhudev and T.M. Chandrashekharaiah, Studies on the microstructure and mechanical properties of A356 alloy with minor additions of copper and magnesium, T. Indian I. Metals, 62 (4-5) (2009) 353-356.
30. M. Tiryakioğlu, J.S. Robinson, M.A. Salazar-Guapuriche, Y.Y. Zhao, P.D. Eason, Hardness–strength relationships in the aluminum alloy 7010, Mat. Sci. Eng. A 631 (2015) 196-200. http://pcwww.liv.ac.uk/~yyzhao/papers/2015_msea_al_alloy.pdf
31. M. T. Di Giovanni, E. Cerri, M. Merlin, D. Casari, L. Arnberg, G. L. Garagnani, Correlation between Aging Effects and High Temperature Mechanical Properties of the Unmodified A356 Foundry Aluminium Alloy, Mat. Sci. Forum, 879 (2017) 424-429. DOI: 10.4028/www.scientific.net/MSF.879.424
32. Q.G. Wang, Plastic deformation behavior of aluminum casting alloys A356/357, Metall. Mater. Trans. A, 34 (2003) 2707-2718.
33. L. Lasa, J. Rodrigues-Ibabe, Evolution of the main intermetallic phases in Al-Si-Cu-Mg casting alloys during solution treatment, J. Mater. Sci. 39(4) (2004) 1343-1355. DOI: 10.1023/B: JMSC.0000013895. 72084.c9
34. T. Lu, J. Wu, Y. Pan, S. Tao, Y. Chen, Optimizing the tensile properties of Al-11Si-0.3Mg alloys: Role of Cu addition, J. Alloys Compd. 631, (2015) 276-282.
35. L. Ceschini, A. Morri, S. Toschi, S. Johansson, S. Seifeddine, Microstructural and mechanical properties characterization of heat treated and overaged cast A354 alloy with various SDAS at room and elevated temperature, Mat. Sci. Eng. A, 648 (2015) 340-349. http://dx.doi.org/10.1016/j.msea.2015.09.072

36. Y.M. Han, A.M. Samuel, F.H. Samuel, H.W. Doty, Dissolution of Al2Cu phase in non-modified and Sr modified 319 type alloys, Int. J. Cast. Met. Res. 21 (2008) 387-393. http://dx.doi: 10.1179/136404608x347662
37. M. T. Di Giovanni, E. Cerri, T. Saito, S. Akhtar, P. Asholt, Y. Li, M. Di Sabatino, Effect of copper additions and heat treatment optimization of Al-7% Si aluminum alloy, La Metallurgia Italiana, 11 (2016) 43-47.
38. D.L. Zhang and L. Zheng, The quench sensitivity of cast Al-7 wt pct Si-0.4 wt pct Mg alloy, Metall. Mater. Trans. A., 27 (1996) 3983-3991.
39. *H.K. Kang, M. Kida, H. Miyahara,* Age hardening characteristics of Al-Si-Cu-Base cast alloys, *AFS* Trans., 107 (*1999) 507*-515.
40. S. Zafar, N. Ikram, M.A. Shaikh, K.A. Shoaib, Microstructure studies in *Al – 6%Si – 1.9%Cu – X%Mg alloys*, J.Mater.Sci., 25 (1990) 2595-2597.
41. M.H. Mulazimoglu, R.A.L. Drew, J.E. Gruzleski, The Electrical conductivity of cast Al-Si alloys in the range of 2~12.6 wt.% silicon, Metall. Mater. Trans. A, 20 (1996) 383-389.

Article 3

Influence of Cu addition on the heat treatment response of A356 foundry alloy

M.T. Di Giovanni, E. A. Mørtsell, T. Saito, S. Akhtar, M. Di Sabatino, Y.Li, E. Cerri.

submitted to Material Science and Engineering A.

Influence of Cu addition on the heat treatment response of A356 foundry alloy

Maria Teresa Di Giovanni[a*], Eva Anne Mørtsell[b], Takeshi Saito[c], Shahid Akhtar[c], Marisa Di Sabatino[b], Yanjun Li[b], Emanuela Cerri[a]

[a] Department of Industrial Engineering and Architecture, 43124 Parma, Italy
[b] Department of Materials Science and Engineering, Norwegian University of Science and Technology, 7491, Trondheim, Norway
[c] Hydro Aluminium, Research and Technology Development, N-6601 Sunndalsøra, Norway

ABSTRACT

High-temperature performance is a critical characteristic affecting Al-Si-Mg alloy's suitability for various power-train applications like combustion engine cylinder head components. In this framework, there is a growing interest toward the addition of Copper (Cu) to the traditional Al-Si-Mg alloys. If properly heat treated, the quaternary alloys exhibit higher mechanical properties as compared to the traditional ternary alloys, i.e. Al-Si-Mg and Al-Si-Cu. The concurrent presence of Cu and Mg should enable the precipitation of Cu containing metastable precipitates such as Q' or Θ', boosting the thermal stability of these T6 heat treated alloys. The influence of the aging parameters on the tensile response has been extensive on high Cu alloys (up to 5 wt. %), while few works were conducted on Al-Si-Cu-Mg alloys containing up to 1 wt. % Cu. In general, the tensile strength increase by the addition of Cu on the expense of ductility when the Cu content is higher than 0.5 wt.%. Therefore, it is important to optimize Cu content and heat treatment to maximize age hardenability and Cu contribution for desired properties in Al-Si-Mg-Cu alloys. In this study, two solutionizing temperatures and two artificial aging temperatures were tested in Al-Si-Mg alloys having 0 wt. %, 0.5 wt. %, and 1 wt. % Cu content. The precipitation behavior, as observed through the aging curves and TEM analysis, has been correlated with the tensile response.

Keywords: A356 alloy; Cu additions; Heat Treatment Optimization; TEM analysis

Introduction

Owing to their good strength, castability and corrosion properties, the Al-Si-Mg based foundry alloys are extensively used in the automotive industry. The strength to weight ratio is an advantage as lighter vehicles have better fuel efficiency and reduced emissions. However, high-temperature performance is a critical characteristic affecting alloy's suitability for various power-train applications like combustion engine cylinder head components. In this framework, there is a growing interest toward the addition of Copper (Cu) to the traditional Al-Si-Mg alloy. The presence of Cu enables the precipitation of Cu containing metastable precipitates such as Q' or Θ', boosting the thermal stability of these T6 heat treated Al-Si-Mg alloys [1]. If properly heat treated, the quaternary alloy exhibits higher mechanical properties as compared to the traditional ternary alloys, i.e. Al-Si-Mg and Al-Si-Cu [2]. The alloy strengthening is due to the formation of metastable precipitates attained under a three step heat-treatment encompassing: i. solutionizing, ii. quenching, and iii. aging. During solutionizing of Al-Si-Mg (-Cu) alloys, eutectic Si particles become spheroidized, some primary solidified phases are dissolved and consequently the alloying elements Mg and Cu (and Si) diffuse into solid solution. The spheroidization of eutectic particles is important to improve elongation of the material. The dissolution of primary phases and the diffusion of alloying elements enhance the strength through precipitation [3]. The maximum solutionizing temperature is restricted to the incipient melting of Cu-rich phases, which in turn depends on Mg/Cu ratio, and also on solidification rate [4]. The most relevant literature [5-7] suggests a solutionizing temperature varying from 495 °C to 520 °C for alloys with Cu content in the range 0.5 - 5 wt. %. As Cu has a lower diffusivity in solid solution than Mg and Si, [8], for low solutionizing temperature, not all the atoms will be available for precipitation hardening during aging, where high solutionizing temperature will lead to local melting of Cu rich phases. In light of this, optimization of solutionizing is necessary to improve the aging response of Al-Mg-Si alloys with Cu. During artificial aging, Cu additions change the precipitation sequence [9], number density of precipitates, and eventually contribution to strength. Some reports [10,11] show no difference in precipitation kinetics in the quaternary as compared to the ternary alloys, while extensive [12-16] investigations suggest the existence of different precipitates types after artificial aging. In this concern, despite it is not generally confirmed, double aging peaks have been sometimes observed in Al-Si-Cu-Mg alloys [10, 17]. The influence of the aging parameters on the tensile response has been extensively investigated on high Cu

alloys (up to 5 wt. %), while few works were conducted on Al-Si-Cu-Mg alloys containing up to 1 wt. % Cu. In general, the tensile strength increase by the addition of Cu on the expense of ductility when the Cu content is higher than 0.5 wt.% [10,18], though the underlying mechanisms were not clearly understood. Therefore, optimizing Cu content and heat treatment to maximize age hardenability and Cu contribution for the desired properties in Al-Si-Mg-Cu alloys is important. In this study, two solutionizing temperatures and two artificial aging temperatures are tested in Al-Si-Mg alloys having 0 wt. %, 0.5 wt. %, and 1 wt. % Cu content. Mechanical properties in connection with precipitation behavior during artificial aging were also investigated.

Materials and Methods

The material used in this study was a commercial A356 alloy, melted in a boron-nitride coated crucible at 750 °C and grain refined with Al-5Ti-1B. Cu was added to the melt to reach concentrations of 0.5 and 1 wt. %. Before being poured into a copper mold having the dimension 65x100x40 mm^3, the aluminum melts were degassed with argon for five minutes. The temperature of the mold was kept at 50 °C for all the casting trials. Further experimental details can be found in [3]. The chemical compositions of the alloys as measured by Optical Emission Spectroscopy (OES) are given in Table 1. For solutionizing the samples were heated from room temperature up to 500 °C and 530 °C with a heating rate of 250 °C/h. Aiming to obtain maximum Mg and Cu content in solid solution before aging and, concurrently, avoid 'incipient melting' of the intermetallic phases, different holding times were applied to the alloys, and are presented in Table 2. As the solutionizing was completed, the samples were directly quenched in water to room temperature. In order to obtain hardness curves, Vickers micro hardness measurements (HV) were performed for all the conditions shown in Table 2. The measurements were done with 500 g load, using a Leica VHNT micro hardness tester. Electrical conductivity (EC) was also measured using a Foerster Sigmatest 2.069. After the solutionizing had been optimized with respect to HV, samples were stored for 1 h at room temperature. The samples were subsequently subjected to aging at 155 °C and at 190 °C for 1, 2, 4, 6, 10 and 15 h (Table 2). The procedure described above was repeated in order to obtain Vickers hardness and the electrical conductivity evolution of the three alloys as a function of aging time for both aging temperatures. Finally, the mechanical properties of the test bars were examined after 5 h of SHT at 530 °C and after 2 h and 4 h of aging at 190 °C and 155 °C, respectively (under-

aged condition), and after 4 h and 10 h of aging, at 190 °C and 155 °C, respectively (peak-aged condition). Tensile tests were conducted at room temperature, using an MTS 810 Universal Testing Machine. The crosshead speed during tensile test was 1 mm/min. For each condition, 3 parallel specimens with a gauge length of 7 mm and a cross section of 4 mm x 4 mm, were tested.

Table 1. Chemical composition (wt.%) of the A356 reference alloy and the Cu-containing alloys as measured by OES and their classification.

Alloy	**Si**	**Mg**	**Fe**	**Cu**	**Ti**	**B**	**Sr**	**Al**	**Code**
A356 (Reference)	6.624	0.216	0.086	0.006	0.103	4.6 ppm	14 ppm	bal.	**Cu0**
A356 + 0.5 wt.% Cu	6.587	0.258	0.082	0.454	0.105	5.6 ppm	80.8 ppm	bal.	**Cu0.5**
A356 + 1 wt.% Cu	6.915	0.262	0.091	0.983	0.086	5.6 ppm	74.5 ppm	bal.	**Cu1**

Table 2. Heat Treatment time/temperature parameters.

Solutionizing													
T = 500°C T = 530°C	0h	1h	2h	3h	4h	5h	6h	7h	8h	9h	10h	11h	12h
Aging													
T = 155°C T = 190°C	0h	1h		2h		4h		6h		10h		15h	

TEM samples were prepared after artificial aging at 155 °C for 10 hours. Slices were cut from the undeformed grip-area of the tensile specimens, perpendicular to the elongation direction. The slices were polished with SiC-paper up to #2500 grit until a thickness of about 100 μm was reached. Disks of 3 mm diameters were then cut from the foils. The disks were electropolished using a twin-jet TenuPol-5 from Struers, with an electrolyte consisting of 1/3nitric acid and 2/3 methanol. The electrolyte was cooled to - 28 °C by adding liquid nitrogen. The TEM-samples were further ion-milled in a PIPSII, using Ar-ions, at angles of +/- 4°. A JEOL2100 and JEOL2100F, both operated at 200 kV, were used for bright field (BF) TEM-imaging and high resolution (HR)-TEM, respectively.

Results and Discussion

Heat Treatment Optimization

Fig. 1 shows the evolution of Vickers hardness and EC as a function of time during solutionizing at 500 °C (a, b), at 530 °C (c, d) and during aging at 155 °C (e, f) and at 190 °C (g, h). Taking into account the solution heat treatment, the trends in the hardness curves at 500°C and 530°C can be considered similar (a and c in Fig.1). Increasing the Cu content, as described by [19-21], results in an increase in hardness and a corresponding decrease in electrical conductivity. This effect is attributed to more solute atoms in solid solution during solutionizing. Both the hardness curves at 500 °C and 530 °C reflect the coexistence of two competing phenomena: on one side the spheroidization and coarsening of the Si-eutectic responsible for the initial decay in hardness, and on the other hand, the dissolution of the primary solidified phases present in the as cast microstructure. Both phenomena are promoted by the solutionizing at high temperature. In addition, the number of quenched-in vacancies rises with increasing the solutionizing temperature, which in turn can improve further artificial aging response. As expected, higher solutionizing temperature results in an overall increase in hardness, as the ability of the α-Al matrix to host Mg appears to be greatly improved when increasing the solutionizing temperature.

EC curves of the samples solutionized at 530 °C (d in Fig.1) show lower conductivity compared to the samples solutionized at 500 °C (b in Fig.1), inferring the presence of more dissolved atoms in solid solution, which has also been confirmed by the hardness response. The conductivity is observed to increase with increasing SHT time due to the spheroidization of eutectic Si, while it decreases due to the dissolution of primary phases. However, in analogy with the study proposed by Mulazimoglu [22], the electrical conductivity of Al-Mg-Si alloy is significantly influenced by changes in the eutectic silicon morphology during solutionizing. With the aim to achieve maximum dissolution of the strengthening elements in the Al matrix (Mg, Si and Cu) and a higher number density of quenched-in vacancies, the temperature of 530 °C has been selected for the solutionizing for further investigations of artificial aging response. It is important to note that no incipient melting of primary solidified phases was observed for the solutionizing at 530 °C. In this condition, the curves (c, d) start to stabilize after 5 h, suggesting a good combination between the dissolution of the hardening solutes and the spheroidization and coarsening of the Si-eutectics. Therefore, 5 h exposure at 530 °C has been selected as the optimized solutionizing for the alloys and conditions considered in this study.

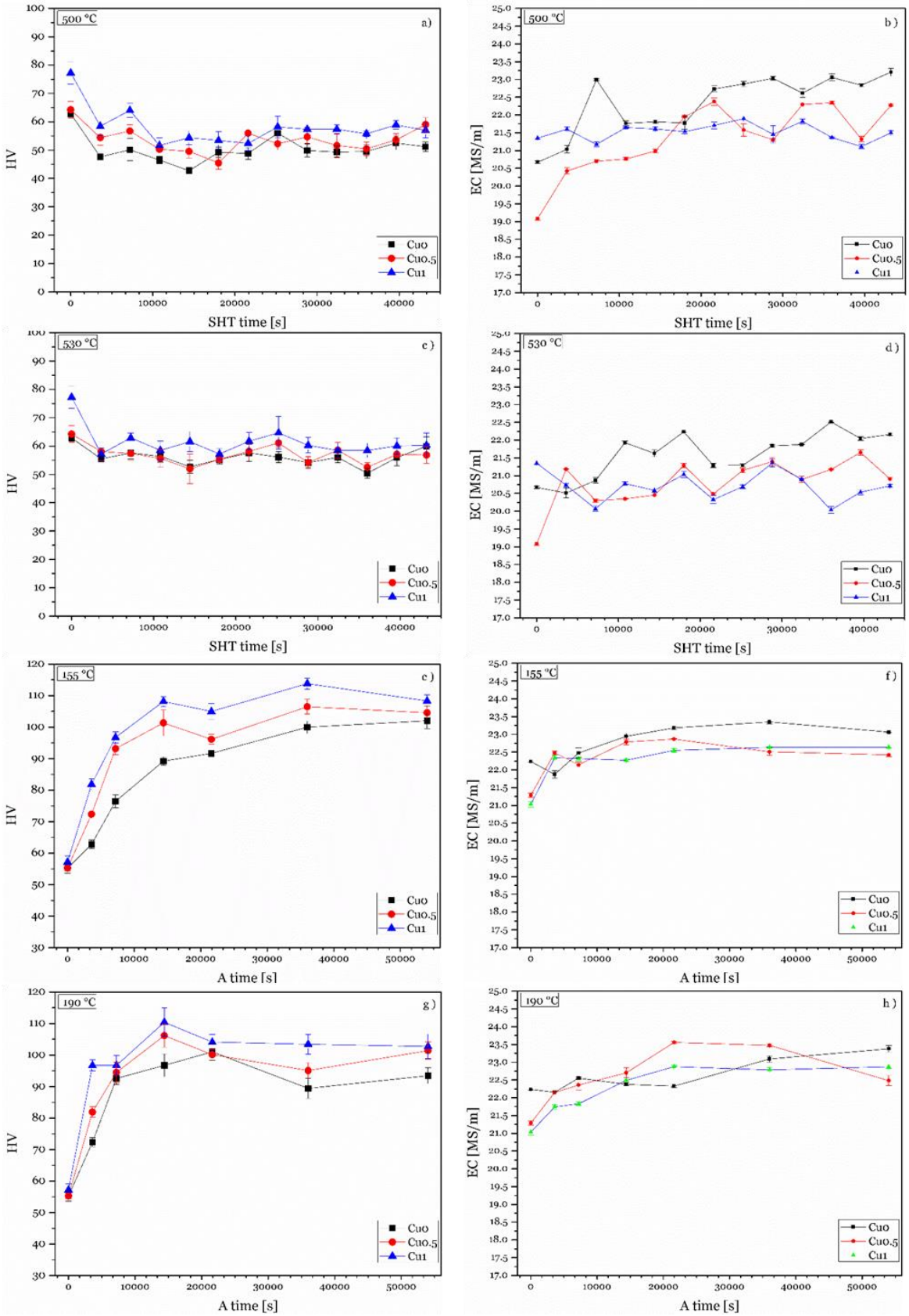

Fig.1. Evolution of Vickers hardness and electrical conductivity as a function of time during solutionizing at 500°C (a, b), at 530°C (c, d) and during aging at 155°C (e, f) and at 190°C (g, h).

The curves (e, g) and (f, h) in Fig.1 show the variation in hardness and EC with aging time for the alloys at the respective temperatures of 155°C and 190°C. It is worth clarifying that the Vickers hardness and EC values reported at the corresponding time of '0 s' represent the optimized values obtained after solutionizing at 530 °C for 5 h followed by quenching. Three main observations can be made: 1) there is an obvious age-hardening response for all three alloys at both artificial aging temperatures, and this is in good agreement with several studies [19,20,23,24], 2) higher maximum hardness is reached in the Cu-containing alloys, 3) two distinct stages of precipitation hardening are observed in the Cu-containing alloys. At the early stage of aging, the hardness of the Cu containing alloys increases with aging time until it reaches the first peak after 4 h at 155 °C and after 2 h at 190 °C. At the intermediate stage of aging, after a small decrease, the hardness increases again and reaches the second peak after 10 h at 155 °C and after 4 h at 190 °C. Similar hardening responses during aging of Al-Si-Mg-Cu alloys have been reported in literature [10,25,26].

After 15 h the hardness of the alloys decreases as a result of over-aging in the Cu containing alloys (e in Fig.1), while the Cu-free alloy still has an increasing hardening tendency with aging time, leading to the highest hardness value after 15 h. This is in good agreement with the hypothesis of different precipitate types having different precipitation kinetics, which will be discussed in section 3.3. Also, it is possible to presume that the transformation of fine semi-coherent to coarse less coherent, and eventually incoherent precipitates lead to a loss of solute in the matrix [27,28]. Hence, with the exception of the Cu0 sample aged at 190°C, whose conductivity reflects the hardness peak, the factors mentioned above should contribute to an increased conductivity as a function of the artificial aging time.

When it comes to the Cu containing alloys, it should be noted that, in contrast to what was observed in the Cu0 alloy, in the first hardness evolution, accelerated precipitation kinetic enables the precipitation and growth of the semi-coherent precipitates to commence earlier, and as a result, the conductivity increases with increasing aging time. Although the deviation in the curves is mainly attributed to the technique sensitivity, it is important to notice the uncharacteristic behavior of the Cu0.5 alloys, which offer the lowest conductivity values at the longest aging time.

Based on above-mentioned results, the under aged and the peak aged conditions have been chosen for tensile testing, i.e. 4 h and 10 h at 155 °C, and 2 h and 4 h at 190 °C.

Tensile Response

Fig. 2 presents the average values of the tensile properties of the reference and Cu-containing alloys. Fig. 2-a reports the as cast (AC) case as reference, while the under aged (UA) and the peak aged (PA) conditions are presented in Fig. 2-b,c for T=155 °C , and in Fig. 2-d,e for T=190 ° C.

The current study reveals that adding 0.5 wt.% and 1 wt.% of Cu does not turn into a proportional increment on the tensile response, as the improvement in strength in the Cu1 variant is much more pronounced, as compared to the Cu0.5 case. This might be attributed to the different precipitation kinetic, density and types of precipitate formed as discussed earlier. These are influenced by the Mg/Cu ratio. For example, Seifeddine et al. [29] reported that the more Cu is added, less Mg is held in the Al matrix, which indicates that also Mg-rich phases are favorable to form and might act as a reinforcement [3].

In agreement with the hardening response, the PA samples at 155 °C show a significant enhancement of both yield strength and ultimate strength as compared to the UA samples. While subjected to the aging temperature of 190 °C, there is no improvement in yield strength moving from the UA to the PA condition, and indeed the PA alloys exhibit a lower ultimate strength as compared to the UA case.

Comparing the Cu-free alloy to the Cu-containing alloys in Fig. 2, it is evident that the elongation is affected. By analogy with the strength response, the elongation of the investigated alloys does not linearly decrease with increasing Cu content. Although it is not straightforward to compare elongation behavior between different studies having different casting conditions, results show some dissimilarities with previous findings [10,18] which assessed Cu content increment to a correspondent elongation decreasing. It can be concluded that optimizing the solutionizing and the aging treatment results in higher tensile strength as compared to the prevailing literature [29,30]. In addition, the heat treatment optimization was found to be reflected in a significant increase in elongation with respect to commercial foundry alloys.

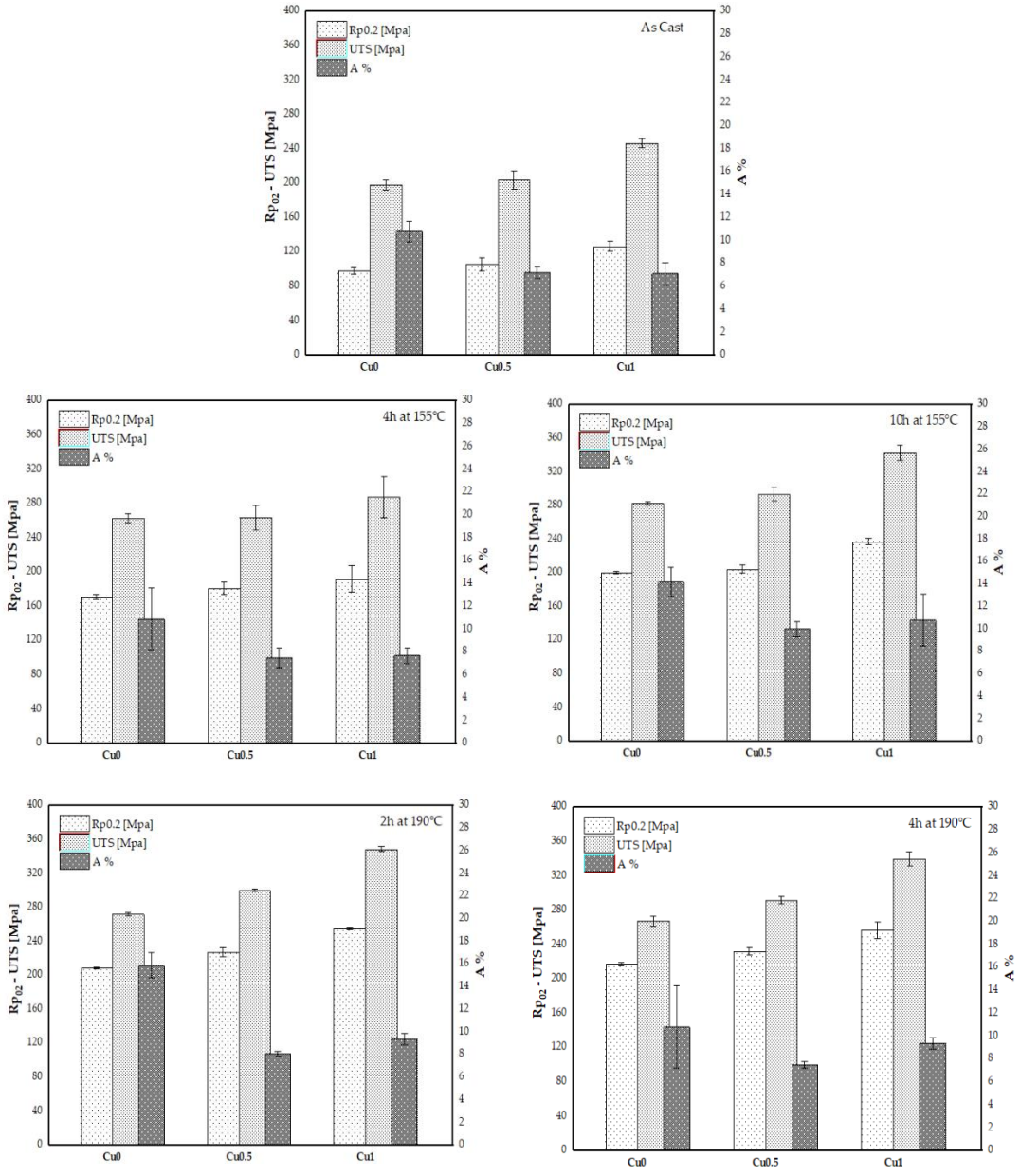

Fig.2. Tensile properties of the three investigated alloys in (a) as cast condition, solutionized for 5 h at 530 °C and successively aged (b) for 4 h at 155 °C, (c) for 10 h at 155 °C, (d) for 2 h at 190 °C, (e) for 4 h at 190 °C.

TEM Analysis

Transmission electron microscopy (TEM) investigations were done on each of the three alloys after aging for 10 h at 155 °C. An overview of the observed microstructure is given in Fig. 3, illustrating representative observations at different length scales in alloy Cu0.5.

The eutectic Si particles are present in all three alloys (see Fig. 3-a) and energy dispersive X-ray spectroscopy (EDS) confirmed this phase to consist of >99 wt.% Si. The Si-eutectic phases are, however, too large to be further investigated by TEM, as their thicknesses are typically much larger than the mean free path in Si at 200 kV. Smaller precipitates, ranging from about 100 nm to 1 μm in length, can be observed in Figure 3-b, these precipitates have been assumed to consist mainly of Si [31]. Si-precipitation have previously been connected to excess-Si in 6xxx alloys by Gupta et al. [31], the Si-precipitates' effect were, however, deemed insignificant on material hardening.

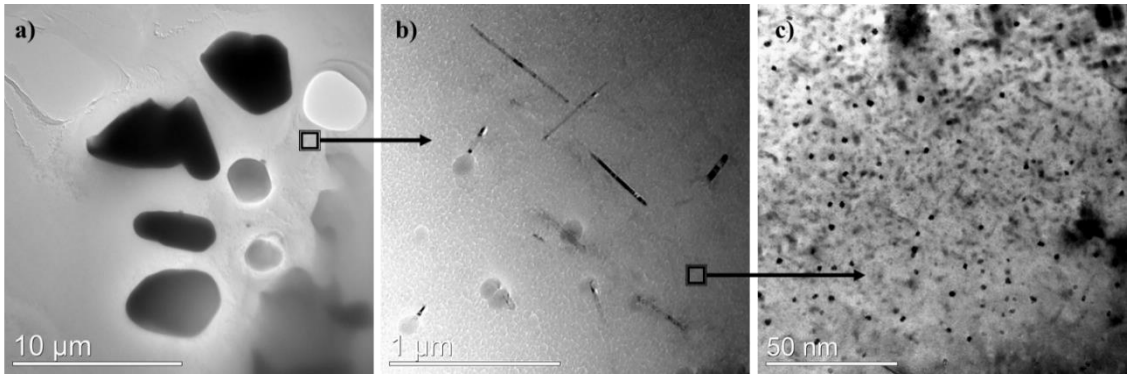

Fig. 3. BF-TEM micrographs from 0.5Cu aged for 10 hours at 155°C. a) Si-eutectic (large dark features), b) Si-precipitates [31] and c) Meta-stable precipitate needles growing along the three $<001>_{Al}$ directions. The dark dots are cross sections growing into the image-plane. The squares in a) and b) indicate the imaged areas in b) and c) respectively.

In the Al-Si-Mg(-Cu) system, several metastable precipitates are encountered growing along $<001>_{Al}$ in α-aluminium, see Figure 3-c and Figure 4. The metastable precipitates are assumedly analogue to the ones encountered in 6xxx series (i.e. Al-Mg-Si) aluminium alloys, i.e. Mg and Si (and Cu) in α-aluminium solid solution for formation of the precipitates during artificial aging. The precipitation sequence in 6xxx series aluminium alloys is generally accepted as β" and post β" phases in Cu free alloys, and L, C and Q' phases in addition to β" and β' in Cu containing alloys [32]. Based on TEM studies, the main precipitates observed in this study were needles along <001>Al. β" in Cu0 and β", Q' and C phases in Cu0.5 and Cu1, see Fig. 5. The observed double peak in hardness evolution

from Fig.1 in the two Cu-containing alloys is probably due to the formation of the Cu containing metastable precipitates, C and Q', which have different precipitation kinetics than β". As demonstrated earlier [10], the θ' phase exists in 3 wt.% Cu containing AlSi7Mg0.5 alloys, where it was also suggested that Cu contents exceeding 1 wt.% are crucial to nucleate and grow the θ' phase in Al-Si-Mg-Cu alloys. No significant occurrence of θ' was observed in this study, in good agreement with this hypothesis.

When comparing the precipitation in the three alloys, see Fig. 4, it becomes clear that the needle-lengths decrease significantly with increasing Cu addition. The measured needle lengths decrease from about 25 nm in Cu0 to less than 7 nm in Cu1, see Table 3. Such decrements in precipitate lengths generally comes with a corresponding increase in precipitate number density. By refining the precipitates, an increase in UTS and HV occurs for increasing Cu-additions, due to a higher dislocation impediment potential.

Table 3. Average precipitate needle lengths for the three alloys after 10 hours aging at 155 °C.

Alloy	Needle length [nm]
Cu0	25.0 ± 2.0
Cu0.5	8.1 ± 0.4
Cu1	6.8 ± 0.4

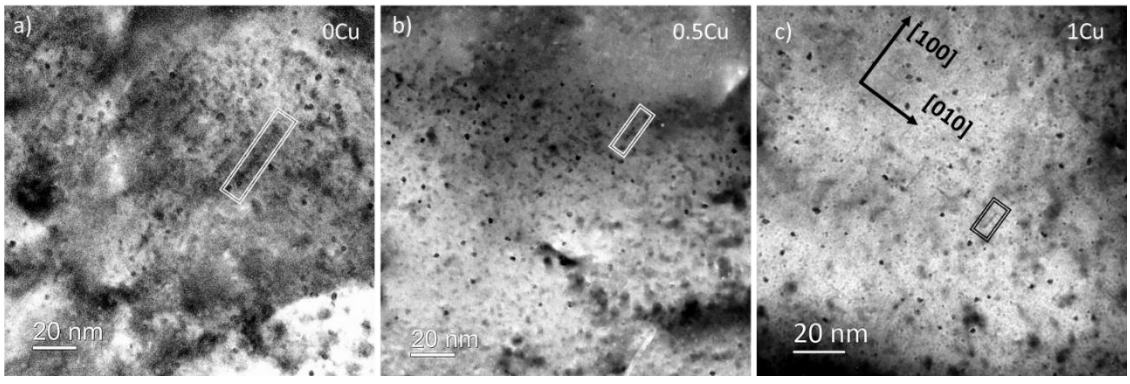

Fig. 4 BF-TEM micrographs illustrating the precipitate needles in a) Cu0, b) Cu0.5 and c) Cu1. The three alloys have been aged for 10 h at 155 °C.

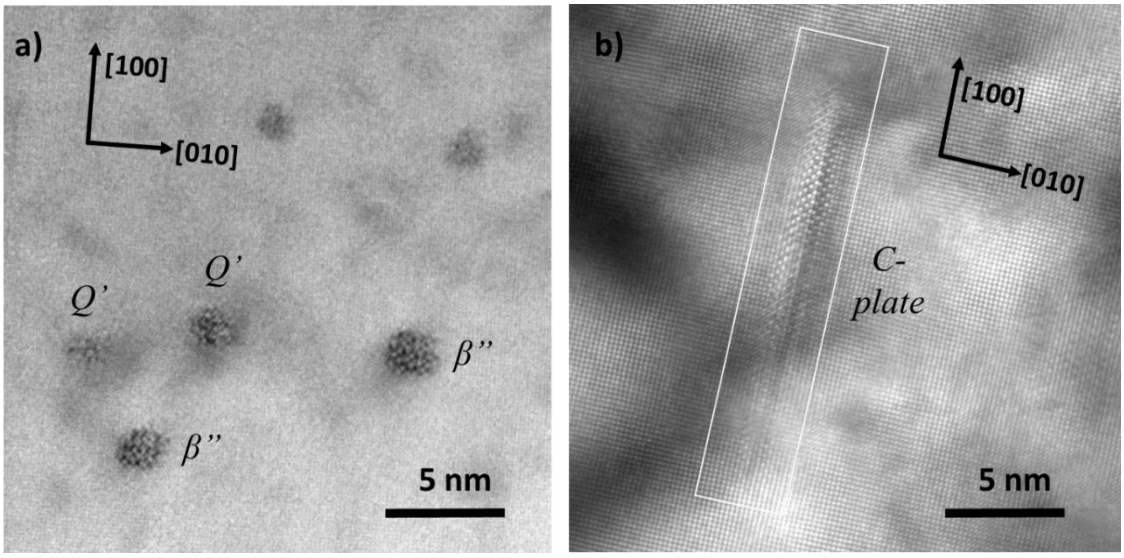

Fig.5. HR-TEM micrographs from alloy Cu0.5 illustrating typical cross sections identified in the three alloys after 10 hours aging at 155 °C. a) Q' and β'' cross sections. β'' is most common in Cu0, while a transformation towards Q' and C occurs in Cu0.5 and Cu1. b) C-plate cross section in Cu0.5. This phase seems to occur with a higher frequency in alloy Cu1 than in Cu0.5.

Conclusions

In this study, two solutionizing temperatures (500 °C and 530 °C) and two aging temperatures (155 °C and 190 °C) were tested in Al-Si-Mg alloys having 0 wt.%, 0.5 wt.%, and 1 wt.% Cu content. Mechanical properties in connection with precipitation behavior during artificial aging were investigated, to validate the selected optimized heat treatment parameters. The following conclusions can be drawn from this study:

Aiming to achieve maximum dissolution of the strengthening elements in the Al matrix and to avoid incipient melting of Cu-rich phases, the temperature of 530 °C and an exposure of 5 h have been selected as the optimized solutionizing parameters.

An obvious age-hardening response was found at both artificial aging temperatures; higher maximum hardness is reached in the Cu-containing alloys. Double aging peaks have been observed in the Cu-containing alloys, while the Cu-free alloy has an increasing hardness tendency with aging time. Under aged (4 h at 155 °C and 2 h at 190 °C) and peak aged (10 h at 155 °C and 4 h at 190 °C) have been chosen for the tensile testing.

Adding 0.5 wt.% and 1 wt.% of Cu does not turn into a proportional strength of the tensile response, as the improvement is strength in the Cu1 variant is much more pronounced compared to the Cu0.5 case. This might be attributed to the different precipitation kinetic, density and types of precipitate formed.

Optimizing the SHT results in higher strength and elongation as compared to the commercial A356 Aluminum foundry alloys.

When comparing the precipitation in the three alloys, it becomes clear that the needle-lengths decrease significantly with increasing Cu addition. The measured needle lengths decrease from about 25 nm in Cu0 to less than 7 nm in Cu1. Refining the precipitates, result in increase in UTS and HV for higher Cu-additions, due to a higher dislocation density and impediment potential.

Reference

1. J. Man, L. Jing, S. G. Jie, J. Alloys Compd. 2007, 437, 146

2. S. Toschi, Cast Aluminum Alloys and Al-Based Nanocomposites with Enhanced Mechanical Properties at Room and High Temperature: Production and Characterization, PhD thesis. DOI10.6092/unibo/amsdottorato/7495.

3. M.T. Di Giovanni, E. Cerri, T. Saito, S. Akhtar, P. Asholt, Y. Li, M. Di Sabatino, Adv. Mat. Sci. and Eng., 11, 2018. https://doi.org/10.1155/2018/4030689.

4. M. Javidani, D. Larouche, X. G. Chen. Met.Mat. Trans. A, 2016, 47A, 4818

5. J. H. Sandoval, A. M. Mohamed, S. Valtierra, F. H. Samuel, Mater. Sci. Forum 2014, 794-796,489.

6. A. Mohamed, F. H. Samuel, S. Al Kahtani, Mater. Sci. Eng. A 2013, 577, 64.

7. P. Wang, S. Lee, J. Lin, J. Mater. Res. 2000, 15, 2027.

8. Y. Du, Y.A. Chang, B. Huang, W. Gong, Z. Jin, H. Xu, Z. Yuan, Y. Liu, Y. He, F.Y. Xie, Mater. Sci. Eng A 2003, 363, 140. https://doi.org/10.1016/S0921-5093(03)00624-5

9. A.R. Farkoosh, M. Pekguleryuz Mater. Sci. Eng. A 2015,621, 277-286

10. Y. J. Li, S. Brusethaug, A. Olsen, Scr. Mater. 2006, 54, 99

11. W. Reif, J. Dutkievicz, R. Ciach, S. Yu, J. Krol, Mater. Sci. Eng. A 1997, 234-236, 165.

12. D. G. Eskin, J. Mater. Sci. 2003, 38, 279.

13. S. C. Wang, M. J. Starink, N. Gao, Scr. Mater. 2006, 54, 287.

14. P. Ratchev, B. Verlinden, P. De Smet, P. Van Houtte, Scr. Mater. 1998, 38, 1195.

15. D. Chakrabarti, D. E. Laughlin, Prog. Mater. Sci. 2004, 49, 389.

16. C. Cayron, P. a. Buffat, Acta Mater. 2000, 48, 2639

17. R. Li, R. Li, Y. Zhao, L. He, C. Li, H. Guan, Z. Hu, Mater. Lett. 2004, 58, 2096

18. S. Seifeddine, G. Timelli, I. L. Svensson, 2007, 59, 2.

19. D.L.Zhang and L. Zheng, Metall. Mater. Trans. A. 27A (1996), P. 3983.

20. H.K. Kang, M. Kida, H. Miyahara, Afs Trans. 27 (1999), P 507.

22. M.H. Mulazimoglu, R.A.L. Drew AND J.E. Gruzleski, Metall. Mater. Trans. A. 20A (1996), p 383.

23. S. Shivkumar, C. Keller, D. Apelian, AFS Trans 179 (1990) 905.

24. S. Zafar, N. Ikram, M.A. Shaikh, K.A. Shoaib, J. Mater. Sci. 25 (1990) 259.

25. Ibrahim, M.F., Samuel, A.M., Doty, H.W. et al. Inter Metalcast (2017) 11: 274. https://doi.org/10.1007/s40962-016-0057-z

26. Z. Li, A.M. Samuel, F.H. Samuel, C. Ravindran, S. Valtierra, H.W. Doty, Factors affecting dissolution of Al2Cu phase in 319 alloys. AFS Trans. 111, 1–14 (2003)

27. T. Ram Prabhu Engineering Science and Technology, an International Journal, ISSN: 2215-0986, Vol: 20, Issue: 1, Page: 133-142.2017

28. A.M.F. Muggerud, E.A. Mortsell, Y.J. Li and R. Holmestad, Mater. Sci. Eng. A 567, (2013), p. 2.

29. S. Seifeddine, E. Sjölander, T. Bogdanoff, Materials Sciences and Applications Vol. 4 No. 3 (2013) , Article ID: 29521 , 8 pagesDOI:10.4236/msa.2013.43020

30. S.A.Kori, M.S. Prabhudev, T.M. Chandrashekharaiah. Trans. IIM Vol. 62, 4-5, 2009

31. A.K. Gupta, D.J. Lloyd, S.A. Court, Mat. Sci. Eng. A. 316 (2001), pp. 11 – 17.

32. T. Saito, E.A. Mørtsell, S. Wenner, C.D. Marioara, S.J. Andersen, J. Friis, K. Matsuda, R. Holmestad, Advanced Engineering Materials, (2018).

Article 4

Influence of microstructure and porosity on the fracture toughness of Al-Si-Mg alloy

M.T. Di Giovanni, J. T.O. de Menezes, E. Cerri, E. M. Castrodeza

submitted to Journal of Material Research and Technology

Influence of microstructure and porosity on the fracture toughness of Al-Si-Mg alloy

Maria Teresa Di Giovanni*[a], Joao T. O. de Menezes[b], Emanuela Cerri[a], Enrique M. Castrodeza[c]

[a]Department of Engineering and Architecture, University of Parma, Parco Area Delle Scienze 181/A, 43124 Parma, Italy.

[b]Department of Metallurgical and Materials Engineering, COPPE/Federal University of Rio de Janeiro, Rio de Janeiro, 21941-972 Rio de Janeiro, Brazil.

[c]Department of Mechanical Engineering, Polytechnic of Milan, Via La Massa 1, 20156 Milano, Italy.

ABSTRACT

With improving molten metal quality and foundry technology, cast alloys are expected to be used more commonly in critical applications. The demands for improved damage tolerance of cast aluminum alloys have increased the importance of fracture-related properties. In this perspective, the present study aims to evaluate the effect of four different aging treatments on fracture toughness of a die cast A356 Al alloy with and without Cu addition. Crack growth resistance curves (*J*-R curves) were experimentally evaluated using the ASTM E1820-17 standard procedure on 25 mm thick compact tension C(T) specimens. In order to assess the mutual influence of casting defects and alloys hardness, as resulting after aging treatments, hardness results have been composed together with porosity values, and finally integrated with the J_{IC} values. In addition, microstructural observations were carried out to endorse the fracture mechanism.

1. Introduction

The past two decades have been marked by great progress and innovation in the aluminum foundry industry. However, the low ductility and fracture toughness, as compared to the wrought aluminum alloys counterpart, still represent one of the major impediment for increased use of aluminum casting aerospace industry [9]. Increasing efforts to improve both the melt quality and process condition 1 are being made, and as a result, Al-Si alloys are expected to be used more commonly in critical application areas. So far, the lack of knowledge towards the fracture toughness of these alloys had limited their use to field where fracture toughness related properties were not relevant. Though, fracture toughness evaluation in Al-Si alloys might represent a key step to understand the metallurgical features which control the toughness and hence will might allow proper material specifications to be settled for those applications where toughness-related failure must be prevented. In this concern, previous studies [4] reported the fracture toughness of a series of Al-Si castings and defined a ratio (λ / DE_{Si}) where λ is the silicon particle spacing and DE_{Si} is the equivalent silicon particle diameter. Tirakiyoglu [3] examined the fracture toughness potential of cast Al-7%Si-Mg alloys as a function of yield strength value. Tohgo and Oka [17] focused on the influence of coarsening treatment of the fracture toughness of Al-Si-Mg alloys. Lee et al. [11] investigated the effect of the Si-particles on the fracture toughness of A356 alloy cast, using different casting technologies. The comprehensive conclusion rising up from these studies is that the resistance to crack growth increases with enhancing the degree of refining of dendrite cells and eutectic silicon, whereas the crack tip plastic is higher in slowly solidified microstructure (sand castings) and lower in permanent mold or, die casting. Hence, the factors favoring the fracture toughness would be decreased dendritic cell size and refinement of Si-eutectic and intermetallic, the opposing factor would be reduced plasticity due to increase in yield strength, both due to primary cell and eutectic refinement. Further, the influence of minor chemical modification has been analyzed by Alexopoupolos [9]. However, as reported by Staley [4] there are several extrinsic factors such as porosity, oxides and inclusions that tend to affect the fracture toughness of these class of alloy.

In this framework, the present work proposes a study on the fracture toughness of a A356 Al alloy and its Cu-containing (1wt.%) variants, under four different aging conditions. The toughness was obtained through crack growth resistance curves (J-R curves) which were determined by the unloading compliance method. In order to assess the mutual influence

of casting defects and alloys hardness, as resulting after aging treatments, hardness results have been composed together with porosity values, and finally integrated with the J_{IC} values. In addition, microstructural observations were carried out to endorse the fracture mechanism.

2. Materials and Methods

2.1 *Materials*

The compositions of the alloys studied are listed in Table 1. They were prepared so as to contain different populations of porosity. The castings were obtained with a gravity die casting process using a copper mold of 65x103x40 mm^3. Aiming to collect a wide range of Secondary Dendrite Arm Spacing (SDAS) variety, specimens for fracture testing were sectioned from different zones in the casting ingot. Four different heat treatments were applied, details and related specimen codes are presented in Table 2.

Table 1 – Chemical compositions (wt.%) of A356 reference alloy and Cu-added A356 alloy as measured by OES.

Alloy	Si	Mg	Fe	Cu	Ti	Sr	Al
A356 (reference)	6.624	0.216	0.086	0.006	0.103	< 0.001	bal.
A356 + 1 wt.% Cu	6.915	0.262	0.091	0.983	0.086	< 0.001	bal.

Table 2 – Cast Al alloys, heat treatment conditions, and specimen codes.

Cast Al alloy	Heat treatment	Specimen code
A356 A356 + 1 wt.% Cu	5 h at 530 °C + 2 h at 190 °C	Ref 2_190 1Cu 2_190
A356 A356 + 1 wt.% Cu	5 h at 530 °C + 4 h at 190 °C	Ref 4_190 1Cu 4_190
A356 A356 + 1 wt.% Cu	5 h at 530 °C + 4 h at 155 °C	Ref 4_155 1Cu 4_155
A356 A356 + 1 wt.% Cu	5 h at 530 °C + 10 h at 155 °C	Ref 10_155 1Cu 10_155

2.2 *Fracture testing*

Fracture toughness tests were performed on C(T) specimens according to ASTM E1820-17 standard 5. Main nominal dimensions of the specimens are shown in Figure 1. Fatigue

pre-cracking was carried out according to the same standard, in air and under the load ratio R = 0.1, using an MTS Landmark servo-hydraulic machine instrumented with ±25 kN load cell. Fracture tests were made in air, at room temperature, and under displacement control in the same servo-hydraulic machine and load cell. However, it was instrumented with an MTS 632.03F-31 fracture extensometer to allow the crack length measurement. Crack lengths were estimated by unloading compliance method through the compliance solution presented in ASTM E561-15a 6 standard for C(T) specimens:

$$\frac{a}{W} = 1.0010 - 4.6695u + 18.460u^2 - 236.82u^3 + 1214.90u^4 - 2143.6u^5, \quad \text{Equation 1}$$

where

$$u = \frac{1}{1+\sqrt{E'BC_i}}. \quad \text{Equation 2}$$

For plane strain conditions, the appropriate effective elastic modulus is $E' = E/(1-\upsilon^2)$. B is the specimen thickness and C_i is the CMOD compliance ($C_i = \Delta CMOD/\Delta P$).

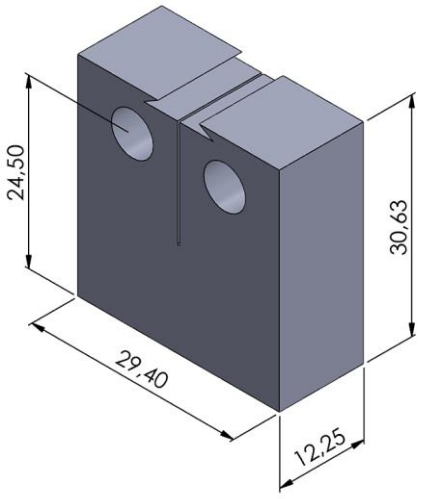

Figure 1 – Compact-tension C(T) test specimens. Main nominal dimensions (in mm).

2.3 *Microstructural investigation*

Samples for microstructural investigations were cut from the fractured tested specimens about 10 mm below the fracture surface, embedded in phenolic resin and prepared using standard grinding and polishing procedures. Microstructure analyses were performed using a Leica DMi8 polarized light optical microscope (OM). Quantitative metallography was carried out using the LAS image analysis software. A measurement field was systematically

defined by composing 8-12 frames at a magnification of 250 x. Pore Area Pct. was calculated as the ratio between 'analyzed pores surface area (μm^2)' and 'total analyzed surface area (μm^2)'. Eutectic Si particles characteristics such as: Aspect Ratio (AR), and Equivalent Circle Diameter (ED) were measured following the procedures described in 7. SDAS measurements were performed using the line intercept method, over 10 fields at 50 x magnification.

2.4 *Hardness tests*

Vickers hardness tests (HV) were conducted with a Leica VMHT micro Vickers tester with a load of 500 gf and a dwell time of 15 s, according to the UNI EN ISO 6507 specification. Further hardness examinations were performed with a load of 25 gf with the aim of testing the sole aluminum α- matrix.

2.5 *Fracture surfaces analysis*

Fracture surfaces were studied with a ZEISS ULTRA 55 field emission scanning electron microscopy (FE-SEM). Element mapping were obtained through energy dispersive X-ray spectroscopy (EDS), operated at an acceleration voltage of 20Kv.

3. Results

3.1 *P-CMOD records*

Figure 2 represents typical experimental load (*P*) *vs.* crack mouth opening displacement (CMOD) record for the tested C(T) specimens. In this case, the behavior of Ref 10_155 C(T) specimen is presented. Unloading-reloading sequences necessary for the elastic compliance technique can be clearly seen.

3.2 *J-Δa curves*

Figure 3 summarizes *J*-R curves of the eight investigated specimens sorted by color as a function of the chemical composition, and by symbol as function of the heat treatment condition. Auxiliary lines according to ASTM E1820-17 were also plotted. It can be observed that while the majority of the curves are found to be grouped in the same area in the plot, the Ref 4_155 and 1Cu 4_155 corresponding *J*-R curves show a higher trend, indicating a better fracture toughness response.

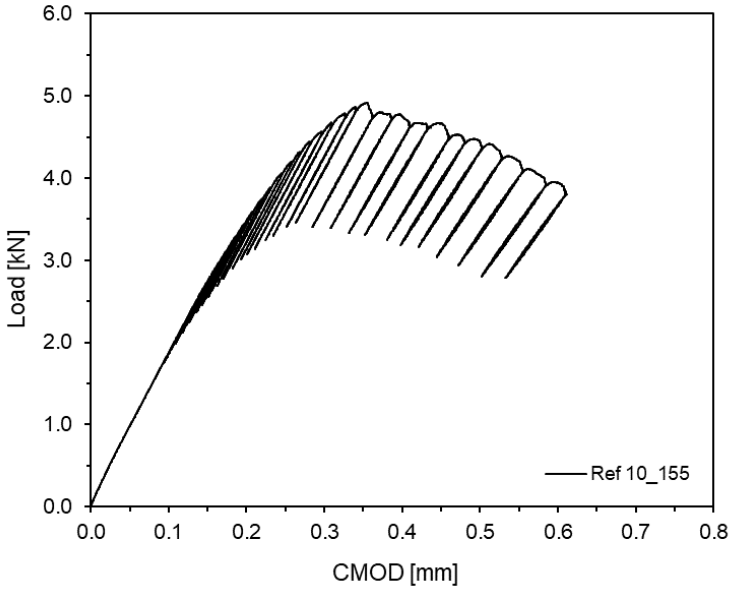

Figure 2 – Typical experimental *P*-CMOD record for the Ref 10_155 C(T) specimen.

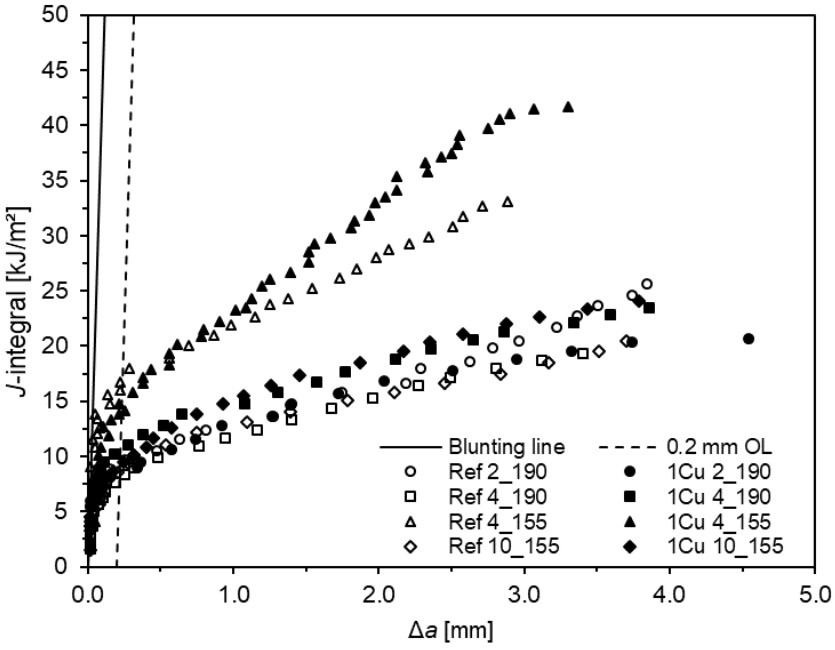

Figure 3 – Experimental *J*-Δ*a* pairs for the tested specimens.

3.3 *Fracture surface and crack lengths measurements*

After the fracture tests, specimens passed through a fatigue post-cracking in order to mark the end of stable crack growth. Figure 4 and Figure 5 show typical fracture surfaces of the tested specimens. EDM notched (dark smooth region), fatigue pre-cracked (first clear region), stable crack growth, and fatigue post-cracked regions can be observed in both figures.

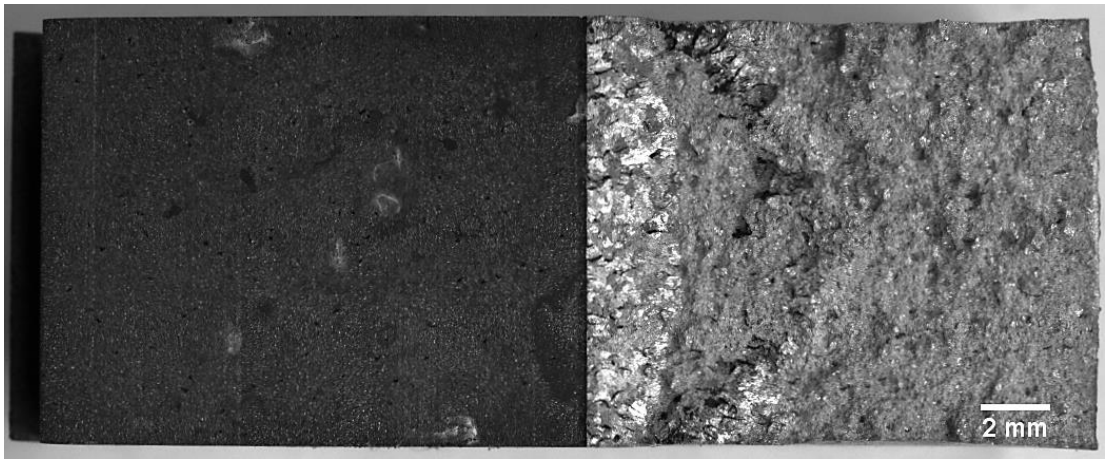

Figure 4 – Fracture surface of Ref 4_155 C(T) specimen.

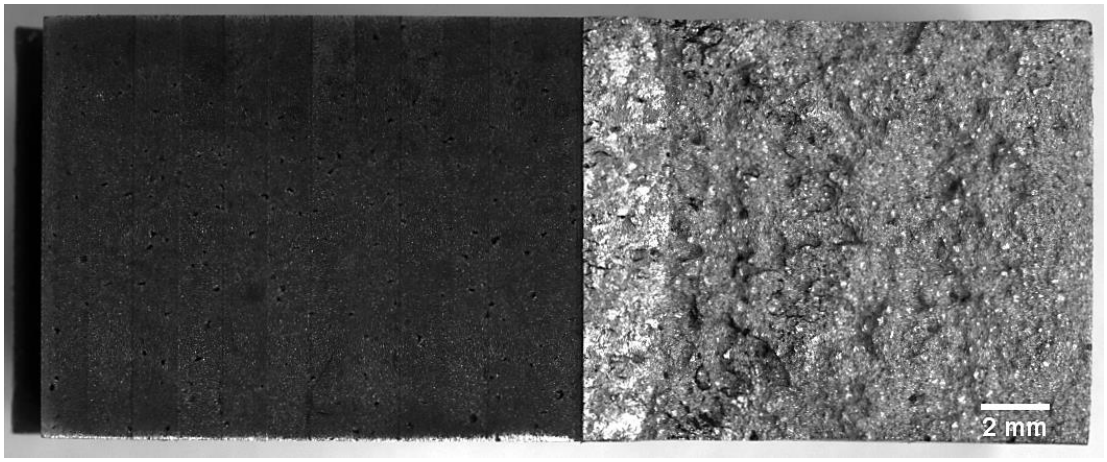

Figure 5 - Fracture surface of 1Cu 10_155 C(T) specimen.

Initial and final physical crack lengths were measured from fracture surfaces according to BS 7448-1:1991 standard 8. Table 3 presents initial (a_0) and final (a_f) crack lengths measurements as well as a_0/W of each C(T) specimen.

Table 3 – Crack lengths measurements of the tested specimens.

Specimen	a_0 [mm]	a_f [mm]	a_0/W
Ref 2_190	12.84	16.67	0.52
1Cu 2_190	12.57	17.10	0.51
Ref 4_190	12.86	16.25	0.53
1Cu 4_190	12.86	16.70	0.52
Ref 4_155	12.85	15.72	0.53
1Cu 4_155	12.91	16.20	0.53
Ref 10_155	12.02	15.71	0.49
1Cu 10_155	12.87	16.64	0.53

3.4 *Fracture toughness evaluation*

Fracture toughness were determined according to ASTM E1820-17 procedure. Table 4 presents the fracture toughness values (J_{Ic}) of each specimen tested. In order to understand the influence played by: Cu content, heat treatments and microstructural features over the fracture toughness behavior, metallographic analysis and hardness measurements were performed.

Table 4 – J_{Ic} values for the investigated alloys.

HT	2_190		4_190		4_155		10_155	
CC	Ref	1Cu	Ref	1Cu	Ref	1Cu	Ref	1Cu
J_{IC}	9.4	8.2	8.3	10.9	16.9	14.7	9.3	9.4

3.5 *Metallographic analysis*

The microstructural properties examined in this analysis encompasses: SDAS, pore area percentage, eutectic silicon particle characteristics (AR and ED) and hardness (HV_{500gf} and HV_{25gf}), a list of the averaged values is given in Table 5. SDAS measurements range from 34 to 70 µm. Porosity, evaluated in pct. as the measured surface pore area, is varying from the 0.92 % up to 3.9%. Representative examples are presented in Figure 6-a and Figure 6-b. With reference to characteristics of the eutectic Si particles, it is possible to observe an overall increase in the eutectic ED size in the Cu-containing alloys as compared to reference A356 alloy; additionally, the former case offers coarse (higher ED) and acicular (higher AR) Si particles, where the A356 alloys present a fine and well-spherodized eutectic network (Figure 6-c and Figure 6-d). The addition of 1 wt.% Cu to the A356 alloy was aimed at enhancing the strength, thanks to the excellent aging response of the copper element; however, the lower Sr-content resulted after the casting in all the investigated alloys, appeared not to prevent the detrimental influence of the addition of the Cu to the eutectic structure, as also observed by 9.

Table 5 - SDAS, percental pore area, eutectic Si particles characteristics, and Vickers hardness for the investigated alloys.

Specimen code	SDAS (µm)	Pore area %	AR	ED	$HV_{500\ gf}$	$HV_{25\ gf}$
Ref 2_190	47.43 ± 5.62	2.094	1.44	2.82	97.92 ± 1.82	97.06 ± 3.03
1Cu 2_190	56.37 ± 6.13	3.929	1.80	4.39	89.94 ± 4.98	94.67 ± 4.12
Ref 4_190	61.03 ± 4.45	1.913	1.53	3.18	94.72 ± 1.78	94.27 ± 2.88
1Cu 4_190	34.30 ± 4.09	0.921	1.54	3.81	94.32 ± 2.73	99.19 ± 2.01
Ref 4_155	69.60 ± 7.89	2.890	1.90	3.62	84.60 ± 5.93	65.94 ± 1.95
1Cu 4_155	58.25 ± 5.11	0.967	1.48	2.97	83.67 ± 7.96	70.29 ± 2.78
Ref 10_155	57.35 ± 7.29	1.690	1.48	3.52	92.00 ± 3.51	82.99 ± 2.57
1Cu 10_155	52.12 ± 6.37	2.658	1.92	4.30	86.55 ± 6.09	94.87 ±3.29

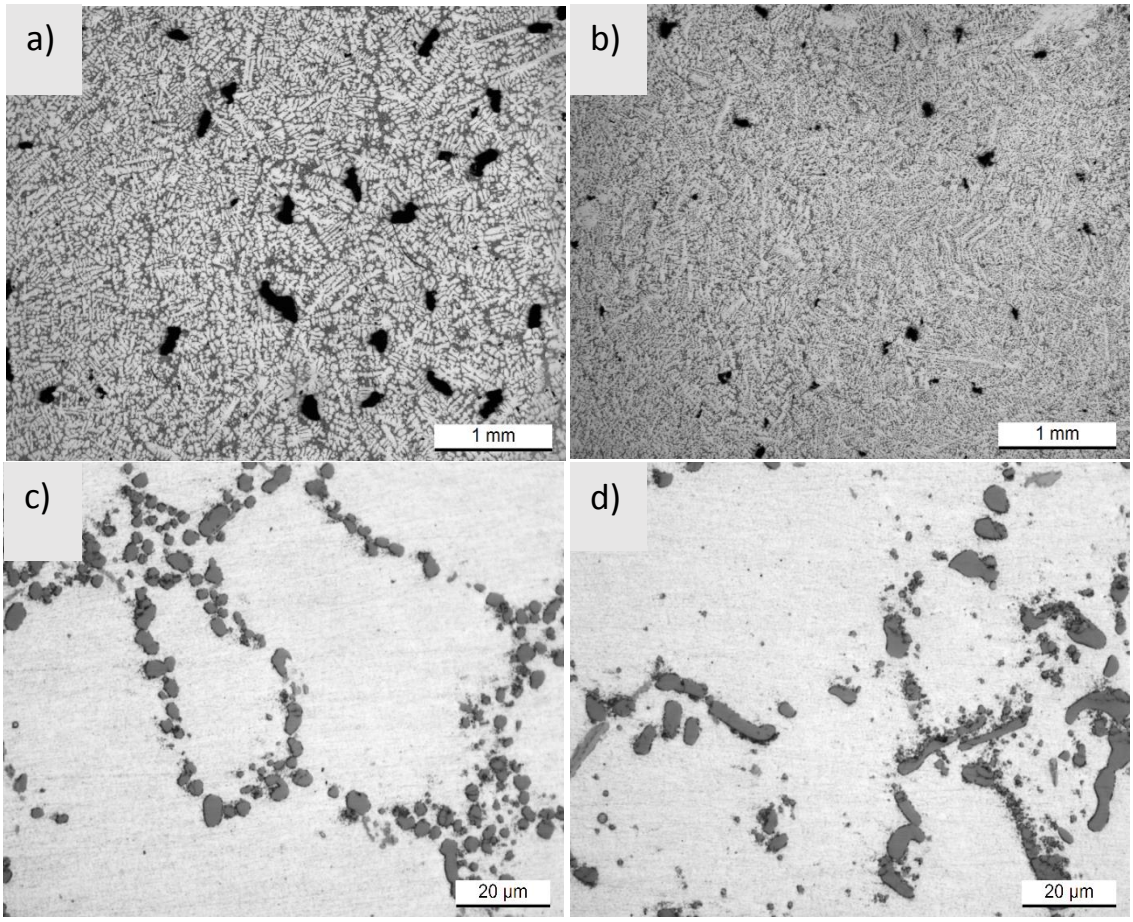

Figure 6 - Representative population of porosity in the Ref 2_190 specimen of A356 alloy (a) and in the 1Cu 4_190 specimen of Cu-added A356 alloy (b). Eutectic Si Particles in the Ref 2_190 specimen of A356 alloy (c) and in the 1Cu 2_190 specimen of Cu-added A356 alloy (d).

3.6 *Fracture toughness (J_{IC}) correlations*

The J_{IC} values, given in Table 4, have been plotted in Figure 7 as a function of porosity (a) and hardness (b). Although the effect of porosity on fracture toughness is well known 10, the trend line in Figure 7-a does not offer an evident linear correlation, suggesting a possible contribute of other parameters influencing fracture toughness response. Therefore, the J_{IC} have been plotted against the $HV_{500\ gf}$ values (Figure 7-b), but unfortunately even in this case, any clear correlation rose up.

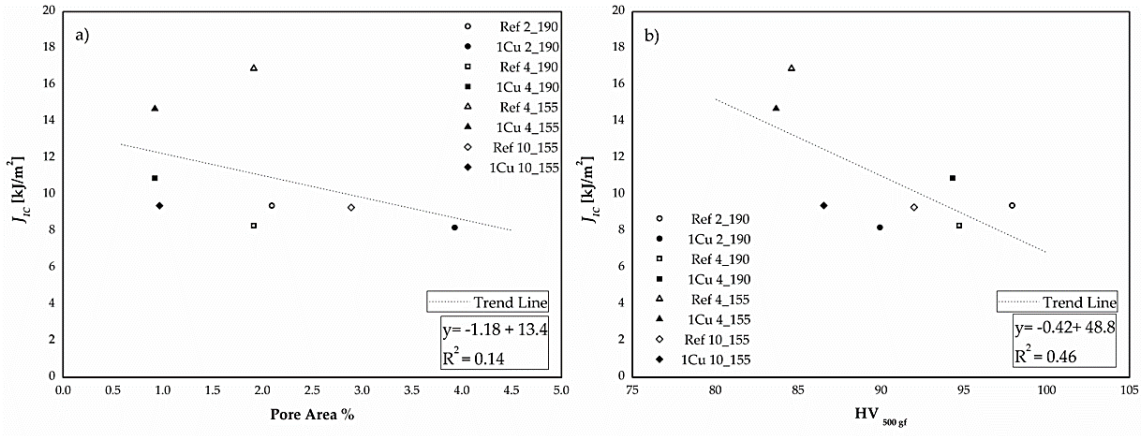

Figure 7 - Fracture toughness correlation between (a) porosity and (b) Vickers hardness 500 gf.

3.7 *Fractographic observations*

Figure 8 shows mid-sections of crack path for the two representative Cu-containing samples aged under different conditions: a) aged 4h at 155° C and b) aged 2h at 190°. Further insights of microstructural features leading the crack are presented in Figure 9. The presence of shrinkage porosity paves the way to the crack propagation, besides that, crack paths extend along solidification cells, where eutectic Si particles are mainly segregated and easily connected to play a bridging role. In addition, microcrack initiation at the eutectic Si particles are visible in the images c) and e) of Figure 9 (distinguished by circles).

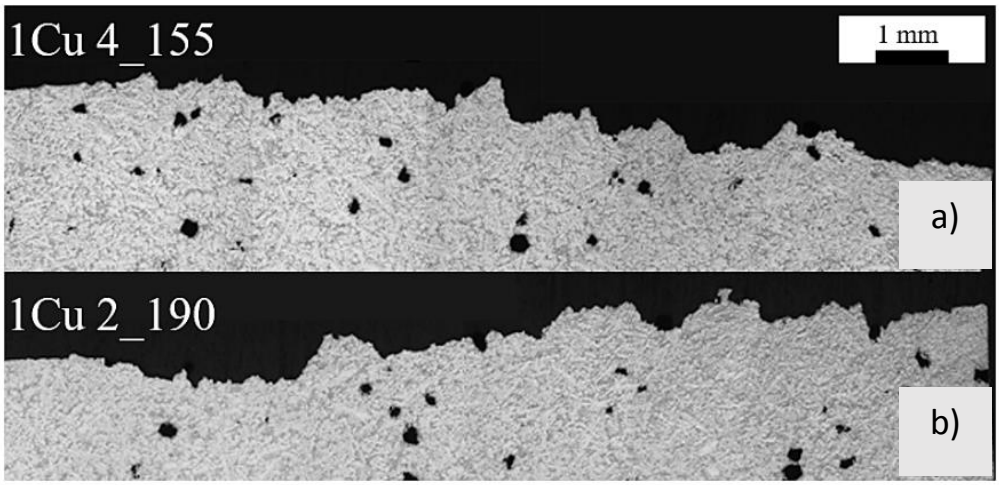

Figure 8 - Mid-section crack paths of two representative C(T) specimens. Image a) specimen 1Cu 4_155 and image b) specimen 1Cu 2_190.

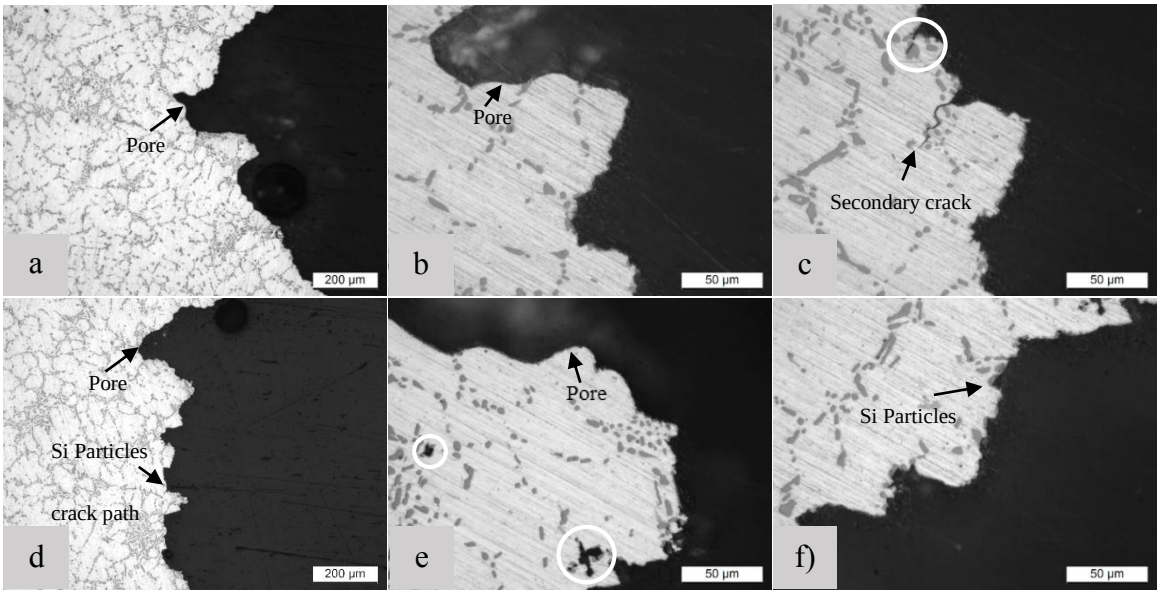

Figure 9 - Microstructural features in the region of unstable crack propagation of two representative C(T) specimens. a-c)1Cu 4_155; d-f) 1Cu 2_190.

Figure 9-a and Figure 9-c are representative fractographies of the C(T) specimen 1Cu 4_155, taken at different magnification. The presence of shrinkage pores (also observed in Figure 7 and Figure 8) greatly affect the fracture surface morphology (Pore Area pct. = 2.89). Higher magnifications, images b) and c) of Figure 9, reveal the typical features of ductile fracture. The dimple size tends to decrease in the proximity of the pore boundary-matrix interface. Pore boundary-matrix interface have been deeply investigated as reported in Figure 10. Aiming to clearly evidence both the α-Al matrix (in red) and the eutectic Si particles (in green), EDS maps of Al and Si, have been provided.

Microcracks within the Si particles are clearly observed in both the Cu-added (see image (c) in Figure 11) and the A356 reference (see image (e) in Figure 11) alloys. In accordance with Table 5, Si particles in the A356 reference alloy appear smaller (lower ED) and more spherodized (lower AR) as compared to the Cu containing alloy. The most of cracked Si particles are observed along the interdendritic regions, where are mainly segregated and easily connected to play a bridging role. Moreover, shear bands observed in both the investigated alloys (see images (c) to (f) in Figure 10) reveal the matrix contribution to the crack propagation.

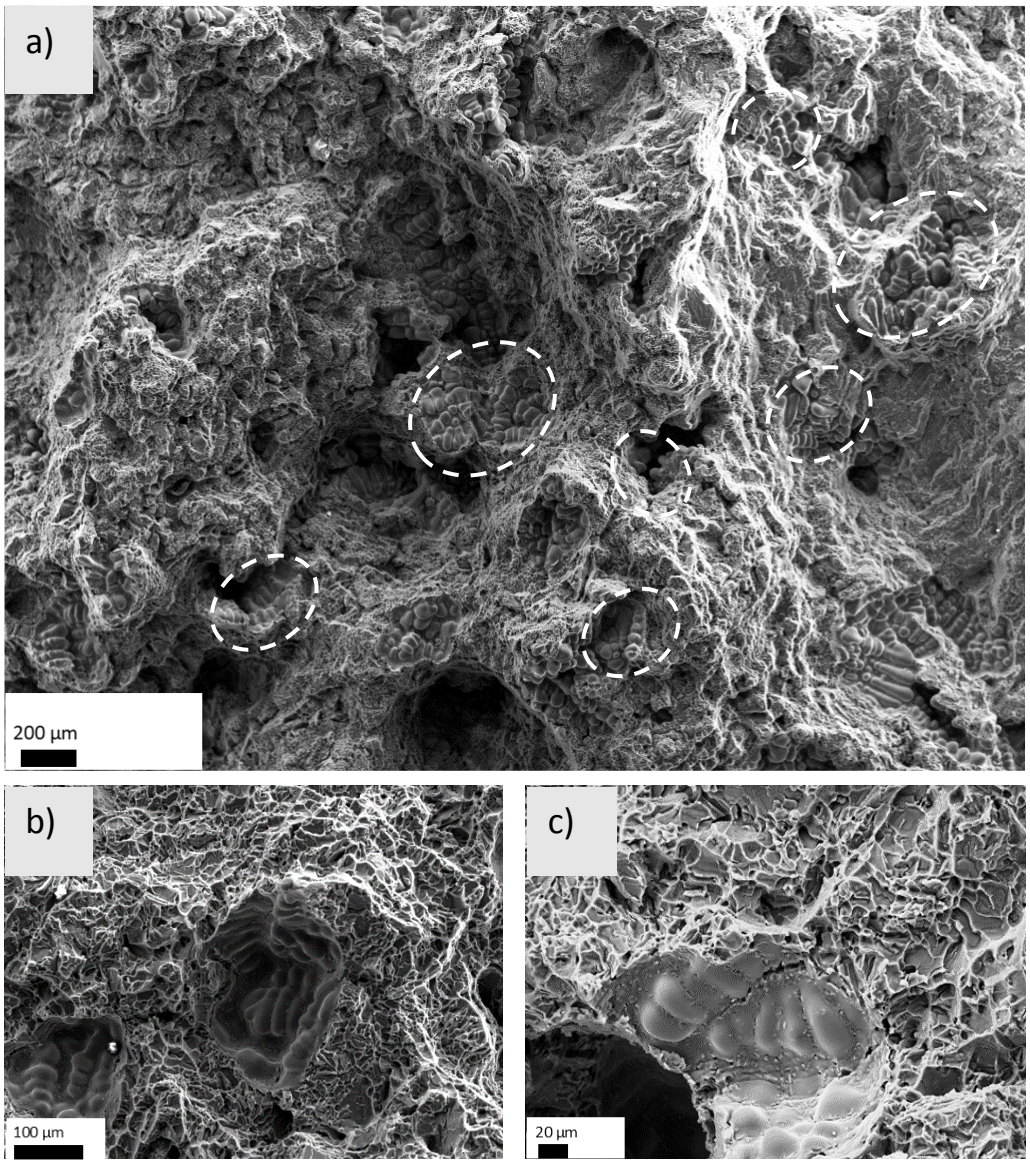

Figure 10 – SEM images of fracture surface showing typical casting defects. C(T) Specimen 1Cu 155_4.

4. Discussion

Based on previous study proposed by Lee *et al.* 11, which exploited the fracture mechanism of A356 alloy through in-situ SEM analysis, two considerations about the microstructural behavior of this alloy during the fracture tests can be addressed:

At the early stage of the fracture test, when a small load is applied, microcracks are initiated at the eutectic Si particles in interdendritic regions (images (c), and (e) of Figure 9 and images (c) to (f) of Figure 10). According to Lee, a more refined microstructure should result in a lower apparent fracture toughness, on account of reduced spacing between the

eutectic Si particles that encourage the fracture initiation. With increased load, the crack growth can be described as a sequential process of crack propagation along shear bands (images (c) and (d) of

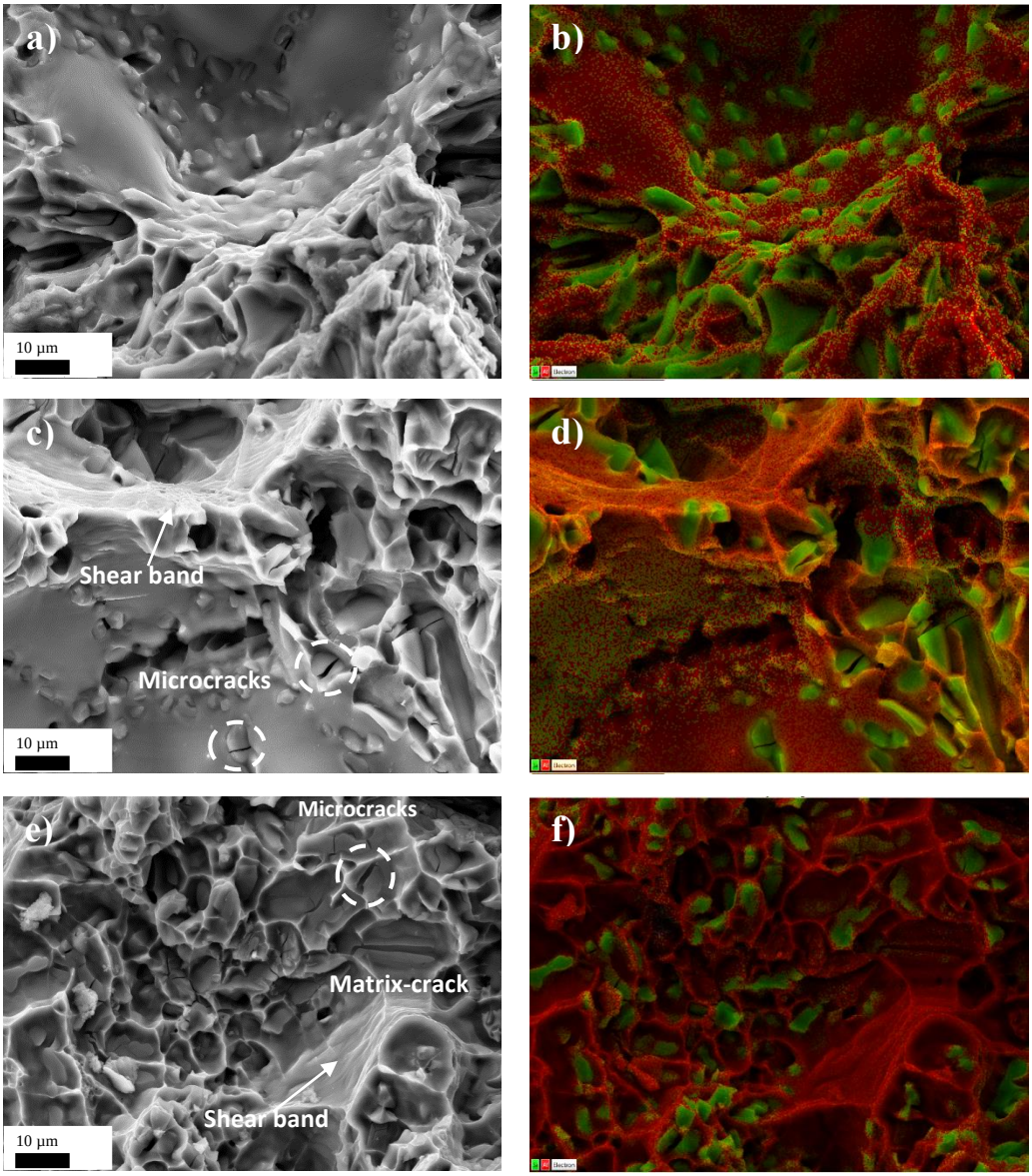

Figure 11 - SEM images of fracture surfaces and EDS maps of Al and Si. Images a) to d) Specimen 1Cu 4_155; Images e) and f) Specimen Ref 4_190.

In this context and comparing the present investigation with the *Lee*'s study, the discussion can be expanded in two main topics:

(1) Referring to the current study, it is important to include the significant presence of shrinkage pores. According to Lee, 1Cu's coarser eutectics are expected to offer higher J_{Ic} values as compared to the Ref A356 alloys. However, with the exception of the alloys aged 4 h at 190° C, Cu-containing alloys present higher porosity, and in turns, fracture initiation is facilitating. Besides the fact that porosity appears to be the foremost fracture leading parameter, a qualitative evidence of the eutectic microstructure contribution toward the fracture toughness can be given observing the 10_155 specimens case. In details: with incrementing porosity by 57% moving to the Reference alloy to the Cu-containing alloy, pretty similar fracture toughness values are observed in the two investigated alloys (9.3 *vs* 9.4 for the Ref and Cu1 alloys, respectively). This might be addressed to the coarsen and less spherodized eutectic microstructure observed in the Cu1 alloy (AR = 1.92 and ED = 4.30 μm) as compared to the Ref case (AR = 1.48 and ED = 3.52 μm). As proposed by Seideffine 12, the addition of Cu is found to promote the formation of coarse Si particles, and to enlarge the solidification interval, increasing the shrinkage porosity. Voids formed at the interfacial separation between eutectic Si particles and the aluminum α-matrix are not observed in the alloys investigated. This suggest a good particle-matrix interfacial strength, own to the presence of Si within the matrix 12. It is possible to presume that the load transfer is mainly supported by the Si particle-matrix interface, and that the shear-lag type strengthening effect 14 plays a crucial role in the increased strength due to eutectic Si particles. Hence, if considering the alloy investigated as composite material where the α-Al phase is the matrix that needs to be reinforced, while the network of eutectic Si particles compounds is the stronger phase acting as a reinforcement 15, it is possible to understand the hardness response reported in Table 5, that show a decrease in HV with adding Cu. The finer and uniform are the eutectic Si particles distributions, the higher is the reinforcement achieved.

Aiming to evaluate the mutual influence of casting defects and alloys hardness, as resulting after aging treatments, hardness results have been composed together with porosity values, and finally integrated with the J_{IC} values, as shown in Figure 12. In this figure, it is possible to observe how the material crack growth resistance is concurrently influenced by both the hardness and porosity. As a matter of fact, for similar hardness (specimens Ref and Cu 4_155), J_{IC} considerably decrease with increasing the porosity, while for similar pore area % values, J_{IC} increases with hardness decreasing.

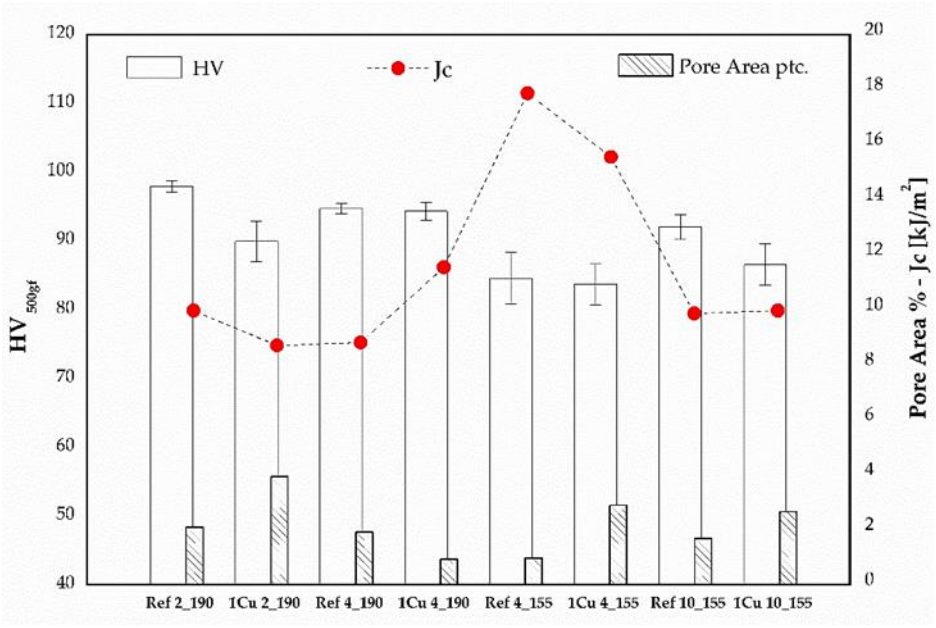

Figure 12 - Fracture toughness vs porosity and Vickers hardness 500 gf.

(2) Focusing now on the *J*-R curve, Figure 3 clearly evidence higher trends for the Cu-containing alloys as compared to the A356 reference alloys. It is reasonable to assume that where the crack initiation is mainly ruled by the mutual cooperation between casting defects and alloy (eutectic network + α-Al matrix) hardness response, the crack propagation appears to be controlled by the content of hardening precipitates, enriching the α-matrix. As a matter of fact, the addition of Cu on A356 alloy enable the formation of Cu-reach precipitates, which reinforce the aluminum matrix, together with Mg-rich precipitates, already present in the A356 alloy (see HV_{25gf} in Table 5). Assuming that the crack propagates along shear bands, it is possible to presume that the precipitates in the matrix might counteract the shear bands sliding, through 'Orowan Mechanism' 16.

5. Conclusions

The present work proposes a study on the fracture toughness of a A356 Al alloy and its Cu-containing (1wt.%) variant, under four different aging conditions. In order to assess the mutual influence of casting defects and alloys hardness, as resulting after aging treatments, hardness results have been composed together with porosity values, and finally integrated with the J_{IC} values. Based on this study, the following conclusions can be derived:

- At the early stage of the fracture test, when a small load is applied, microcracks are initiated at the eutectic Si particles in interdendritic regions. A more refined microstructure should result in a lower fracture toughness, on account of reduced spacing between the eutectic Si particles.
- Besides the fact that porosity appears to be the foremost fracture leading parameter, there is evidence of eutectic microstructure contribution toward the fracture toughness.
- Fracture toughness is concurrently influenced by both hardness and porosity
- J-R curves evidenced higher trends for the Cu-containing alloys as compared to the A356 reference alloys.
- Where the crack initiation is mainly ruled by the mutual cooperation between casting defects and alloy (eutectic network + α-Al matrix) hardness response, the crack propagation appears to be controlled by the content of hardening precipitates, enriching the α-matrix.

References

1. Anilchandra, A.R., Arnberg, L., Bonollo, F., Fiorese, E., Timelli, G., Evaluating the Tensile Properties of Aluminum Foundry Alloys through Reference Castings – A Review, Materials (2017), 10, 1011.
2. Hafiz, M. F., Kobayashi, T., Fracture toughness of eutectic Al-Si casting alloy with different microstructural features, Journal of Materials Science, Vol. 31 (1996), pp.: 6195-6200.
3. Tirayakioglu, M., Fracture toughness potential of cast Al-7%Si-Mg alloys, Materials Science and Engineering A., Vol. 497 (2008), pp.: 512-514.
4. Staley, J. T., Properties related to fracture toughness. ASTM STP., Vol. 605 (1976), pp.: 71-96.
5. ASTM E1820-17a, Standard Test Method for Measurement of Fracture Toughness. ASTM International, West Conshohocken, PA, 2017, www.astm.org.
6. ASTM E561-15a, Standard Test Method for *K*-R Curve Determination, ASTM International, West Conshohocken, PA, 2015, www.astm.org.
7. Lattanzi, L., Di Giovanni, M. T., Giovagnoli, M., Fortini, A., Merlin, M., Casari, D., Di Sabatino, M., Cerri, E., Garagnani, G. L., Room Temperature Mechanical Properties of A356 Alloy with Ni Additions from 0.5 Wt to 2 Wt%, Metals 2018, Vol. 8(4), 224.
8. BS 7448 Part 1: Method for determining of K_{Ic}, critical crack tip opening displacement (CTOD) and critical *J* values of fracture toughness for metallic materials under displacement controlled monotonic loading at quasistatic rates, British Standards Institution, London, 1991.
9. Alexopoulos, N. D., Tiryakioğlu, M., Relationship between Fracture Toughness and Tensile Properties of A357 Cast Aluminum Alloy, Metallurgical and Materials Transactions A, Vol. 40A (2009), pp.: 702-716.
10. Srinivasan, M., Seetharamu, S., Fracture Toughness of Metal Castings, Science and Technology of Castings Processes, *Chapter 10*, IntechOpen (2012), pp.: 285-312.
11. Lee, K., Kwon, Y.N., Lee, S., Effects of eutectic silicon particles on tensile properties and fracture toughness of A356 aluminum alloys fabricated by low-pressure-casting, casting-forging, and squeeze-casting processes, Journal of Alloys and Compounds, Vol. 461 (2008), pp.: 532-541.

12. Seifeddine, S., Sjölander, E., Bogdanoff, T., On the Role of Copper and Cooling Rates on the Microstructure, Defect Formations and Mechanical Properties of Al-Si-Mg Alloys, Materials Sciences and Applications, Vol. 4, nº 3 (2013), pp.: 171-178.
13. Poruks, P., Yakubtsov, I., Boyd, J.D., Martensite-ferrite interface strength in low-carbon bainitic steel, Scripta Materialia, Vol. 54 (2006), pp.: 41-45.
14. Nardone, V.C., Prewo, K.M., On the strength of discontinuous silicon carbide reinforced aluminum composites, Scripta Metallurgica, Vol. 20 (1986), pp.: 43-48.
15. Asghar, Z., Requena, G., Boller, E., Three-dimensional rigid multiphase networks providing high-temperature strength to cast AlSi10Cu5Ni1-2 piston alloys, Acta Materialia, Vol. 59, nº16 (2011), pp.: 6420-6432.
16. Sjölander, E., Seifeddine, S., The heat treatment of Al-Si-Cu-Mg casting alloys, Journal of Materials Processing Technology, Vol. 210, Issue10, (2010), pp.: 1249-1259.
17. Tohgo, K., & Oka, M. (2004). Influence of coarsening treatment on fatigue strength and fracture toughness of Al-Si-Mg alloy castings. Key Engineering Materials, 261-263, 1263-1268.

Article 5

Fatigue crack growth behavior of a selective laser melted AlSi10Mg

M.T. Di Giovanni, J. T.O. de Menezes, G. Bolelli, E. Cerri, E. M. Castrodeza.

submitted to Engineering Fracture Mechanics.

Fatigue crack growth behavior of a selective laser melted AlSi10Mg

Maria Teresa Di Giovanni[1], Joao Teixeira Oliveira de Menezes[2], Giovanni Bolelli[3], Emanuela Cerri[1], Enrique Mariano Castrodeza[2,4]

[1]Department of Engineering and Architecture, University of Parma, Parco Area delle Scienze 181/A, 43124 Parma, Italy.

[2]Department of Metallurgical and Materials Engineering, COPPE/Federal University of Rio de Janeiro, 21941-972 Rio de Janeiro, Brazil.

[3]Department of Engineering "Enzo Ferrari", University of Modena and Reggio Emilia, Via Pietro Vivarelli 10/1, 41125 Modena, Italy

[4]Departament of Mechanical Engineering, Politecnico di Milano, Via La Masa 1, 20156 Milano, Italy

ABSTRACT

Selective Laser Melting (SLM), an additive manufacturing (AM) technology, has experienced a large growth in the past few years due to his high flexibility, versatility and customizability and it is now suiting most sectors of industrial production. The SLM technology involves layer by layer melting of the metallic powder by means of a high-power laser beam according to the instructions provided by CAD files. It is well known that the SLM process is characterized by high temperature gradients leading to rapidly solidified, non-equilibrium microstructures. High localized thermal gradients and very short interaction times, which leads to rapid volume changes, cause substantial residual stress development. As a result, the mechanical properties of SLM parts can differ substantially from one another and from those produced by conventional techniques. In order to meet the full potential that the SLM has to offer, especially for flight-critical components, studies and qualifications are needed. In this light, the present study examines the high cycle fatigue crack growth behavior in the linear region of da/dN vs. ΔK diagrams (described by the Paris law) of AlSi10Mg alloy for different experimental conditions.

Specimen building orientation and notch position have been combined to obtain 4 different crack growth orientations. Further, specimens were tested in both as-built (AB) and T6 heat treated (T6) conditions. The Fatigue Crack Growth (FCG) curves revealed the beneficial influence of the heat treatment on the FCG response, as compared to the as-built case. On the other hand, the latter' fatigue crack growth behavior is found to be strongly dependent on the material orientation. Fractographic analysis and residual stress measurements have been further performed to understand the mechanisms involved.

Keywords: Selective Laser Melting, AlSi10Mg alloy, Fatigue Crack Growth, Residual Stress, Paris Law.

Introduction

Selective Laser Melting (SLM), an additive manufacturing (AM) technology, has been experiencing a large growth since the past few years due to his high flexibility, versatility and customizability and it is now suiting most sectors of industrial production. The SLM technology involves layer by layer melting of the metallic powder by means of a high-power laser beam according to the instructions provided by CAD files [1]. Rapid cooling rates and directional solidification induced by the SLM process result in non-equilibrium microstructure (metastable phases, non-equilibrium compositions, solute trapping), fine and ultra-fine grains, occasionally anisotropically elongated, and metallurgical defects (porosity due to unmelted powders and/or gas entrapment) [2-3]. In addition, high localized thermal gradients and very short interaction times, which leads to rapid volume changes, causes substantial residual stress development. As a result, the mechanical properties of SLM parts can differ substantially from one another and from those produced by conventional techniques. In order to meet the full potential that SLM has to offer, especially for flight-critical components, studies and qualifications are needed. So far, the most pertinent literature has focused on static mechanical properties and on optimizing the scan strategy and microstructures [4,5,6,7]. To the authors' knowledge there are few works [8,9] exploring the dynamic response of AlSi10Mg SLM parts. In this framework the present work investigates the fatigue crack growth behavior for this aluminum alloy, and in particular, considering that crack initiation and propagation are critically sensitive to the interaction between fracture path, orientation and microstructure [10], specimen building

orientation and the notch position have been combined to obtain 4 different crack path conditions. In addition, the influence of the T6 heat treatment on the microstructure, and hence on the crack propagation has been also evaluated. The T6 heat treatment encompassed: 4h of solution heat treatment at 505 °C followed by 4h of aging treatment at 175 °C. Fractographic analysis has been further performed to understand the mechanical and physical mechanisms occurred.

Materials and methods

Materials

Within this work, a SLM 500 machine with a 500 x 280 x 360 mm^3 platform was used. Argon was applied as the inert gas and the platform temperature was kept constant at 200 °C throughout the entire manufacturing process. SLM processing was performed with a laser power of 350 W, using a laser beam having a spot size diameter of 80 µm. The scan speed was 1.15 m/s, the hatch spacing was 170 µm, the hatch rotation between build was of 67 and the layer thickness was 50 µm, resulting in an energy density of 35.8 J/mm^3. Standard compact-tension C(T) specimens were manufactured using an Al-alloy AlSi10Mg (according to EN AC-43000) feedstock powder for the determination of fatigue crack growth properties. Powder particles had spherical shape and their size ranged between 20-63 µm. Geometry and the main nominal dimensions of the C(T) specimens are presented in Figure 13. During the SLM process, layers were built on the X-Y plane and stacked along the Z-direction. A full set of C(T) specimens for the FCG testing was manufactured in one build-platform in order to avoid possible variation associated with powder quality. The crack notch was machined by Electro-Discharge Machining (EDM). Specimens' designation as a function of both loading and notch directions is given in the drawing on the right in Figure 13. Half of the specimen set was tested as-built, whereas the other half has been successively heat treated according to the standard T6 heat treatment, which encompassed 4h of solution heat treatment at 505 °C followed by room temperature water quench, 1h storage and finally 4h of aging at 175 °C. In the text, the specimens tested in the as-built condition are referred to as AB, whereas the T6 heat treated specimens are referred to as T6.

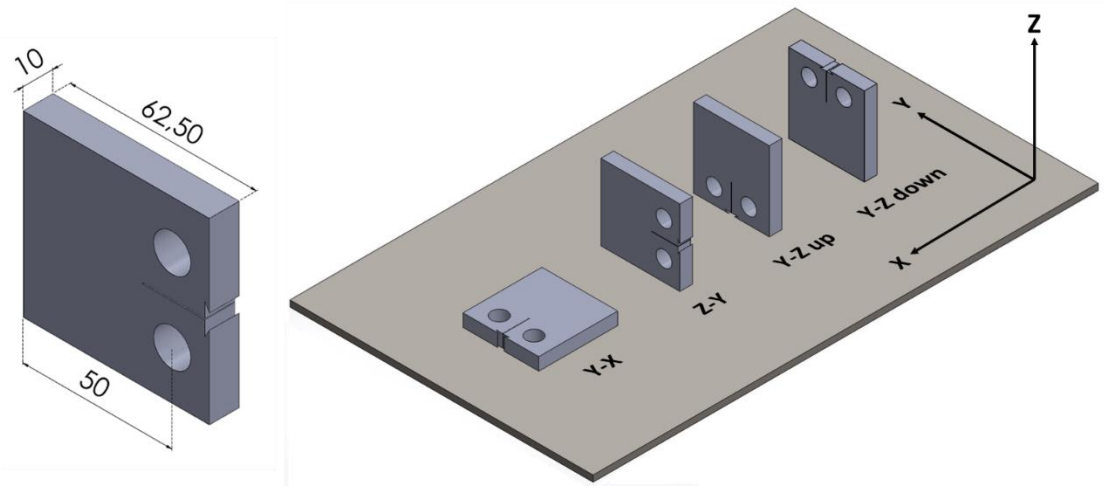

Figure 13 – Compact tension (C(T)) specimens with main nominal dimensions (in mm) and the specimens' designation as a function of both loading and notch directions.

Fatigue Crack Growth

FCG tests were performed according to ASTM E647–15 standard [11] in an MTS Landmark servo-hydraulic machine instrumented with a 25 kN load cell and an MTS 632.02F-20 fracture extensometer for CMOD measurements. C(T) specimens were fatigue pre-cracked in the same machine. Fatigue pre-cracking and FCG testing were done in air, at room temperature, under load ratio R = 0.1, and under a frequency of approximately 25 Hz. In order to obtain the experimental d*a*/dN *vs*. Δ*K* curves and the Paris coefficients, the constant-force-amplitude procedure was used, where specimens are tested at a constant force range (Δ*P*). Specimens identification and FCG testing parameters (including final K_{max} after pre-cracking, initial K_{max} applied in the FCG test, and the constant force range applied (Δ*P*)) are reported in Table 6 for specimens in the AB condition, and in Table 7 for the T6 specimens. Excluding the Y-Z_{down} case, two specimens (I and II) have been tested for each experimental condition.

Table 6 – FCG testing parameters (final K_{max} after pre-cracking, initial K_{max} applied in the FCG test, and the constant force range applied (ΔP)) for the AB specimens.

Specimen	Final pre-cracking K_{max} [MPa√m]	Initial FCG K_{max} [MPa√m]	ΔP [kN]
Y-Z_{down} AB I	6.08	6.55	2.88
Y-Z_{up} AB I	3.98	4.61	2.16
Y-Z_{up} AB II	3.99	4.48	1.89
Z-Y AB I	4.17	4.56	1.98
Z-Y AB II	4.21	4.75	1.98
Y-X AB I	4.66	5.02	2.25
Y-X AB II	4.48	4.72	2.07

Table 7 – FCG testing parameters (final K_{max} after pre-cracking, initial K_{max} applied in the FCG test, and the constant force range applied (ΔP)) for the T6 specimens.

Specimen	Final pre-cracking K_{max} [MPa√m]	Initial FCG K_{max} [MPa√m]	ΔP [kN]
Y-Z_{down} T6 I	6.97	8.90	3.60
Y-Z_{up} T6 I	7.09	7.91	3.60
Y-Z_{up} T6 II	7.44	8.14	3.96
Z-Y T6 I	7.89	8.44	3.96
Z-Y T6 II	8.93	9.72	4.50
Y-X T6 I	7.66	8.19	3.78
Y-X T6 II	6.46	6.94	3.24

Fractographic and microstructural analysis

Fractographic analyses were conducted with a ZEISS ULTRA 55 field emission scanning electron microscope (FE-SEM). Element mapping was obtained through energy dispersive X-ray spectroscopy (EDS), operated at an acceleration voltage of 20 kV. The microstructure and the crack path profiles of AB and T6 samples were observed by optical and scanning electron microscopy after polishing and etching with Keller's reagent.

XRD Measurements – Residual stress

Residual stresses were measured by X-Ray Diffraction (XRD: X'Pert PRO diffractometer, PANAlytical, Almelo – NL) on the bottom and top surfaces of Z-Y AB and Z-Y T6 specimens. In order to avoid any influence from the roughness of as-built surfaces, the samples were lightly ground and polished up to colloidal silica suspension.
Cu-Kα radiation generated from a conventional X-ray tube operated at 40 kV and 40 mA in line focus mode was employed. Measurements were performed using the $\sin^2\psi$ method in ω-tilt configuration, and, in order to minimize errors due to sample misalignment, the instrument was equipped with an X-ray mirror on the incident beam path, a parallel plate collimator, a single crystal monochromator and a 0D gas counter on the diffracted beam path [12]. The (422) peak of Al was acquired over the 134.9° - 140.3° range, with a step size of 0.05°/step and a counting time of 10 s/step, for 13 different positive and pseudo-negative ω-tilt values corresponding to $\sin^2\psi = 0, 0.1, \ldots, 0.6$. The procedure was repeated along three distinct φ orientations on the measurement plane (φ = 0°, φ = 90°, φ = 45°), in order to resolve a plane stress state.

Lattice strains were computed as:

$$\varepsilon_{\varphi,\psi}^{(422)} = \frac{d_{\varphi,\psi}^{(422)} - d_0^{(422)}}{d_0^{(422)}} \qquad \text{Equation 3}$$

Where $d_0^{(422)}$ is the reference (unstressed) lattice spacing, whilst $d_{\varphi,\psi}^{(422)}$ is the interplanar spacing obtained, through Bragg's law, from the fitted position of the diffraction peak acquired along the orientation φ at a tilt value ψ. Fitting of the experimental patterns was carried out using the PANAlytical HighScore Plus software, with pseudo-Voigt peak functions accounting for the $K\alpha_1$ and $K\alpha_2$ radiation components.

From lattice strains, in-plane stresses were obtained through equations (2.a), (2.b), (2.c) [13]:

$$\varepsilon_{0°,\psi}^{(422)} = \frac{1}{2}S_2^{(422)}\sigma_1 sin^2\psi + S_1^{(422)}(\sigma_1 + \sigma_2) \quad \text{Equation 4.a}$$

$$\varepsilon_{90°,\psi}^{(422)} = \frac{1}{2}S_2^{(422)}\sigma_2 sin^2\psi + S_1^{(422)}(\sigma_1 + \sigma_2) \quad \text{Equation 2.b}$$

$$\varepsilon_{45°,\psi}^{(422)} = \frac{1}{2}S_2^{(422)}\left(\frac{\sigma_1+\sigma_2}{2} + \tau_{12}\right) sin^2\psi + S_1^{(422)}(\sigma_1 + \sigma_2) \quad \text{Equation 2.c}$$

Where σ_1, σ_2, τ_{12} are the normal stress components along the directions φ = 0°, φ = 90° and the shear stress component, respectively; $\frac{1}{2}S_2^{(422)}$ = 19.02×10^{-6} MPa^{-1} and $S_1^{(422)}$= -4.94×10^{-6} MPa^{-1} are the elastic compliances along the (422) direction of aluminum [14].

Results

Fatigue Crack Growth

Results of the FCG experiments are presented by the d*a*/dN *vs.* Δ*K* curves shown in Figure 14. As can be seen, most of the curves where evaluated in regimes B and C [15]. The linear mid-growth rate region is well known as the Paris regime and can be described by a power function (Paris law). The resulting Paris constants (*C* and *m*) for all the specimens are shown in Table 8.

Microstructure & Fracture Propagation

Microstructure

Figure 15 shows optical micrographs of the microstructure of the as-built (a) and T6 heat-treated (b) SLM AlSi10Mg samples after etching with Keller's reagent.

Figure 15 (a) presents a cellular-dendritic microstructure (α-Al matrix) with an average size about 1 μm. Fibrous Si-network (dark-grey) decorates α-Al grains. A melt track is clearly visible in the micrograph, and as deeply investigated by Thijs et al. [16], across the melt track, three characteristic regions with cellular microstructure of different sizes can be distinguished: coarse cellular zone, transitional zone (at the melt track boundary) and fine cellular zone (within the melt pool).

On the other side, Figure 15 (b) presents microstructural features which remind of AlSi10Mg alloy castings. The fine cellular system is deconstructed during the solution heat treatment and concurrently, the fibrous Si-network coalesces to form Si-conglomerates (dark-grey) with rounded and/or polygonal shapes varying in the range of 1-8 µm.

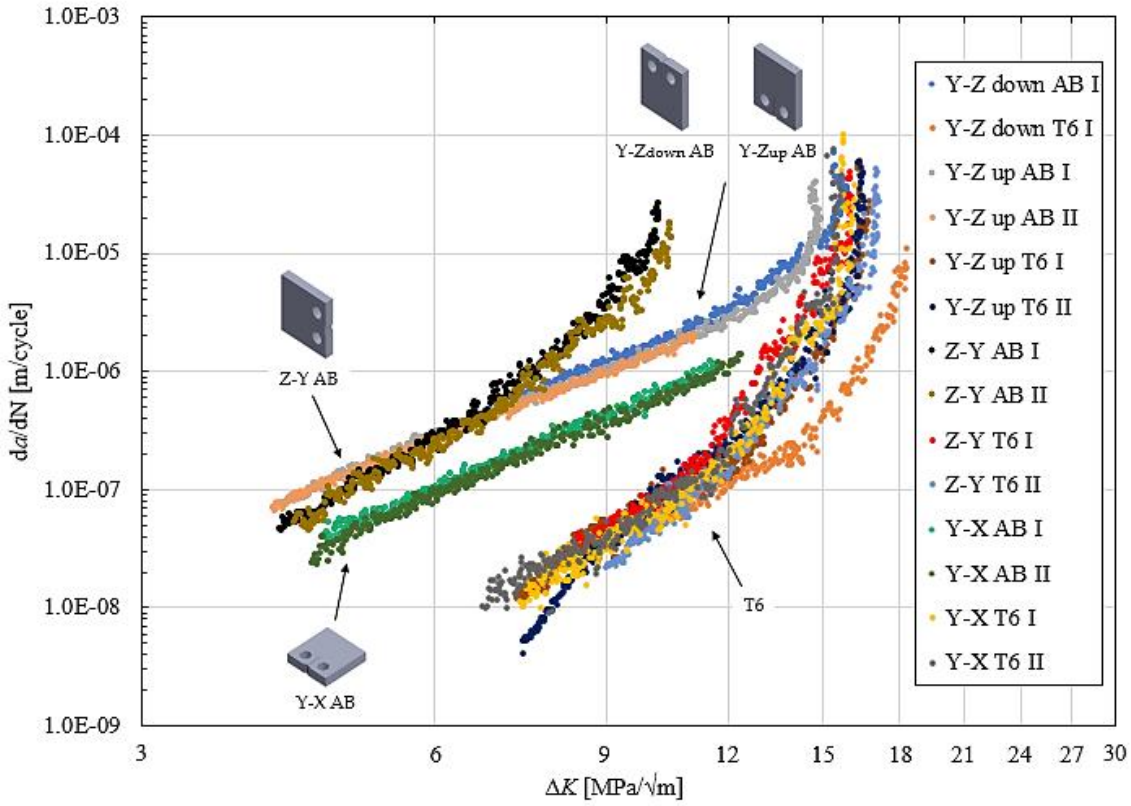

Figure 14 – Experimental *da*/*dN* vs. Δ*K* curves of AlSi10Mg SLM specimens for the Y-Z_{down}, Y-Z_{up}, Z-Y, Y-X planes in the AB and T6 conditions.

Fracture paths

Typical fracture paths of both the AB and T6 conditions are shown in Figure 16. In the AB case, interdendritic fracture is observed, crack paths extend along solidification cells, where eutectic Si particles are mainly segregated and easily connected to play an easy-path role. Significant plastic deformation and cracked matrix regions are also observed. Under the T6 condition, coarsening of Si particles occurs, and as result, the spacing between Si phases increases. Crack propagation appears to be hindered by the ductile matrix, and secondary

cracks are sporadically observed. These observations corroborated the overall trend exposed by Figure 14, in which all AB samples feature higher crack growth rates than T6 ones at similar ΔK level.

Table 8 - Paris constants (C and m) for all the specimens tested.

Specimen	C (m/cycle)	m
Y-Z_{down} AB I	4.52×10^{-10}	3.6
Y-Z_{down} T6 I	5.62×10^{-11}	3.0
Y-Z_{up} AB I	7.29×10^{-10}	3.3
Y-Z_{up} AB II	7.26×10^{-10}	3.3
Y-Z_{up} T6 I	1.69×10^{-11}	3.7
Y-Z_{up} T6 II	5.19×10^{-13}	5.2
Z-Y AB I	4.97×10^{-11}	4.8
Z-Y AB II	6.72×10^{-11}	4.6
Z-Y T6 I	1.73×10^{-12}	4.7
Z-Y T6 II	7.33×10^{-13}	4.7
Y-X AB I	1.81×10^{-10}	3.5
Y-X AB II	2.29×10^{-10}	3.4
Y-X T6 I	1.00×10^{-11}	3.8
Y-X T6 II	1.54×10^{-11}	3.6

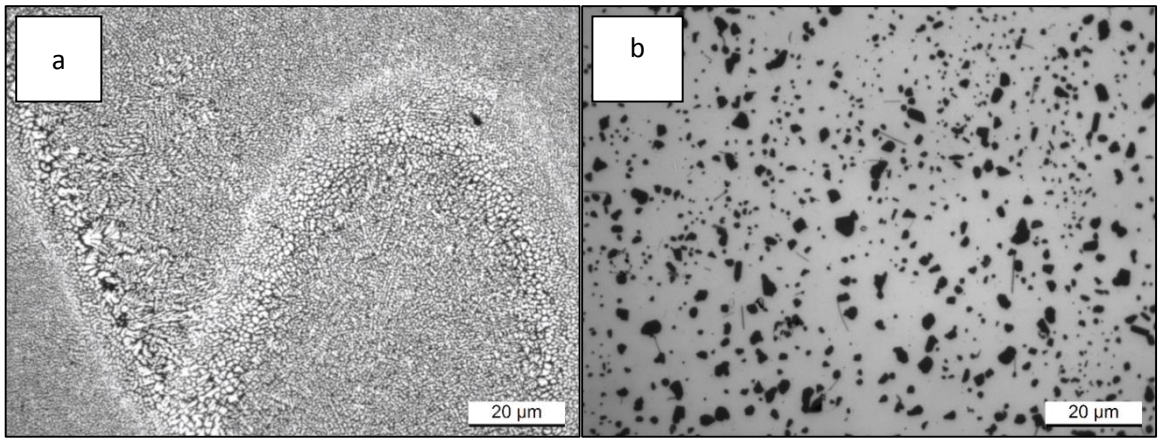

Figure 15 - Optical micrographs of the investigated alloys after etching with Keller's reagent, perpendicular to the Z direction in Figure 13, for the (a) as built and (b) T6 conditions.

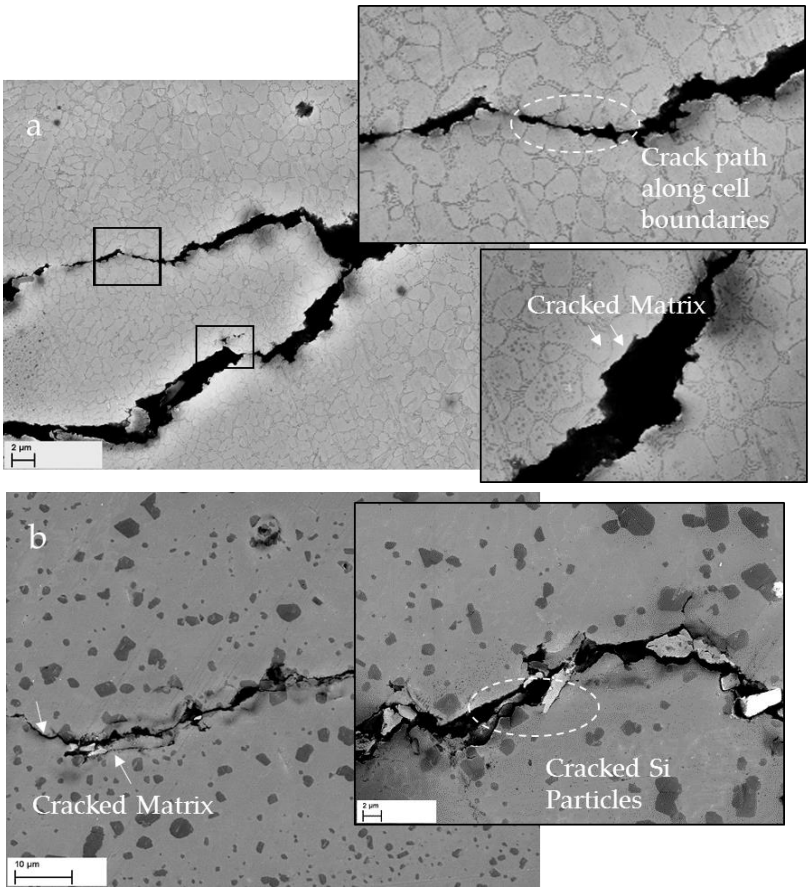

Figure 16 - SEM micrographs showing the crack paths for two AlSi10Mg SLM specimens in both (a) as built (Y-Z_{down} AB I) and (b) T6 heat treated (Y-Z_{down} T6 I) conditions.

Fracture Surfaces

Figure 17 displays a series of SEM images, taken at different magnifications, for two representative AB and T6 Z-Y specimens. Images 5.a, 5.c, and 5.e show the fracture surface of Z-Y AB I specimen, and images 5.b, 5.d, and 5.f correspond to the Z-Y T6 I specimen. Figure 18 displays similar images for two representative AB and T6 Y-X specimens. Images 6.a, 6.c, and 6.e show the fracture surface of Y-X AB I specimen, whereas images 6.b, 6.d, and 6.f correspond to the Y-X T6 I specimen.

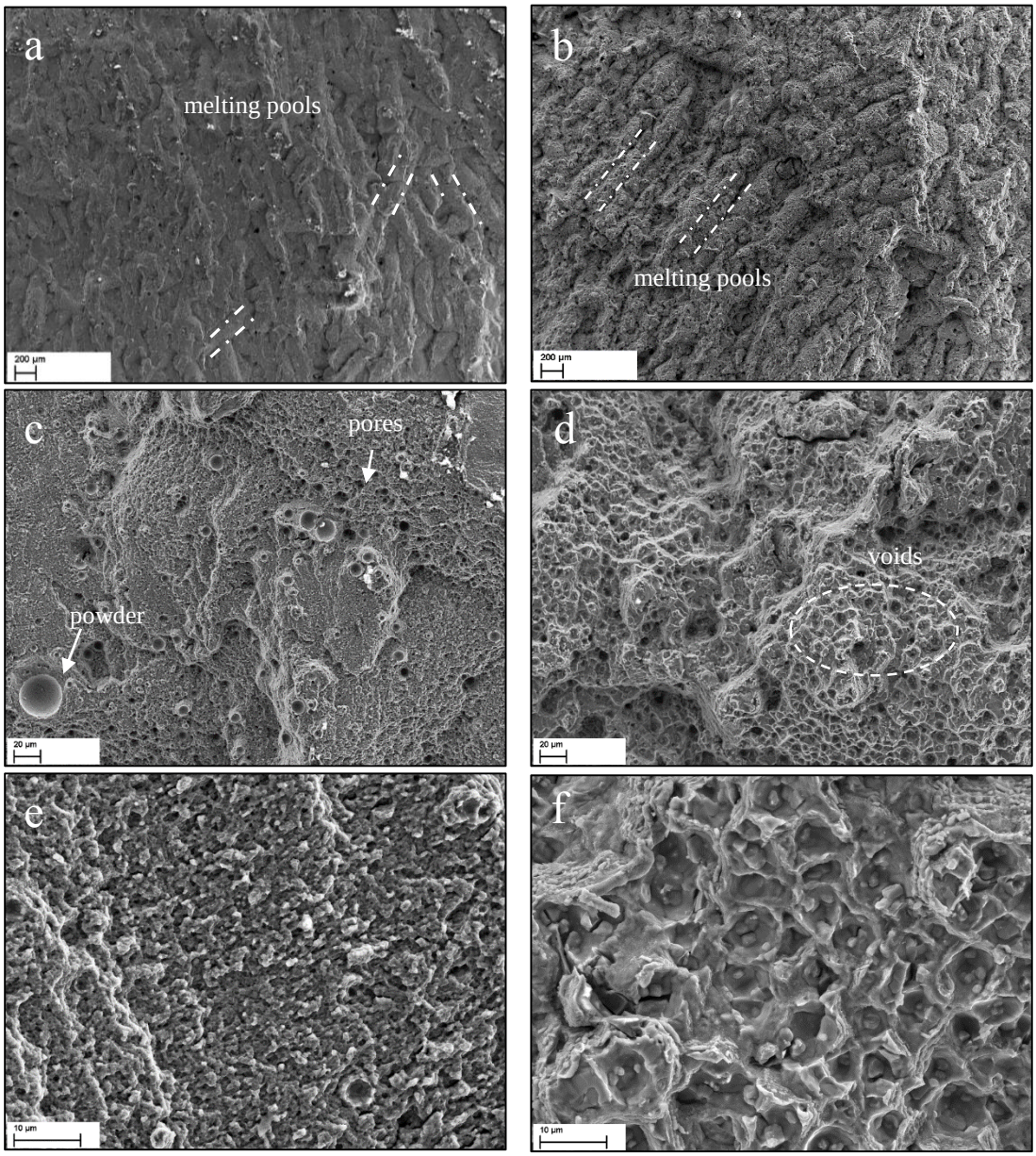

Figure 17 - SEM micrographs showing fracture surfaces for two AlSi10Mg SLM specimens in both (a-c-e) as built (Z-Y AB I) and (b-d-f) T6 heat treated (Z-Y T6 I) conditions.

Figure 19.a and 7.b reports EDS maps of Al and Si, showing the typical microstructural features in both the (a) as built (Z-Y AB I) and (b) T6 heat treated (Y-X T6 I) conditions, respectively.

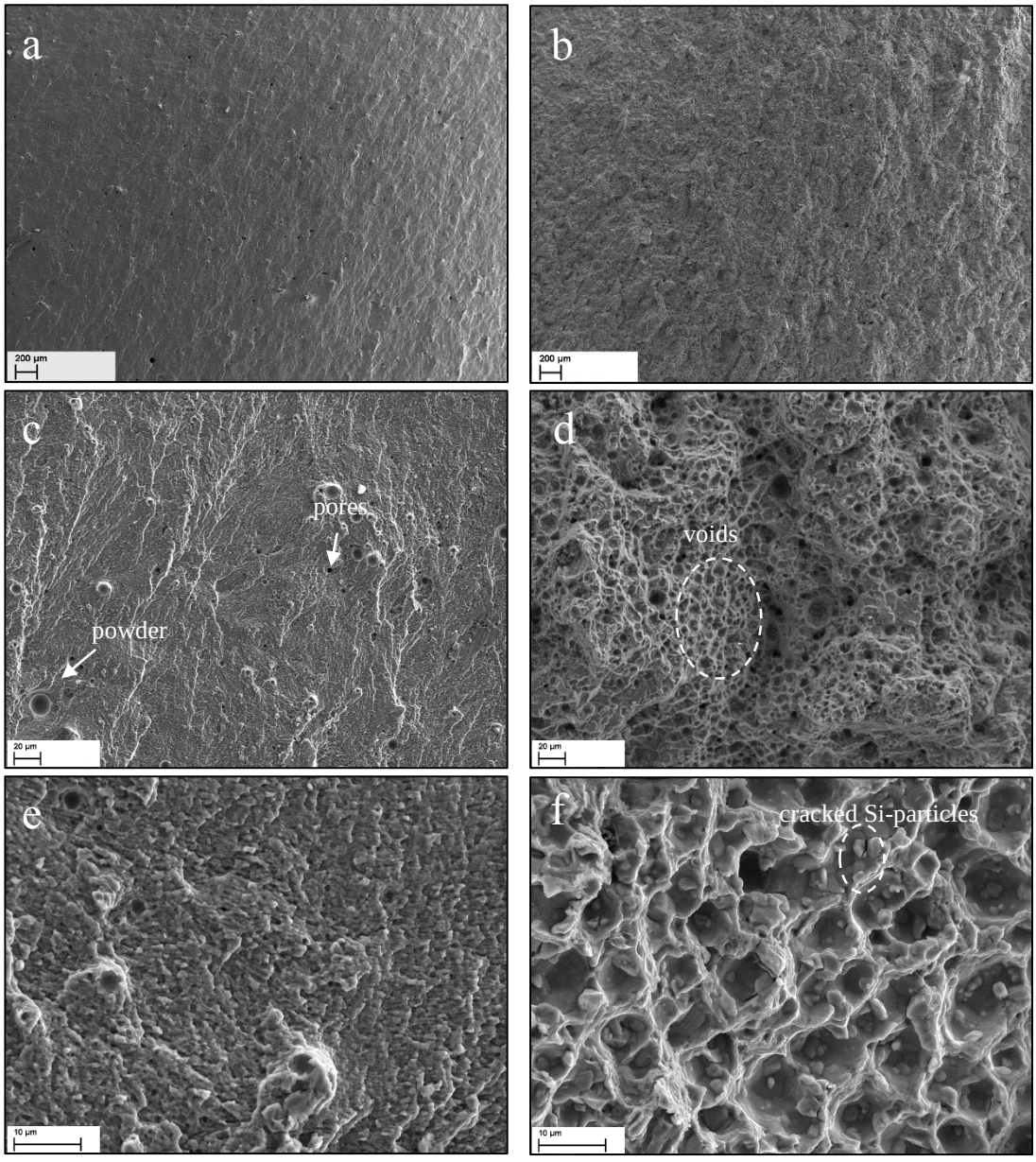

Figure 18 – SEM micrographs showing fracture surfaces for two AlSi10Mg SLM specimens in both (a-c-e) as built (Y-X AB I) and (b-d-f) T6 heat treated (Y-X T6 I) conditions.

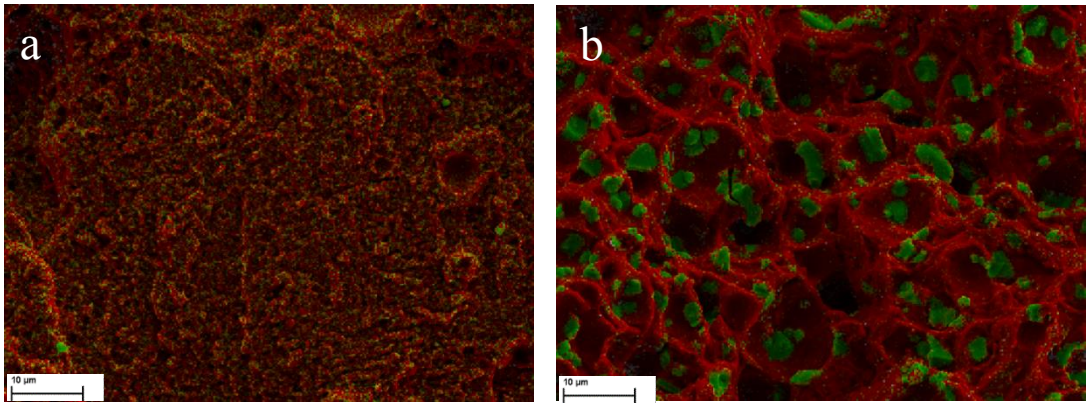

Figure 19 - EDS maps of Al (red) and Si (green) showing the typical microstructural features in both (a) as built (Z-Y AB I) and (b) T6 heat treated (Y-X T6 I) conditions.

Residual Stresses

Two representative samples, Z-Y AB and Z-Y T6, have been selected for evaluating the residual stresses' variation along the Z axis (top and bottom samples' surfaces). The $\sin^2\psi$ plots for all tested surfaces are shown in Figure 8. Residual stressed as measured by X-ray diffraction are listed in Table 4.

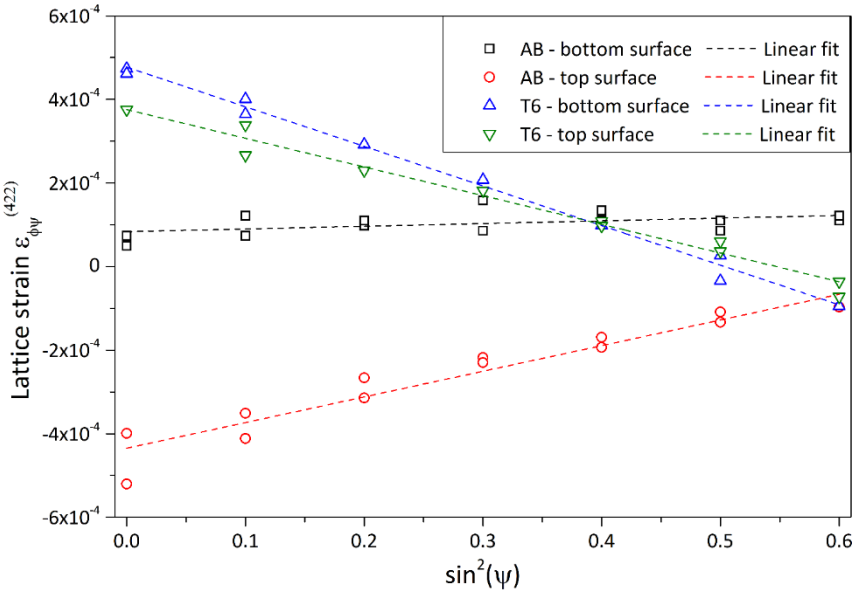

Figure 20 - Examples of $\sin^2\psi$ plots for samples Z-Y AB and Z-Y T6, on both the top and bottom faces, along the direction φ=0°. Linear fitting according to Equation (2.a) is also shown.

Table 9 - Residual stresses measured by X-ray diffraction on the top and bottom surfaces of Z-Y AB and Z-Y T6 samples.

Sample	Top surface	Bottom surface
Z-Y AB	σ_1 = 32 MPa	σ_1 = 3 MPa
	σ_2 = 62 MPa	σ_2 = -35 MPa
	τ_{12} = -2 MPa	τ_{12} = -6 MPa
Z-Y T6	σ_1 = -36 MPa	σ_1 = -50 MPa
	σ_2 = -44 MPa	σ_2 = -33 MPa
	τ_{12} = -1 MPa	τ_{12} = 7 MPa

Discussion

Focusing initially on the results of residual stresses evaluation, the $\sin^2\psi$ plots (Figure 20) show good linearity for all tested surfaces, corroborating the assumption of a plane stress state. Considerable differences emerge between the residual stress state of Z-Y AB and Z-Y T6 samples. On both the top and bottom face of the Z-Y AB samples, stresses along the φ=0° and φ=90° directions (i.e. parallel to the two sides of the specimen) differ significantly, presumably as the result of the specific patterning described by the laser. Most importantly, whilst the bottom face exhibits mild compression along the direction φ=90° and nearly zero stress along the φ=0° direction, stresses shift to considerably larger tensile values on the top surface. Following classical models of residual stress generation in layered materials [17], tensile stresses are presumably developed on the topmost layer as its shrinkage is restrained by the colder underlying material. This also induces compression on the underlying layers, countering the tensile residual stress state presumably developed immediately after their own deposition, and leading to neutral or moderately compressive stress on the bottom face. After the T6 heat treatment, stresses are considerably homogenized, as little difference exists between the φ=0° and φ=90° directions, consistent with previous microstructural observations. Stresses become compressive on both the top

and bottom faces, which might be the result of thermal gradients between the core and the surface of the sample during the various heating and cooling stages of the T6 treatment.

All experimental d*a*/dN *vs.* Δ*K* curves were presented in Figure 14. From this Figure, it can be inferred that the curves of T6 heat treated specimens appear to be grouped to the right of the curves of AB specimens, featuring lower crack growth rates for the same applied Δ*K* range. In the AB condition, the Y-X specimen orientation shows the highest resistance to fatigue crack propagation, whereas the Z-Y orientation features the lowest one. Images of the fracture surface of AB and T6 Z-Y samples (Figure 17.a and 5.b, respectively) show that the crack grew in this case along the melt pools boundaries, while the fracture of the Y-X samples (Figure 18.a and 6.b) no specific path can be found. These observations explain the higher crack-growth rate observed in Z-Y AB specimens if compared to Y-X AB ones, being the former the less resistant to fatigue crack growth at intermediate Δ*K* levels, as shown in Figure 14. Higher magnification observations reveal the presence of possible gas-driven porosity (based on the small size and round shape) and lack-of-fusion porosity (indicated by the unmelted powder particles) in the AB samples (Figure 17.c and Figure 18.c) whereas a dimple-like fracture (voids) surface is clearly seen in heat-treated specimens (Figure 17.d and Figure 18.d). These observations are in line with the lower crack growth rates of all T6 specimens if compared to the AB ones at similar Δ*K* levels. Additionally, in T6 specimens fracture of the silicon particles at the center of the voids left by the crack growth was occasionally observed (Figure 18.f), which can be related to a more energy consuming process that can also explain the lower crack-growth rates in these cases. Mostly, voids appear to have initiated at the silicon-aluminum interface. Further, EDS maps of Al and Si (Figure 7.a and Figure 7.b) confirm the presence of a distributed network of fine Si particles at the α-Al grain boundaries, whereas the T6 sample exhibits a coarser structure with larger, more distanced Si particles.Comparing the Y-Z_{down} AB and Y-Z_{up} AB specimens, Figure 2 displays overlapping curves, as cracks are found to cross the same microstructure, in the first case from the bottom to the top, and in the opposite direction in the second case. That behavior is reflected in the obtained Paris coefficients (Table 8) of Y-Z_{down}, Y-Z_{up}, and Y-X specimens in both conditions (AB and T6), which featured similar values of *m*, between 3.0 and 3.8. Only one specimen (Y-Z_{up} T6 II) shown a higher *m* value (*m* = 5.2). Moreover, in both conditions, the Z-Y specimens presented higher *m* values than other specimens' directions (between 4.6 and 4.8). From the constant *C*, it can be observed that the crack propagation per cycle decreased with the heat treatment in all specimens' directions, which is consistent with the results shown in Figure 14.

As described above, the FCG resistance is substantially increased after heat treatment, relative to the AB condition. This behavior is consistent with the residual stress measurements, which evidenced: i. a compressive and uniform stress state on both the top the top and bottom faces of the investigated T6 specimen and, ii. a significant stresses variation when comparing AB bottom and top faces.

The AB response appears to be strongly dependent on the building orientation, offering the best compromise for the Y-X condition, and the worst for the Z-Y condition. Fractographs of the Z-Y oriented AB specimen (Figure 17.a) demonstrate that the fracture occurred in the vicinity of the boundaries between the melt pools, where heat-affected-zones (HAZ) are found to offer softer and less ductile networks [18], unlike the Y-X fracture surface (Figure 6.a), which reveals the occurrence of fracture at random locations within the laser track segments.

With the aim to clarify the fracture propagation mode, a model has been proposed in Figure 9. Basically, the crack path appears to propagate crossing the layers in the Y-Z_{down}/Y-Z_{up} and Y-X cases (panels a and b in Figure respectively), whereas it is found to propagate along the layer in Z-Y oriented samples, as indicated by the fracture surfaces (panel c in). Hence, in the Z-Y oriented samples, cracks can easily propagate along the weakest link, namely the HAZ along the interlayer boundary, whilst, in the Y-Z_{down}/Y-Z_{up} and Y-X cases, the crack has to cross tougher intra-layer regions. Si particles finely distributed around the α-Al grains along the boundaries between the melt pools are the dominant contributor to the fracture initiation, as they enhance the local strain hardening. This fact suggests that changing the distributions of Si-particles would be an effective means of controlling the direction-dependence of the FCG response.

Thus, in agreement with FCG results (Figure 14) it is possible to associate higher energy consumption when considering the cross-layers propagation mode, and lower energy consumption when considering the propagation along the layer. Crack propagates crossing layers in the Y-Z_{up}/Y-Z_{down} and Y-X cases, where it is found to propagate along the layer in the Z-Y case. Fracture surfaces show tearing along the melt-pool boundaries for both the AB and T6 Z-Y oriented specimens.

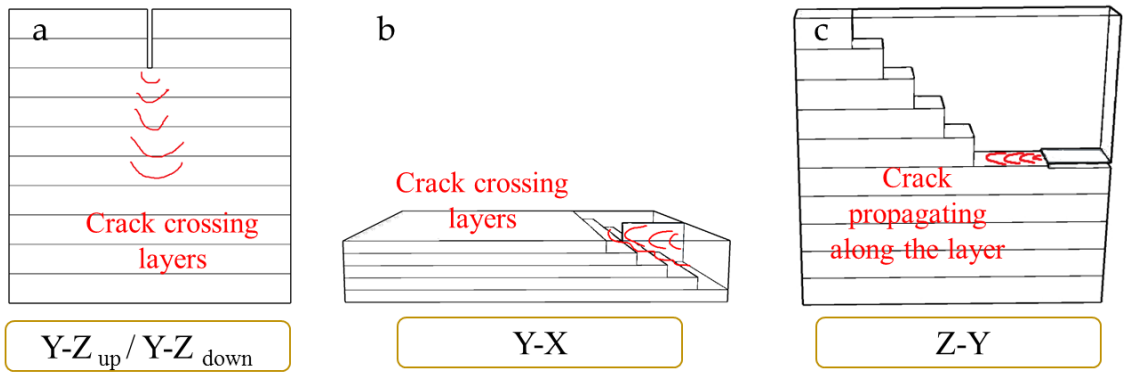

Figure 21 - Fracture model for specimens with different building orientation: (a) Y-Z_{up}/Y-Z_{down}, (b) Y-X, and (c) Z-Y.

Moreover, in the Y-X case, the crack simultaneously crosses the top layers under tensile residual stress and bottom layers under compressive residual stress: the latter help restraining the crack advancement at every cycle, which can contribute to explaining why stable crack growth rate is the lowest in this condition. On the other hand, in both the Y-Z_{down} and Y-Z_{up} samples, the stable crack growth regime occurs within the middle layers, subject to similar residual stress states. Neither a favorable effect of bottom-face residual compression in the Y-Z_{up} sample, nor a negative effect of top-face residual tension in the Y-Z_{down} sample can be observed, as the cracks in the respective samples reach those regions only in the final stages of the fatigue tests, out of the stable (Paris) regime.

Microstructural and stress homogenization, on the other hand, explain why the T6 samples exhibit improved fatigue crack growth resistance with little or no orientation dependence. It is particularly interesting that more relaxed and coarser microstructure constituents in the heat treated condition result in improved fatigue crack growth behavior, regardless of specimens building orientation.

Concluding Remarks

The steady-state fatigue crack growth (FCG) behavior (Paris regime) was studied in additively manufactured AlSi10Mg samples obtained by selective laser melting (SLM), both in as-built condition and after a T6 heat treatment. The following conclusions can be drawn from the experimental findings:

- The effect of the relationship between build direction and fatigue crack growth rate is most noticeable when the material is tested in the as-built condition and may be accounted for by anisotropies in microstructure and residual stress distribution. Considerable differences emerge the residual stress states of the top and bottom of the representative Z-Y AB specimen.
- The fracture mode was responsible for the observed direction-dependence on the FCG response. Specifically, the heat-affected zones (HAZs) around interlayer boundaries are the weakest link in the material, because Si particles finely distributed around the α-Al grains along the boundaries between adjacent melt pools are the dominant contributor to fracture initiation and propagation.
- Cracks propagating along planes oriented perpendicular to the layers therefore encounter more resistance than they do when propagating parallel to the layers, as in the latter case they can easily move along the weak HAZs. Cracks propagating transversally along the entire thickness of the as-built sample exhibit the lowest fatigue crack growth rates as they are constantly forced to open up bottom layers subject to compressive residual stresses.
- After a T6-heat treatment, homogenization of the microstructure and of residual stresses minimizes the dependence of crack growth rate on crack orientation. Restructuring of the Si precipitates into large, rounded particles, farther away from one another than are the fine Si precipitates in as-built condition, enhances the fatigue resistance as the crack is forced to propagate across tough, pure α-Al regions.

Acknowledgments

The authors would like to acknowledge Beam-IT for providing the experimental material and CAPES Brazil for the scholarship of João Teixeira Oliveira de Menezes.

References

[1] G. Nicoletto, Directional and notch effects on the fatigue behavior of as-built DMLS Ti6Al4V, Int. J. Fatigue 106 (2017)124-131. doi: http://doi.org/10.1016/j.ijfatigue.2017.10.004

[2] M. Seifi, A. Salem, J. Beuth, O. Harrysson, J.J. Lewandowski, Overview of Materials Qualification Needs for Metal Additive Manufacturing, JOM 68(3) (2016) 747–764.

[3] S. Gorsse, C. Hutchinson, M. Gouné, R. Banerjee, Additive manufacturing of metals: a brief review of the characteristic microstructures and properties of steels, Ti-6Al-4V and high-entropy alloys, Sci. Technol. Adv. Mater.18(1) (2017) 584–610. doi10.1080/14686996.2017.1361305

[4] J.J. Lewandowski, M. Seifi, Metal Additive Manufacturing: A Review of Mechanical Properties. Annual Review of Materials Research, 46(1) (2016) 151–186. doi:10.1146/annurev-matsci-070115-032024.

[5] L. Shiwen, Z. Haihong, P. Gangyong, Microstructure prediction of selective laser melting AlSi10Mg using finite element analysis, Mater. Des. 142 (2018) 319-328.

[6] F. Michaela, D. Drahomir, A. Michalcova, Changes in the microstructure and mechanical properties of additively manufactured AlSi10Mgalloy after exposure to elevated temperatures, Mater. Charact. 137 (2018) 119-126.

[7] D. Donghua, G. Dongdong, Z. Han, Influence of scan strategy and molten pool configuration on microstructures and tensile properties of selective laser melting additive manufactured aluminum based parts, Opt. Laser. Technol. 99 (2018) 91-100.

[8] A. Tridello, C.A. Biffi, J. Fiocchi, VHCF response of as-built SLM AlSi10Mg specimens with large loaded volume, Fatigue Fract. Eng. Mater. Struct. 2018, (41), 1918-1928.

[9] S. Bagherifard, N. Beretta, S. Monti, On the fatigue strength enhancement of additive manufactured AlSi10Mg parts by mechanical and thermal post-processing, Mater. Des. 145 (2018) 28-41

[10] V. Cain, L. Thijs, J. Van Humbeeck, B. Van Hooreweder, R. Knutsen, Crack propagation and fracture toughness of Ti6Al4V alloy produced by selective laser melting,

Additive Manufacturing, Volume 5, 2015, Pages 68-76, https://doi.org/10.1016/j.addma.2014.12.006.

[11] ASTM E647-15e1, Standard Test Method for Measurement of Fatigue Crack Growth Rates, ASTM International, West Conshohocken, PA, 2015, www.astm.org.

[12] A.C. Vermeulen, D. Götz, Data Collection Requirements for the Analysis of Residual Stress in Polycrystalline Coatings, Mater. Sci. Forum 524–525 (2006) 795–800.

[13] U. Welzel, J. Ligot, P. Lamparter, A.C. Vermeulen, E.J. Mittemeijer, Stress analysis of polycrystalline thin films and surface regions by X-ray diffraction, J. Appl. Crystallogr. 38 (2005) 1–29.

[14] B. Eigenmann, E. Macherauch, Röntgenographische Untersuchung von Spannungszuständen in Werkstoffen – Teil III, Materialwissenschaft &Werkstofftechnik 27 (1996) 426-437.

[15] S. Suresh, Fatigue of Materials, 2nd Ed. Cambridge University Press, New York, 1998.

[16] L. Thijs, K. Kempen, J.P. Kruth, J. Van Humbeeck, Fine-structured aluminium products with controllable texture by selective laser melting of pre-alloyed AlSi10Mg powder, Acta Materialia 61(5) (2013) 1809-1819.

[17] Y.C. Tsui, T.W. Clyne, An analytical model for predicting residual stresses in progressively deposited coatings Part 1: Planar geometry, Thin Solid Films 306(1) (1997) 23-33.

[18] Tang, Ming. Inclusions, Porosity and Fatigue of AlSi10Mg Parts Produced by Selective Laser Melting, PhD. Dissertation (2017) p. 903.